Bridging effects on Mixed Mode delamination: experiments and numerical simulation

THÈSE N^{O} 7056 (2016)

PRÉSENTÉE LE 24 JUIN 2016

À LA FACULTÉ DES SCIENCES ET TECHNIQUES DE L'INGÉNIEUR
LABORATOIRE DE MÉCANIQUE APPLIQUÉE ET D'ANALYSE DE FIABILITÉ
PROGRAMME DOCTORAL EN MÉCANIQUE

ÉCOLE POLYTECHNIQUE FÉDÉRALE DE LAUSANNE

POUR L'OBTENTION DU GRADE DE DOCTEUR ÈS SCIENCES

PAR

Marco BOROTTO

acceptée sur proposition du jury:

Prof. L. Laloui, président du jury
Prof. J. Botsis, directeur de thèse
Prof. M. Alfano, rapporteur
Prof. D. Karalekas, rapporteur
Prof. D. Pioletti, rapporteur

ÉCOLE POLYTECHNIQUE
FÉDÉRALE DE LAUSANNE
Suisse
2016

Abstract

Composite materials and, in particular, Carbon Fibre Reinforced Polymers (CFRP) have been well studied and developed in the past years due to their advanced mechanical characteristics. These materials are used in several different application fields, such as aerospace, automotive, energy production, civil constructions, bio-prosthesis and sport equipment. The combination of carbon fibers with epoxy resin allows obtaining materials characterized by high specific stiffness, low weight, and extremely high ultimate strength, properties almost impossible to obtain by the standard metallic materials.

Although the mechanical properties of the single carbon fiber are impressive, damage initiation often occurs at lower stresses. These materials are produced by stacking a sequence of several layers, which makes them prone to delamination. This process may lead to the creation of bridging fibers across the crack surfaces, which increases the total fracture toughness. Several important efforts have been devoted in the past years to study the delamination process of composite materials under pure Mode I, characterized by a high bridging contribution, and pure Mode II where no bridging fibers are involved. However, studies of delamination and bridging in Mixed Mode have not received adequate attention in the literature.

The first goal of this project is to study the delamination process for unidirectional CFRP under Mixed Mode conditions. Experiments are performed over a wide range of different mode mixities $\mu = \frac{G_{II}}{G_{tot}}$, where G_{II} represents the Mode II energy release rate component and $G_{tot} = G_I + G_{II}$ the total one, by using a Mixed Mode Bending (MMB) setting and monitoring the applied displacement, reaction force, crack propagation and internal strains. Axial strain values are measured in specific specimens by embedding optical fibers with Bragg grating sensors (FBGs) between the carbon layers, during the manufacturing process. Delamination tests are performed at pure Mode I, Mixed Mode at 20%, 30%, 40%, 60% and pure Mode II, in order to obtain a complete set of experimental data. The results allowed characterizing both the energy release rate at crack initiation G_c and the corresponding bridging energy contribution G_b, as a function of the applied mode mixity. The fracture toughness G_c increases with μ while it is found out that large scale bridging occurs in pure Mode I and Mixed Mode up to $\mu = 30\%$, affecting

the stress field and the crack propagation, while a negligible bridging contribution occurs for higher mode mixities.

The second goal of this work is to create a numerical FE Model, based on cohesive elements, able to reproduce the correct delamination behavior and bridging contribution for each tested mode mixity, by using a unique cohesive law. Unfortunately, the cohesive law formulations for Mixed Mode delamination known so far show several limitations since they are not able to properly predict the delamination behavior in a MMB test when large scale bridging occurs. These models are based on the assumption that the local mode mixity $\beta = \frac{\delta_{shear}}{\delta_{normal}}$, which represents the ratio between the shear and normal displacements for each cohesive element, is directly related to the energy mode mixity μ according to the formula $\mu = \frac{\beta^2}{1+\beta^2}$. This work points out the limitations of this formulation, showing that it can be used only if β is constant along the entire process zone. Since for a Mixed Mode delamination test, based on a MMB setting, the β value keeps changing even if the applied energy mode mixity μ is constant, this approach cannot be used to properly simulate the experiments. For this reason, an innovative mode-dependent cohesive formulation is implemented: it extends the constitutive laws of the previous models to incorporate the proper bridging contribution, by using an external customized routine which uses the computed displacement mode mixity β as an indicator, named β^*.

The bridging tractions are defined by three parameters: the corresponding energy contribution G_b, the maximum stress σ_{max} and the crack opening displacement at failure δ_f. These bridging parameters are described by three different functions, dependent on the mode mixity indicator β^*, by means of the coefficients $\xi_i = \left[\xi_{G_b}, \xi_{\sigma_{max}}, \xi_{\delta_f}\right]$. The coefficients ξ_i are obtained by using an inverse method, where the strains measured by the FBGs and the ones computed by the Finite Element Model (FEM) are involved in an optimization process. In contrast to the standard Mixed Model models, this algorithm provides a unique mode-dependent cohesive law able to properly simulate all the different delamination tests, from pure Mode I up to pure Mode II, predicting the load, the crack propagation, the energy release rate (ERR) and the strains evolution.

Keywords: Mixed Mode, delamination, CFRP, fibre bridging, fibre Bragg grating sensors, cohesive elements, FE modelling

Résumé

Les matériaux composites, et en particulier les polymères renforcés avec des fibres de carbone (CFRP), ont été longuement étudiés, analysés et développés ces dernières années du fait de leurs hautes caractéristiques mécaniques. Les matériaux composites sont utilisés dans différents domaines, comme l'automobile, l'aérospatial, la production d'énergie, des constructions civiles, les prothèses et l'équipement sportif. La combinaison de fibres de carbone avec la résine époxy permet d'obtenir un matériau d'une grande rigidité spécifique, léger, et d'une limite à la rupture extrêmement élevée, soit des propriétés presque impossible à obtenir par des matériaux métalliques standards.

Bien que les propriétés mécaniques de la fibre de carbone seule soient impressionnantes, l'endommagement ou la rupture totale survient souvent à des charges moins élevées. Les matériaux composites sont produits en empilant une séquence de plusieurs couches, ce qui les rend enclins à la délamination. Ce processus peut mener à la création de pontage de fibres entre les deux surfaces de la fissure, ce qui augmente la ténacité du matériau. Beaucoup d'efforts ont été consacrés ces dernières années à étudier le processus de délamination de matériaux composites en pure Mode I, caractérisé par une haute contribution du pontage de fibres, et le pur Mode II où le pontage de fibre n'intervient pas. Cependant, l'étude de la délamination et du pontage en mode mixte n'a pas reçu l'attention adéquate dans la littérature.

Le premier objectif de ce projet est d'étudier le processus de délamination pour des CFRP unidirectionnels dans des conditions de Mode Mixte. Les expériences sont exécutées sur une vaste gamme de mixités de modes $\mu = \frac{G_{II}}{G_{tot}}$, où G_{II} représente la composante du taux de restitution d'énergie en Mode II et $G_{tot} = G_I + G_{II}$ le taux de restitution d'énergie total (ERR), en utilisant la configuration du test Mixed Mode Bending (MMB) et le monitoring du déplacement imposé, de la force de réaction, de la propagation de fissure et des déformations internes. Les déformations axiales sont mesurées dans des spécimens spécifiques en intégrant pendant la fabrication, des capteurs à fibres optiques contenant des réseaux de Bragg multiplexes (FBG) entre les couches de CFRP. Les tests de délamination sont exécutes en Mode I pur, en Mode Mixte 20%, 30%, 40%, 60%, et en Mode II pur, en vue d'obtenir un set complet de données

expérimentales. Les résultats ont permis de caractériser l'ERR à l'initiation de propagation de fissure G_c, ainsi que la contribution d'énergie due au pontage de fibres G_b, comme une fonction de la mixité de mode appliquée. La ténacité G_c augmente avec μ, et il a été montré que le pontage de grande échelle intervient uniquement dans le Mode I pur et le Mode Mixte jusqu'à $\mu = 30\%$, affectant le champ de contraintes et la propagation de fissure, tandis que la contribution du pontage de fibres est négligeable des mixités de mode plus élevés.

Le deuxième objectif de ce travail est de créer un modèle numérique à éléments finis, basé sur des éléments cohésifs, capable de reproduire le comportement en délamination correct ainsi que la contribution du pontage de fibres pour chaque mixité de mode testée, en utilisant une loi cohésive unique. Malheureusement, les formulations des lois cohésives pour la délamination de Mode Mixte connues montrent jusqu'ici plusieurs limitations puisqu'ils peuvent ne pas correctement prédire le comportement en délamination dans un test de MMB en cas de pontage de grande échelle. Ces modèles sont basés sur l'hypothèse que la mixité de mode locale $\beta = \frac{\delta_{cisaillement}}{\delta_{normal}}$, qui représente le ratio entre les déplacements en cisaillement et les déplacements normaux pour chaque élément cohésif, est directement corrélé a l'énergie de mixité de mode μ selon la formule $\mu = \frac{\beta^2}{1+\beta^2}$. Ce travail souligne les limitations de cette formulation, montrant qu'il peut être utilisé seulement si β est constant le long de la zone de processus entière. Sachant que pour un test de délamination en Mode Mixte, basé sur de la configuration MMB, la valeur de β continue à changer même si l'énergie de mixité de mode appliquée μ est constante, cette approche ne peut pas être utilisée pour correctement simuler les expériences. C'est pourquoi, une innovante formulation cohésive dépendante du mode est implémentée : elle étend les lois constitutives des modèles précédents pour incorporer la contribution de pontage de fibres appropriée, ce en utilisant une routine externe personnalisée qui utilise le mode de déplacement calculé mixity β comme un indicateur, nommé β^*.

Les tractions de pontage sont définies par 3 paramètres: la contribution énergétique correspondante G_b, la contrainte maximale σ_{max} et l'ouverture de la fissure à la rupture δ_f. Les paramètres de pontage sont décrits par trois fonctions différentes, selon l'indice de mixité des modes β^*, au moyen des coefficients $\xi_i = \left[\xi_{G_b}, \xi_{\sigma_{max}}, \xi_{\delta_f}\right]$. Les coefficients ξ_i sont obtenus en utilisant une méthode inverse, où les déformations mesurées par les FBGs et celles calculées par le Modèle par Éléments Finis (FEM) sont impliquées dans un processus d'optimisation. Contrairement aux Modèles standards de modes mixtes, cet algorithme fournit une loi cohésive unique, dépendante du mode, capable de correctement simuler tous les tests de délamination du Mode I pur jusqu'au Mode pur II, prévoyant la force, la propagation de fissure, l'ERR et l'évolution des déformations.

Mots-clés: Mode Mixte, délamination, CFRP, pontage de fibres, réseau de Bragg, élément cohésifs, FE modelling

Acknowledgments

First, I want to thank Prof. J. Botsis for the opportunity he gave me to work in his laboratory. Thanks for being a strong technical guide, supporting and pushing me during our weekly meetings throughout the whole project. Another special acknowledgment goes to Dr. Joël Cugnoni for his precious contribution to the project, for all his suggestions and ideas, for his infinite knowledge and skills combined with a great simplicity. I learned a lot from both of you.

I also want to thank all the LMAF colleagues that I met during these years. I will always remember the "super useful" french-italian tandem session together with Nassima (...), the never ending discussions about everything with George and Luis and our lunch breaks. I want also to thank Dr. Marco Alfano, a great researcher always willing to share ideas and an amazing office mate: it has been a pleasure to have you here. Another sincere thanks to Viviane, one of the most kind, reliable and useful person of the lab.

Then a big hug to the Italian community in Lausanne, I met so many nice people and shared moments I will keep forever with me. A special thought goes to Marco Lai, initially a colleague and afterwards a great friend and a bitter enemy on basketball courts. Another thanks for my lunch break Italian group, which always added a smile on my face and updated me on every sort of gossip.

I also want to thank two proper friends, Alessandro Arena and Enrico de Cais, for being as brothers despite the distance. I am so grateful that you both have been part of this journey.

Now a special thought for my mother and father: I thank you so much for your support and love during these years throughout good and dark moments, I will be forever grateful to you. I also want to give a big hug to my sister Erika and my amazing nephews Marta, Greta and the new entry Giorgio. I love you all.

Another though is for a very special person, who literally changed my life and allowed me to grow and become what I am now. Thanks Pia for what you do.

Finally, I do not have enough words to thank my sunshine Stefania. It has been hard living far from my heart for 4 years but thanks for all your support from the day I decided to leave up to now. Another big hug goes to Alfredo, Maria and Daniela, thanks for being part of my life

during all these years and for your warm welcome.

Contents

1 Introduction **1**

1.1 Motivation 1

1.2 Objectives 2

1.3 Outline 3

2 State of the art **5**

2.1 Delamination in composites 5

2.2 Delamination tests 6

2.3 Bridging and cohesive law 8

2.4 Fiber Bragg Grating sensors 10

2.4.1 Multiplexed sensing 10

2.5 Summary 12

3 Materials and methods **13**

3.1 Material properties, manufacturing and testing parameters 13

3.1.1 Specimen preparation 17

3.1.2 Testing machine and settings 19

3.1.3 Crack measurement 21

3.2 Experimental energy release rate 21

3.2.1 Compliance method 24

3.3 Measurements by fiber Bragg grating sensors 25

3.3.1 Optical Low-Coherence Reflectometry 28

3.4 Cohesive Elements 32

4 Experimental results **35**

4.1 Mode I delamination test 35

4.2 Mixed Mode Delamination tests 42

4.2.1 Mixed Mode test: 20% . . . 43
4.2.2 Mixed Mode test: 30% . . . 49
4.2.3 Mixed Mode test: 40% . . . 53
4.2.4 Mixed Mode test: 60% . . . 58
4.3 Mode II delamination test . . . 61
4.4 Summary . . . 65

5 Traction separation law in Mixed Mode delamination and optimization approach 69
5.1 Optimization scheme . . . 69
5.2 Mode I: numerical model and bridging identification . . . 71
5.2.1 Numerical model for bridging identification . . . 71
5.2.2 Optimization process for bridging identification . . . 71
5.3 Mixed Mode: numerical model and bridging identification . . . 75
5.3.1 Mode mixity with cohesive elements . . . 75
5.3.1.1 Relationship between β and μ . . . 81
5.3.2 Cohesive law in Mixed Mode . . . 90
5.3.3 FE Model for Mixed Mode delamination . . . 97
5.3.3.1 Abaqus® internal model based on B-K relationship . . . 97
5.3.3.2 Cohesive law in tabulated form . . . 98
5.3.4 External and local mode mixity . . . 98
5.3.5 Bridging modeling . . . 100
5.3.6 Optimization process for bridging parameters . . . 104
5.3.7 Variation of the B-K relationship . . . 108

6 Comparison between experimental and numerical results 111
6.1 Mode I . . . 111
6.2 Mixed Mode . . . 114
6.2.1 20% Mixed Mode . . . 114
6.2.2 30% Mixed Mode . . . 120
6.2.3 40% Mixed Mode . . . 126
6.2.4 60% Mixed Mode . . . 128
6.3 Mode II . . . 130
6.4 Summary . . . 133

7 Conclusions 135
7.1 Future work . . . 137

List of Figures

2.1 Mixed Mode apparatus 9
2.2 Multiplexed sensing, serial and parallel scheme 11

3.1 Material manufacturing, layout for curing in autoclave 14
3.2 Curing cycle for composite fabrication. Vacuum and 3 bars extra pressure applied 15
3.3 Transverse sections of a carbon plate fabricated with (a) $4.05mm$ frame thickness and applied vacuum, (b) $3.95mm$ frame thickness, vacuum and 3 bars extra pressure 16
3.4 Schematic layout of a specimen with embedded optical fiber 16
3.5 Specimen cross section with an embedded optical fiber 17
3.6 Specimens with steel blocks and markers for (a) Mode I and Mixed Mode setting (b) Mode II setting 18
3.7 Mixed Mode Bending setting 20
3.8 Crack front for a Mixed Mode delamination test 22
3.9 Crack in Griffith theory 22
3.10 (a) Compliance calibration method with 2 and 3-terms power law expression (b) Derivatives $\frac{dC}{da}$ 25
3.11 Optical Fiber 26
3.12 Optical fiber subjected to mechanical multi-axial strains 27
3.13 Reflected FBG spectrum from (a) homogeneous strain field and (b) non-homogeneous strain field 28
3.14 OLCR schema 30
3.15 OLCR signal 31
3.16 Cohesive law for fracture simulation (a) without bridging contribution (b) with bridging contribution 32
3.17 Bridging tractions 33

4.1 Mode I specimen with embedded optical fiber 36

4.2 Mode I typical load-displacement curve obtained by a DCB test 36
4.3 Mode I, crack length versus applied displacement obtained by markers; (a) measurement on both sides, (b) averaged value increased by $0.75mm$ to take into account the crack front curvature 37
4.4 Mode I, compliance calibration method. Compliance versus crack length fitted by a power law equation 38
4.5 Mode I, ERR curve. Critical value and evolution with crack propagation 38
4.6 Mode I, bridging tractions in the middle of the crack with the toughening process completely developed 39
4.7 Mode I, strains measured by Multiplexed FBGs as a function of the applied displacement 40
4.8 Mode I, crack length versus applied displacement measured by side markers and FBGs 41
4.9 Mode I, shifted FBGs strains to common crack tip position 41
4.10 Mode I, strain profile measured by the FBGs above the crack plane, along the bridging zone 42
4.11 Mixed Mode Bending setting, specimen and embedded optical fiber 43
4.12 Mixed Mode $\mu = 20\%$, average load-displacement curve and standard deviation . 44
4.13 Mixed Mode $\mu = 20\%$, crack length measured by markers versus applied displacement 44
4.14 Mixed Mode $\mu = 20\%$, ERR. Critical value at crack initiation and evolution with the crack propagation 45
4.15 Mixed Mode $\mu = 20\%$, bridging tractions in the middle of the crack at $\triangle a = 20mm$ 46
4.16 Mixed Mode $\mu = 20\%$, strains measured by Multiplexed FBGs as a function of the applied displacement 47
4.17 Mixed Mode $\mu = 20\%$, crack length measured by side markers and FBGs, versus applied displacement 47
4.18 Mixed Mode $\mu = 20\%$, shifted FBGs strains to common crack tip position 48
4.19 Mixed Mode $\mu = 20\%$, unloading curve to check the linearity of the system . . . 48
4.20 Mixed Mode $\mu = 30\%$, average load-displacement curve and standard deviation . 49
4.21 Mixed Mode $\mu = 30\%$, crack length measured by markers versus applied displacement 50
4.22 Mixed Mode $\mu = 30\%$, ERR. Critical value at crack initiation and evolution with crack propagation 50
4.23 Mixed Mode $\mu = 30\%$, bridging tractions in the middle of the crack at $\triangle a = 20mm$ 51

4.24 Mixed Mode $\mu = 30\%$, strains measured by Multiplexed FBGs as a function of the applied displacement . . . 52
4.25 Mixed Mode $\mu = 30\%$, crack length versus applied displacement measured by side markers and FBGs . . . 52
4.26 Mixed Mode $\mu = 30\%$, shifted FBGs strains to common crack tip position . . . 53
4.27 Mixed Mode $\mu = 40\%$, average load-displacement curve and standard deviation . 54
4.28 Mixed Mode $\mu = 40\%$, crack length measured by markers versus applied displacement . . . 54
4.29 Mixed Mode $\mu = 40\%$, ERR. Critical value at crack initiation and evolution with crack propagation . . . 55
4.30 Mixed Mode $\mu = 40\%$, bridging tractions in the middle of the crack at $\triangle a = 20mm$ 56
4.31 Mixed Mode $\mu = 40\%$, strains measured by Multiplexed FBGs as a function of the applied displacement . . . 57
4.32 Mixed Mode $\mu = 40\%$, crack length versus applied displacement measured by side markers and FBGs . . . 57
4.33 Mixed Mode $\mu = 40\%$, shifted FBGs strains to common crack tip position . . . 58
4.34 Mixed Mode $\mu = 60\%$, average load-displacement curve and standard deviation . 59
4.35 Mixed Mode $\mu = 60\%$, crack length measured by markers versus applied displacement . . . 59
4.36 Mixed Mode $\mu = 60\%$, ERR. Critical value at crack initiation and evolution with crack propagation . . . 60
4.37 Mixed Mode $\mu = 60\%$, bridging tractions in the middle of the crack at $\triangle a = 20mm$ 60
4.38 Mode II 4ENF setting. Specimen and embedded optical fiber . . . 61
4.39 Mode II, average load-displacement curve and standard deviation . . . 62
4.40 Mode II, crack length measured by markers versus applied displacement . . . 62
4.41 Mode II ERR. Critical value at crack initiation and evolution with crack propagation 63
4.42 Mode II, no bridging tractions in the middle of the crack. Picture taken by opening the specimen in Mode I after the 4ENF test . . . 63
4.43 Mode II, strains measured by Multiplexed FBGs as a function of the applied displacement . . . 64
4.44 Mode II, shifted FBGs strain to common crack tip position . . . 64
4.45 ERR at crack initiation as a function of mode mixity $\mu[\%]$ . . . 65
4.46 Bridging contribution G_b as a function of mode mixity $\mu[\%]$ . . . 66
4.47 Bridging fibers involved during the delamination process, for different mode mixities . . . 67
4.48 ERR curves for different mode mixities, as a function of the crack propagation . 68

5.1 Optimization scheme for the evaluation of bridging tractions 71
5.2 FE Model for bridging identification in Mode I delamination 72
5.3 Axial strain profile over the bridging zone measured by the FBG sensors: (a) schematic view (b) actual FBGs strains 73
5.4 Evolution of the bridging parameters during the optimization process 73
5.5 Fitting of the objective function 74
5.6 Optimized cohesive law for Mode I delamination 75
5.7 Cohesive law with linear decay 82
5.8 Evolution of $\mu(\beta)$, comparison between equations 5.22 and 5.37 89
5.9 Schematic cohesive law for Mixed Mode conditions 90
5.10 Critical ERR at initiation as a function of β 91
5.11 Mixed Mode stress at damage initiation $\sigma_{m,i}$ as function of β 92
5.12 Cohesive law for a constant β value: definition of the bridging parameters 92
5.13 Evolution of $G_b(\beta)$ as a function of β by equation 5.39 94
5.14 Evolution of $\sigma_{max}(\beta)$ as a function of β by equation 5.40 94
5.15 Evolution of $\delta_f(\beta)$ as a function of β by equation 5.41 95
5.16 3D cohesive law as a function of β 96
5.17 FE Model for Mixed Mode delamination 97
5.18 β curves associated to the first six cohesive elements as a function of the COD $\delta_m = \sqrt{\delta_3^2 + \delta_1^2}$ for a 40% Mixed Mode FE Model 99
5.19 β curve associated to the first cohesive element as a function of the applied displacement for a 40% Mixed Mode FE Model 100
5.20 β curve associated to the first cohesive element as a function of the applied displacement for a 40% Mixed Mode FE Model 101
5.21 Definition of $D\,|_{\sigma_{max,b}}$ at a constant β 103
5.22 Fortran® sub-routine called by Abaqus® to control the evolution of β^* 103
5.23 Evolution of β^* versus applied displacement by using the external routine for a 40% Mixed Mode model 104
5.24 Evolution of β for six different cohesive elements versus applied displacement by using the external routine for a 40% Mixed Mode model 105
5.25 Mixed Mode optimization scheme 107
5.26 Evolution of the Mixed Mode bridging parameters along the optimization process 108
5.27 Comparison between the strains measured by the ten FBGs and the ones obtained by the FE Model for $\mu = 20\%$ after the optimization process: (a) all the FBG sensors (b) three FBG sensors 109

5.28 Load-displacement curve for Mixed Mode 40%, mismatch of the maximum load at crack initiation of the numerical model based on a B-K relationship with $\eta = 1.61$ 110

6.1 Mode I, comparison between experimental and numerical load-displacement curves 112
6.2 Mode I, comparison between experimental and numerical crack length-displacement curves 113
6.3 Mode I, comparison between experimental and numerical ERR curves 114
6.4 Mixed Mode 20%, comparison between experimental and numerical load-displacement curves 116
6.5 Mixed Mode 20%, comparison between experimental and numerical crack length-displacement curves 117
6.6 Mixed Mode 20%, comparison between experimental and numerical ERR curves 117
6.7 Mixed Mode 20%, comparison between the experimental FBGs and the corresponding *FEM 1* numerical strain curves, (a) all the FBG sensors (b) three FBG sensors 118
6.8 Mixed Mode 20%, comparison between the experimental FBGs and the corresponding *FEM 2* numerical strain curves, (a) all the FBG sensors (b) three FBG sensors 119
6.9 Mixed Mode 30%, comparison between experimental and numerical load-displacement curves 121
6.10 Mixed Mode 30%, comparison between experimental and numerical crack length-displacement curves 121
6.11 Mixed Mode 30%, comparison between experimental and numerical ERR curves 122
6.12 Mixed Mode 30%, comparison between the experimental FBGs and the corresponding *FEM 1* numerical strain curves, (a) all the FBG sensors (b) three FBG sensors 123
6.13 Mixed Mode 30%, comparison between the experimental FBGs and the corresponding *FEM 2* numerical strain curves, (a) all the FBG sensors (b) three FBG sensors 124
6.14 Mixed Mode 30%, comparison between the experimental FBGs and the corresponding *FEM 3* numerical strain curves, (a) all the FBG sensors (b) three FBG sensors 125
6.15 Mixed Mode 40%, comparison between experimental and numerical load-displacement curves 126
6.16 Mixed Mode 40%, comparison between experimental and numerical crack length-displacement curves 127

6.17 Mixed Mode 40%, comparison between experimental and numerical ERR curves 127
6.18 Mixed Mode 60%, comparison between experimental and numerical load-displacement curves 128
6.19 Mixed Mode 60%, comparison between experimental and numerical crack length-displacement curves 129
6.20 Mixed Mode 60%, comparison between experimental and numerical ERR curves 129
6.21 Mode II, comparison between experimental and numerical load-displacement curves 130
6.22 Mode II, comparison between experimental and numerical crack length-displacement curves 131
6.23 Mode II, comparison between experimental and numerical ERR curves 131
6.24 Mode II, comparison between the experimental FBGs and the corresponding numerical *FEM 1,2,3* strain curves, (a) all the FBG sensors (b) four FBG sensors . 132

List of Tables

3.1 Material properties 15
3.2 Testing machine displacement rates 19
3.3 MMB setting: C-arm length as a function of the applied mode mixity 21

4.1 Mode I: FBGs positions measured with respect to the edge of the specimen on the crack side 39
4.2 Mixed Mode $\mu = 20\%$, FBGs positions measured with respect to the edge of the specimen 46
4.3 Mixed Mode $\mu = 30\%$, FBGs positions measured with respect to the edge of the specimen 51
4.4 Mixed Mode $\mu = 40\%$, FBGs positions measured with respect to the edge of the specimen 56

5.1 Optimized bridging parameters for Mode I delamination 73
5.2 β_b values obtained by the FE Model 104
5.3 Bridging parameters $\xi_i = \left[\xi_{G_b}, \xi_{\sigma_{max}}, \xi_{\delta_f}\right]$ obtained from the optimization process 106

List of symbols

B	Specimen width
C	Compliance
E_i	Young's Moduli in i-direction
F	Error function
G	Shear Modulus
P	Reaction force
U	Strain Energy
a	Crack length
a_0	Initial Crack length
h	Half specimen thickness
G_c	ERR at damage initiation in Mixed Mode
G_{Ic}	ERR at damage initiation in Mode I
G_{IIc}	ERR at damage initiation in Mode II
G_b	Experimental bridging energy contribution
$G_{b,mode\ I}$	Experimental bridging energy contribution in pure Mode I
$G_{b,30}$	Experimental bridging energy contribution at $\mu = 30\%$
n	Refractive index
Λ	Bragg grating period
Π	Potential Energy
Ψ	Total Energy
δ_m	Magnitude of Crack Opening Displacement
δ_f	Magnitude of Crack Opening Displacement at failure
ε	Strain
λ_B	Bragg reflected wavelength
$\Delta\lambda_B$	Bragg reflected wavelength variation

ν	Poisson's Ratio
σ	Stress
σ_c	Generic stress at damage initiation
$\sigma_{3,0}$	Stress at damage initiation for normal openings
$\sigma_{1,0}$	Stress at damage initiation in shear
μ	Energy mode mixity
β	Displacement mode mixity
β_b	Constant displacement mode mixity in the bridging zone
$\beta_{b,30}$	Constant displacement mode mixity in the bridging zone at $\mu = 30\%$
β_{end}	Displacement mode mixity when $G_b(\beta_{end}) = 0$
η	Exponent of the B-K relationship
D	Damage parameter for cohesive elements

Chapter 1

Introduction

1.1 Motivation

The research for innovative materials is always one of the main and fascinating topics since it is strictly related to the new challenges that the extreme engineering is called to overcome. Engineers, physicists and chemists deeply affected the whole world by their improvements and discoveries over the years. In this panorama, composite materials represent one of the most important challenges, since the topic is still relatively recent and has a strong potential for current and future applications.

Fibre Reinforced Polymers (FRP) are receiving more and more attention due to their superior mechanical properties. This kind of composite material is widely used for several applications such as sport equipment, prosthesis for health care, automotive, aerospace, boats, wind turbines, civil structures, etc. Nowadays, we can find it also in the daily life when we use a tennis racket, if we wear a helmet, if we ride a racing bike or even if we carry a luggage.

The improved mechanical properties combined with low weight, high stiffness, the incoming reduction of raw material costs and the increase of automation, are the reasons why composite materials are replacing steel, iron and aluminum over a wide range of applications. Comparing with iron, composite Young's modulus is lower (half or less) but the density can be five times lower and the ultimate strength can reach 2000MPa. This allows designing structures keeping the same stiffness and with an impressive reduction of weight.

Composite materials are created by stacking fibre layers followed by a curing, which allows for resin polymerization. The most common reinforcements are carbon, glass or natural fibres mixed with epoxy or polyester resin. The intrinsic anisotropy of the composite materials allows for designing optimized geometries by combining layers with different fibers orientation, obtaining the best mechanical properties along the desired direction, according to the external loads.

Composite production is mainly made by hand due to the complexity of the process. This allows fabricating very complicated geometries but it also involves drawbacks such as scatter on the final quality and high costs, due to the high working time. If simple parts are needed, automatic systems can be used, such as injection moulding and hot press with the counterpart of high initial costs required for the production chain.

Despite the impressive mechanical properties, composite materials are prone to delamination which may lead to loss of structural integrity and premature failure. Delamination is a common process which involves layered structures and consists in the separation of two adjacent layers. This phenomenon can be caused by impacts, stress intensification and, in general, by critical tensile or shear local stresses. Delamination often represents the weakest link for structures made of carbon FRP, despite the superior mechanical characteristics of the fibres themselves. This kind of failure is potentially very dangerous since it may occur inside the composite without any external evidence.

Delamination may start in three different fracture modes. Mode I represents the normal opening of the crack, Mode II the shear component and Mode III the tearing [1, 2].. All these fracture modes have been extensively studied during the years in terms of crack initiation and, in case of Mode I, also bridging contribution.

Since composite structures are often subjected to tensile and shear loads, a complete study of delamination under Mixed Mode conditions is mandatory. Up to now, as shown in the ASTM, only the critical energy at crack initiation is used to design composite structures but no predictions are available about crack propagation with bridging. In order to obtain a complete overview of the crack propagation and to provide additional information about composite toughness under Mixed Mode conditions, large scale bridging effects must be characterized.

This work aims to provide the experimental fracture initiation values for unidirectional CFRP and to reveal an innovative numerical tool able to model the whole fracture propagation, adding the proper bridging contribution over a wide range of different mode mixities.

1.2 Objectives

A complete characterization of the delamination process in Carbon Fiber Reinforced Polymers (CFRP) under Mode I and Mode II conditions has been already studied, both in terms of crack initiation and bridging contribution [3]. It is well described the important influence of bridging in Mode I and its absence in pure Mode II delamination. In the first case, bridging contribution is extensive, heavily conditioning the crack propagation and the local stresses. For a typical Double Cantilever Beam (DCB) test, the amount of energy provided by the bridging tractions deeply affects the load-displacement curves and slows down the crack propagation, due to the

increase of fracture toughness. In the second case, a four-point bend End Notched Flexure test (4-ENF) shows the absence of bridging, revealing a flat energy release rate (ERR) and, therefore, no toughening processes acting during crack propagation.

The objective of this work consists in obtaining a whole characterization of the delamination process in Mixed Mode, both in terms of fracture initiation values and bridging contribution. In order to achieve this objective, several steps must be completed, such as:

- Validate of Mixed Mode Bending setting (MMB), used to impose the required mode mixity during the experiments.
- Stability check of crack propagation over different mode mixities.
- Calculate the ERR at initiation G_c according to the ASTM specifications.
- Embed multiplexed Fiber Bragg Grating sensors (FBGs) in the carbon specimens, in order to measure the internal strains and, indirectly, to obtain the corresponding bridging tractions acting on the crack plane.
- Validate of a numerical Finite Element Model (FEM), by using cohesive elements, able to simulate the crack propagation over a wide range of mode mixities, taking into account the corresponding bridging contribution.
- Find a correlation between the angle β, which represents the orientation of the bridging tractions due to the presence of shear and tensile components, and the global mode mixity.

1.3 Outline

In Chapter 2, literature about Mode I, Mode II and Mixed Mode delamination, fibre bridging and optical fibers is reviewed. This represents the state of the art of the actual research and the basis to start our work.

Chapter 3 combines all the main practical aspects: it describes the material manufacturing, the measurement systems, the testing machine, the working principle of the FBG sensors and the cohesive elements.

Chapter 4 discusses the experimental results obtained in pure Mode I, Mixed Mode at 20%, 30%, 40%, 60% and pure Mode II. The influence of the applied mode mixity on the fracture toughness G_c and on the corresponding bridging contribution is analyzed. These results represent the basis to implement a numerical model.

Chapter 5 describes the numerical model. It provides a detailed overview about the standard Mixed Mode numerical approaches, revealing their limitations and issues, and describes an innovative cohesive law formulation which better represents the experimental results.

In Chapter 6 a complete comparison between the experimental results and the numerical ones obtained by using three different approaches is shown. This part well points out that the standard FE Models are not suitable to properly represent the experimental curves and the development of bridging tractions.

Chapter 7 includes the conclusions and the main goals of this work, combined with the suggestions for a future development.

Chapter 2

State of the art

Delamination in composites is still a challenging topic in mechanics and materials research field. Several studies have been published up to now with the target of obtaining a better understanding about the mechanisms which control the propagation of delamination. This chapter aims to provide a complete overview of the current literature about Mode I, Mode II and Mixed Mode delamination, plus the bridging tractions and their contribution to fracture toughness. The Fiber Bragg Grating sensors are also described since they represent a fundamental and innovative tool extensively employed in this work, which allows to shed light on the delamination process.

2.1 Delamination in composites

An extensive amount of literature on delamination in composites and the correlating results is provided by review papers [4, 5] and textbooks [6]: the fracture mechanics theory is fundamental for an in depth comprehension of the topic [2, 7].

Delamination in composites can occur for several different reasons reducing the stiffness and the reliability of the components. Damage initiators are represented by drilled holes [8], local impacts or internal defects [9, 10, 11]. The fact that composite materials are nowadays widely used, makes delamination a hot topic, for all the researchers involved [12, 5].

The initiation of delamination and its propagation are influenced by several parameters, such as ply thickness and fibers orientation [13, 14]. The Young's modulus is another important parameter to take into account since it has been shown that fracture toughness under Mode I and Mixed Mode conditions decreases as the fibre modulus increases [15]. Fatigue and monotonic loading need to be separated since, in composite materials, they may cause a different behavior in terms of delamination process and damage initiation [16, 17, 18]. Temperature and moisture

also have an important influence and must be kept under control in order to obtain repeatability on the experimental results [19].

A fundamental approach to describe, analyze and predict delamination is represented by the numerical simulation based on the Finite Element Method (FEM) [20]. By using the virtual crack closure technique [21], we are also able to calculate both the energy release rate and the mode mixity. In order to simulate a crack propagation, cohesive elements provide an extremely interesting tool for several different delamination cases [22, 23]. Cohesive elements are placed in the crack propagation path and their behavior is set by multiple parameters such as the initial stiffness, the ultimate strength, the corresponding energy and the linear or exponential stress degradation. All these parameters are chosen according to the material properties and fracture modes [24, 25]. This kind of approach, thanks to its flexibility, is used to simulate the delamination process under Mode I, Mode II and Mixed Mode conditions, both for monotonic and fatigue loads [26, 27].

2.2 Delamination tests

During the past years, specific tests and settings have been developed for Mode I, Mode II and Mixed Mode delamination tests, in order to standardize and compare the final results in terms of ERR. Brunner et al. [28] reviewed several methods for testing the fracture toughness.

In case of Mode I delamination, the Double Cantilever Beam setting (DCB) is widely used and accepted as a reference. The specimen is symmetrically loaded at the end of the beam. Load, displacement and crack length are simultaneously monitored. The corresponding ASTM standard [29] describes in detail all the steps to be followed to perform a quasi-static delamination test. Another standard [30] has been developed for Mode I fatigue tests. An analytical model, able to represent the phenomenon, is well described by Camanho et al [31]. A close analytical solution to calculate the stress intensity factors for a double cantilever beam is also present in literature [32]. A correction in the calculation of the G_{Ic} must be also taken into account since the assumption that the two beams behave as a built-in cantilever is not accurate [33].

A standardized procedure for Mode II delamination is still lacking. Problems related with crack growth and position monitoring are the main reasons why an accurate calculation of G_{IIc} is not trivial. If in Mode I tests the crack tip is clearly visible, with pure shear the crack detection is more problematic [34]. There are three fundamental experiments to measure G_{IIc}. The first and most common is the End Notched Flexure test (ENF) [35, 36], initially developed for wooden materials characterization. It is easy to implement since it consists in a three point bending test but the disadvantage is represented by an unstable crack propagation and a non-constant flexural moment over the crack path. In order to improve the stability of crack propagation,

some changes have been proposed [37]. Another setting to characterize Mode II delamination, called End Loaded Split test (ELS), is based on a cantilever beam geometry which provides a larger range for crack propagation [38]. A third method is represented by the four-point End Notched Flexure test (4ENF) which allows for a constant moment zone between the two upper pins and, therefore, for a more stable crack propagation [39, 40]. The 4ENF setting has been used in this work for the characterization of Mode II delamination. For the aforementioned tests, friction contribution must be also taken into account [41, 42].

A Mixed Mode delamination setting is been recently standardized to determine the interlaminar fracture toughness of unidirectional fiber composites [43]. In the past years, a large amount of different settings to perform Mixed Mode tests has been presented, trying to find a combination between Mode I and Mode II setup. Figure 2.1 shows all the different types of apparatus for Mixed Mode delamination tests. The Cracked Lap Shear setting (CLS) is composed of a specimen where the load is applied to a single arm [44, 45]. The Edge Delamination Tension (EDT) specimen combines Mode I and Mode II contributions due to the particular layer layup ($\pm$ 35/0/90) and the consequent mismatch in the Poisson's ratio [46]. Another Mixed Mode test is represented by the Arcan configuration, where the specimen is bonded to a rigid support and then loaded with different angles in order to produce the desired mode mixity [47]. A variation of the standard DCB test has been proposed by Bradley and Cohen [48], consisting in a different loading system for the two beams. A wide range of possible Mixed Mode conditions can be achieved from pure Mode I to pure Mode II. Another Mixed Mode setup is proposed by Russell and Street [19], who fabricated unsymmetrical specimens to impose a local mode mixity. Several different settings and analytical methods implemented to obtain the critical energy at crack initiation in Mixed Mode have been explored and reviewed by Hashemi [49], splitting the critical energy G_c into the corresponding Mode I and Mode II components. The last and currently most used setting, able to reproduce a wide range of Mixed Mode conditions, is represented by the Mixed Mode Bending test (MMB) developed by Reeder and Crews [50]. Starting from a three point bending configuration, an upper bar is added in order to allow for the Mode I component. Pure Mode II is obtained if the load is placed over the central pin while pure Mode I is reached when the crack front reaches the last pin. This means that, by changing the lever arm length, it is possible to apply a full range of Mode I/II ratios. Stability and instability of crack propagation are a function of the initial crack length and applied mode mixity. Additional attempts, aiming to improve the stability of the crack propagation, are described by Martin and Hansen [51].

In order to develop a criterion able to predict the failure under different Mixed Mode conditions, by collecting the experimental data from pure Mode I/II tests and the intermediate mode mixities, a lot of effort has been devoted during the past years. A classic form based on energy

release rate [52, 53], able to predict the delamination initiation, is expressed as:

$$\left(\frac{G_I}{G_{Ic}}\right)^m + \left(\frac{G_{II}}{G_{IIc}}\right)^n + k\left(\frac{G_I}{G_{Ic}}\right)\left(\frac{G_{II}}{G_{IIc}}\right) = 1 \tag{2.1}$$

where m,n and k are coefficients to be determined from the experimental results. Another criterion developed by Benzeggagh and Kenane [54], aims to fit the experimental critical energies G_c as a function of the applied mode mixities μ, by using the following formula:

$$G_c = G_{Ic} + (G_{IIc} - G_{Ic})\mu^\eta \tag{2.2}$$

where $\mu = {}^{G_{II}}/_{(G_I+G_{II})}$ represents the mode mixity and η the fitting parameter.

2.3 Bridging and cohesive law

When a delamination propagates in a unidirectional carbon fiber composite material, it is common to see fiber bundles bridging the crack faces. In this case, the delamination involves a first narrow process zone which represents the cracked matrix zone failure plus a second larger region in which bridging fibers cross the crack front, providing additional tractions. This phenomenon, called *fibre bridging,* provides an additional energy to be dissipated during the crack propagation, thus acting as a toughening process. The reasons and the way how fibers pull-out develops can be determined by studying the micro-mechanical processes, close to the crack tip. Defects, porosity, layers compaction and moisture may affect the amount of bridging developed during the delamination process [55]. A review article by Bao and Suo describes several aspects involved in the bridging development [56].

By implementing a micro-mechanical model, the shape of the bridging tractions has been established. Highest normal stresses act very close to the crack tip while they quickly decrease as the crack opening displacement increases [57, 58]. In case of small scale bridging and uniform tractions, the Dugdale model is adequate but it fails if large scale bridging occurs [59].

Experimental observations show that fibers misalignment in composites influences the bridging process and, consequentially, the corresponding energy contribution. Specimen geometry effects are also important [60].

The bridging tractions, acting between the crack faces, can be derived by using indirect methods, by experimentally measuring the crack opening displacement (COD) or the strains over the bridging zone [61, 62, 63, 64].

Delamination can also occur in z-pinned laminates. This technique aims to increase the fracture toughness, introducing fibers in an out of plane direction, which link two adjacent layers. It is shown that a bi-linear cohesive law well describes the delamination process in terms

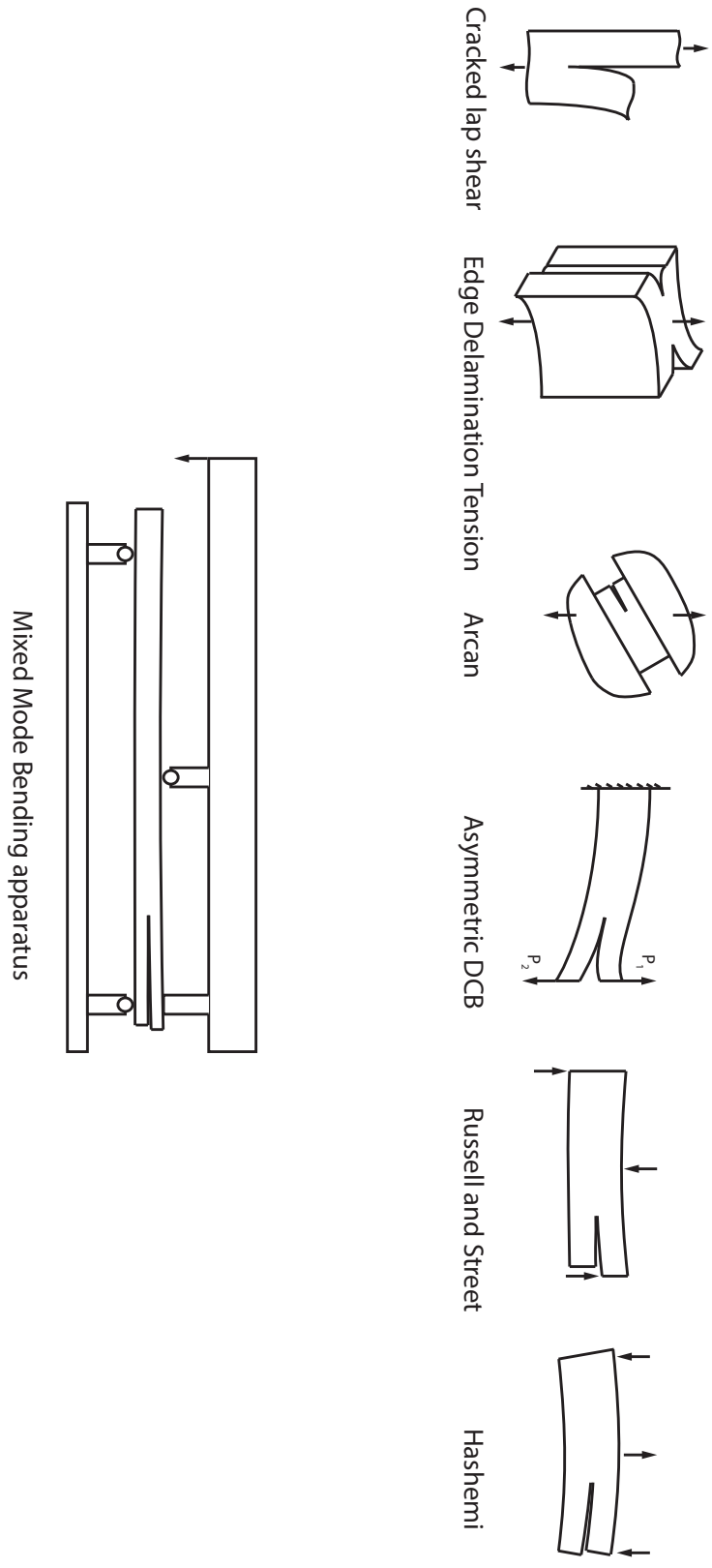

Figure 2.1: Mixed Mode apparatus

of load-displacement curves and ERR [65, 66]. This kind of approach is used and checked for Mode I, Mode II and Mixed Mode delamination [67, 68, 69].

2.4 Fiber Bragg Grating sensors

Optical Fiber Bragg Grating sensors (FBGs) have received a lot of attention during the past years due to their innovative characteristics, to measure strains and temperature variations in composite materials. The Bragg grating consists in a periodic variation of the refractive index along the optical fiber, so that if a broad band source light travels through it, a narrow part of the whole spectrum is reflected. Discovered and developed by Hill et al. in 1978 [70], the sensor works as a spectral filter, changing characteristics when a variation of strain or temperature is applied. The reflected spectrum is centered in the so-called Bragg wavelength. A very important contribution to the optical Bragg fibers development comes from Meltz et al. [71], who managed to introduce the grating by using a phase mask.

FBG sensors have been used for multiple purposes, such as the monitoring of composite materials during the curing process [72], the moisture absorption and hygrothermal aging in epoxy [73, 74], the presence of local damages due to impacts [75, 76], the measurement of strains for nautical applications [77] or to detect acoustic emissions [78]. FBGs are also used for structural health monitoring for aerospace/aeronautical applications [79, 80, 81].

Review articles are also available to get additional information about the optical theory [82, 83].

Optical fibers are often embedded in composite materials and used as strain gauges. This means that optical fibers act as an inclusion for the surrounding material. It is shown that the optical fibers, due to the small diameter equal to $125\mu m$, do not influence the crack propagation and the ERR, in particular if they are embedded in the direction of the reinforcing fibers and if the ply thickness is higher than the optical fiber diameter. A good compromise is to embed the optical fiber at distance from the crack plane at least double than the fiber diameter [84]. Influences, due to the presence of optical fibers, are verified when they are embedded too close to the crack plane, in particular in case of fatigue tests and in cross-ply laminates [85, 86, 87, 88].

2.4.1 Multiplexed sensing

FBG sensors represent a very interesting tool, able to accurately measure strains or a temperature variation. A main limitation consists on the fact that, in a real structure, there are several different spots to be monitored while the optical fibers provide the measurement just in a single spot. There are two different ways to measure strains at the same time over different locations,

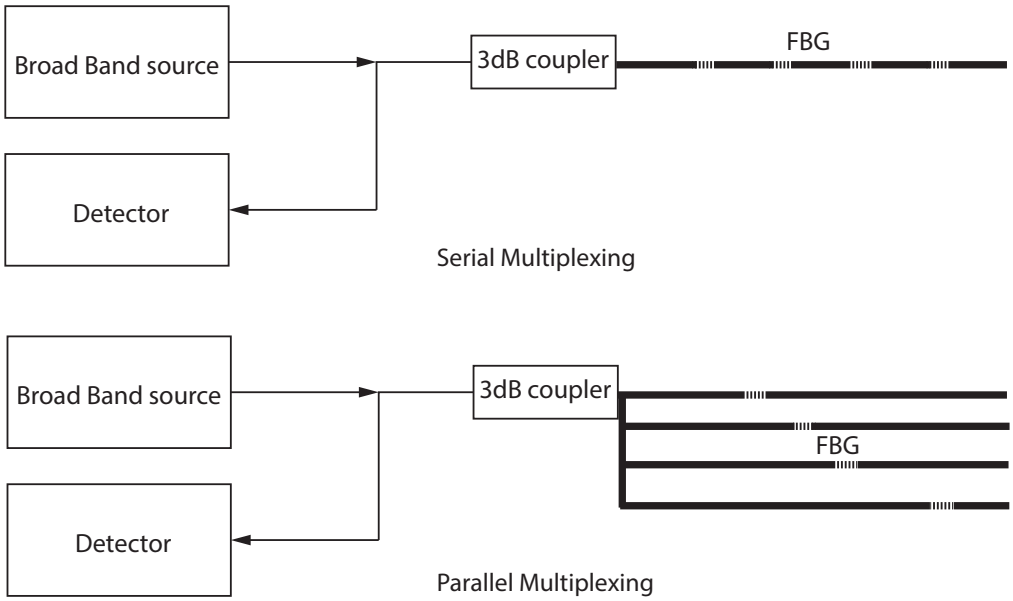

Figure 2.2: Multiplexed sensing, serial and parallel scheme

by using a parallel or a serial approach [89, 81], as shown in Figure 2.2.

Both schemes work by using a single broad band light source and detector. In the parallel scheme, the source light is split through different fibers and the reflected spectra are coupled and detected at the same time. This technique allows for measurements in different locations of the structure, even far from each others, but it increases the inclusions due to the optical fiber presence.

In the serial one, the light propagates through a single fiber where multiple Bragg gratings are inscribed. In this case, only one fiber is needed, reducing the issues related to the presence of several optical fibers embedded. A drawback is that strains are measured only over the fiber path [90].

In both cases, serial and parallel, the Bragg gratings inscribed must reflect different wavelengths in order to avoid overlaps on the reflected spectra and, thus, issues on the peak detection computed by the electronic device. Note that, too close reflected wavelengths may bring to an overlap during the acquisition process, due to different strain profiles over the sensors array.

The spatial distance between two Bragg sensors can be reduced up to $2mm$, while the sensor length up to $1mm$. Such a spatial resolution, combined with the possibility to have several sensors over a single fiber, allows for measuring the strain profile over very small regions.

2.5 Summary

Composite materials, due to their increased importance in multiple applications and the issues represented by their brittle failure, still represent a very interesting and challenging research field for worldwide engineers. Several efforts have been devoted to study Mode I and Mode II delamination processes by using advance measurements techniques and numerical simulations. Nonetheless, an important contribution must be still provided to better characterize the Mixed Mode delamination, especially if large scale bridging occurs. The delamination tests performed in Mode I, Mode II and Mixed Mode, the optical fibers equipped with Bragg grating sensors and the numerical models, represent the basis to shed some light on this challenging topic.

Chapter 3

Materials and methods

The goal of this chapter is to provide the fundamental information about the materials and techniques used during the whole project. In particular the specimens preparation, material layup, the main steps to properly embed the optical fiber, the experiments definitions and the data reduction are described. This part is essential due to the important influence on the repeatability of the final results. Finally, an introduction to cohesive elements involved in the numerical model is presented.

3.1 Material properties, manufacturing and testing parameters

The material used for the tests described in this work consists in unidirectional carbon fibre layers combined with epoxy resin SE 70 from Gurit SP^{TM}. It comes as prepreg, which means the resin is already mixed with carbon fibers. The use of prepregs is very common and useful when strong process reliability is required, since the resin amount is fixed and homogeneous, unlike the wet layup where the operator is in charge to manually distribute the resin. The fibre volume ratio after curing is kept constant over all the different fabricated batches. The material comes as a big roll protected by a plastic film on both sides in order to avoid any contamination with moisture or dust. To improve the protection against moisture contamination, the roll is stored in an additional external sealed bag and vacuum is applied. These precautions are fundamental since a moisture contamination can deeply affect the delamination behavior, preventing the possibility to compare the experimental results obtained from different batches. The carbon roll is finally stored in a fridge at -18°C, up to the expiring date.

Specimens are prepared by stacking 20 layers of carbon-epoxy prepreg. The roll is cut into sheets of $200 \times 200mm$. The single layer thickness $\backsim 0.2mm$ is approximately provided by the material data sheet, thus a plate $\backsim 4mm$ thick is normally obtained. All the layers are stacked

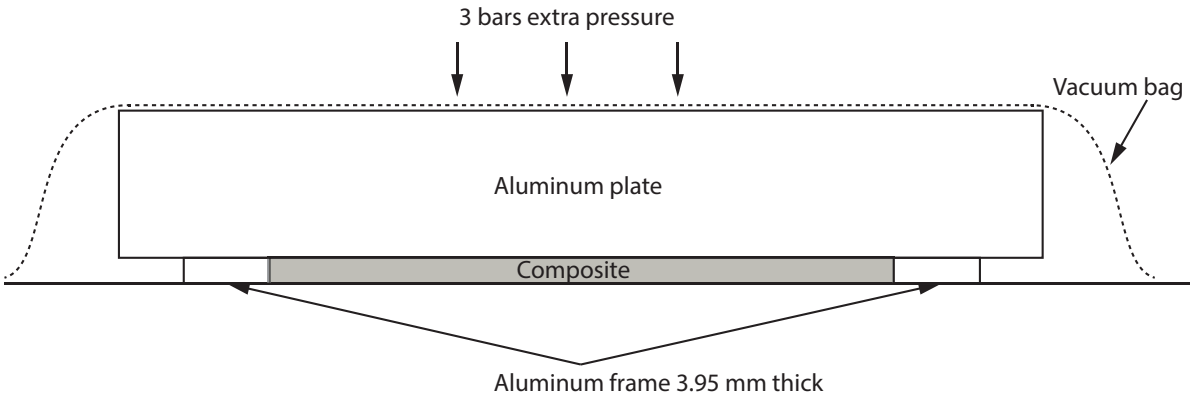

Figure 3.1: Material manufacturing, layout for curing in autoclave

sequentially with the same fiber direction. Vacuum is applied every five layers for ten minutes to remove air bubbles and improve material compaction. A PTFE film 13μm thick and 50mm long is placed in the middle of the stacking sequence, between layer 10 and 11, in order to create a crack initiator. This material allows the perfect separation of the two crack faces since it doesn't react with the epoxy resin.

Once the stacking sequence is completed, the material is placed on the autoclave hot plate, using a release film as support. The exact final thickness is obtained by using a surrounding aluminum frame 3.95mm thick and a very rigid aluminum plate on top. The plate rests on the external frame and on the material at the same time, improving compaction and final surface quality as shown in Figure 3.1. The vacuum bag is finally added to improve compaction and remove bubbles during the curing process. Once all the steps are correctly completed, the autoclave is turned on and temperature is properly set according to the material data sheet. Figure 3.2 shows the whole curing cycle, with an initial temperature ramp and a plateau kept for 13 hours. The initial ramp is very slow to allow a homogeneous heat flow through the thickness. Two additional thermocouples are added to monitor the temperature over different regions of the plate. In addition to the vacuum, which is kept all over the curing cycle, 3 bars extra pressure is applied. After several pilot tests and attempts, the described fabrication setting is found to be the best in terms of quality and reproducibility.

The quality of the plate after curing and the repeatability of the process is mandatory to compare strains, load profiles and fracture behavior for specimens coming from different batches. In order to reach such a goal, several attempts have been made to check the influence of parameters such as frame thickness and extra pressure. Figure 3.3 shows two transverse sections of the cured material, obtained by a high resolution microscope able to capture the presence of voids and compaction quality. In Figure 3.3(a) the material is fabricated with a 4.05mm frame

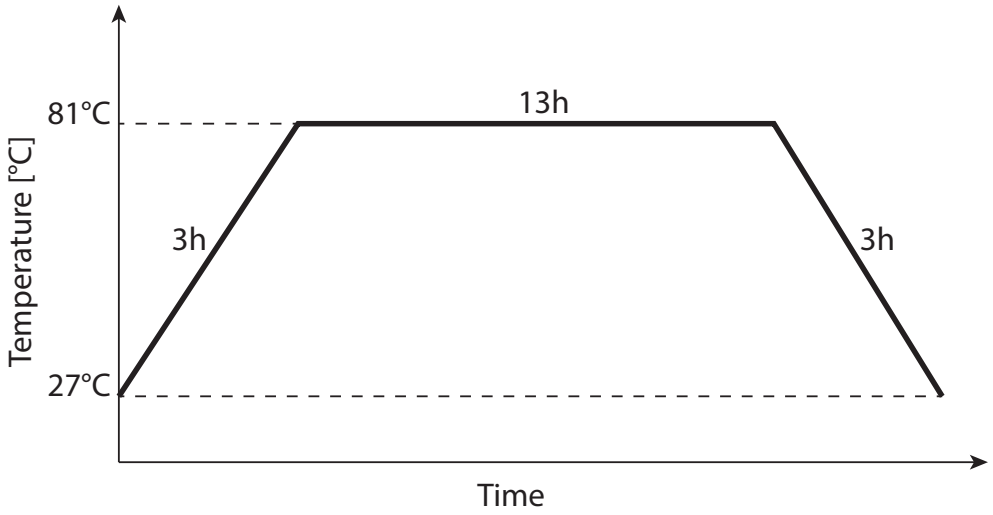

Figure 3.2: Curing cycle for composite fabrication. Vacuum and 3 bars extra pressure applied

	E_1 [MPa]	E_2=E_3 [MPa]	υ_{12}=υ_{13}	υ_{23}	G_{12} = G_{13}[MPa]	G_{23} [MPa]
Composite	118700	7725	0.314	0.427	3837	3121

Table 3.1: Material properties

thickness and applied vacuum during the curing, while Figure 3.3(b) shows a plate made by using $3.95mm$ frame thickness and 3 bars extra pressure to improve the compaction. In the second case, the amount of internal voids is almost negligible and the compaction of the layers is also improved. The difference between the two techniques is significant and it shows how much attention must be paid during the whole fabrication process to assure such a quality result.

The final thickness of the plate is $3.9mm$. This is found to be well reproducible between different batches. The small difference with the aluminum frame thickness is due to the thermal shrinking after curing.

Once the fabrication process is defined, tensile and bending tests are carried out in order to obtain the material properties such as the elastic and shear moduli and the Poisson's ratio. Table 3.1 shows the material properties obtained from the experiments and then used for the numerical models.

The optical fibers used during the tests are wavelength multiplexed, composed by ten Bragg gratings. These gauges reflect ten different wavelengths of the coupled broadband light source. This gives the opportunity to obtain information about local strains in different regions at the same time during the delamination test. In this specific case, the distance between each sensor is $3mm$ and the Bragg grating length is only $1mm$, which allows a very local measurement.

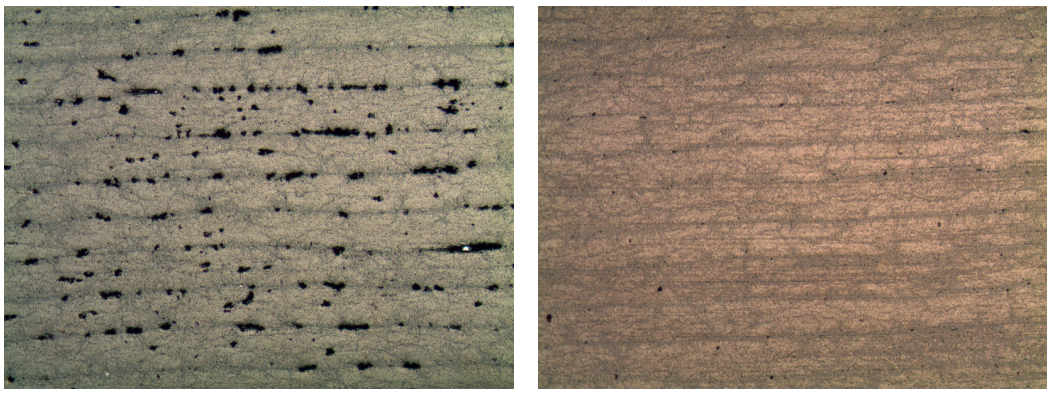

(a) (b)

Figure 3.3: Transverse sections of a carbon plate fabricated with (a) 4.05mm frame thickness and applied vacuum, (b) 3.95mm frame thickness, vacuum and 3 bars extra pressure

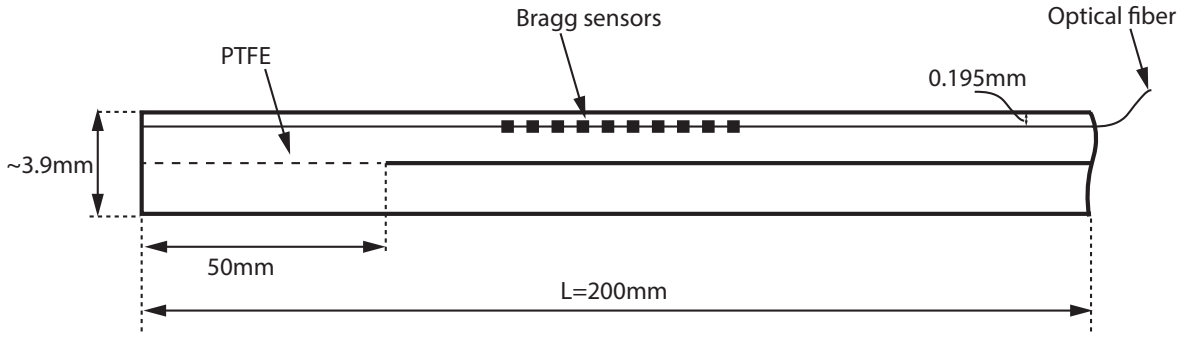

Figure 3.4: Schematic layout of a specimen with embedded optical fiber

The fabrication with embedded optical fibers requires additional precautions. The FBG sensors are surrounded by an external coating all over the fiber for better handling toughness. By using sulfuric acid, the coating is removed over the Bragg grating region to obtain a better adhesion with the surrounding material, improving the measurement accuracy. After this step, the fiber is placed on the prepreg, setting the required sensors position. The optical fiber is placed between layer 19 and 20, which means 9 layers over the crack plane. This position is chosen as a compromise between the requirement of measuring very local strains close to the crack tip and to avoid local discontinuities, due to the presence of bridging fiber bundles pulled out. On the edge of the plate, the exit points of the optical fibers are covered by shrinkable sleeves to protect them from fracture. The connectors are covered by L-shape metallic profiles. The schematic layout of the embedded optical fiber in the specimen is shown in Figure 3.4.

Figure 3.5 displays a polished cross section of a specimen with an embedded optical fiber.

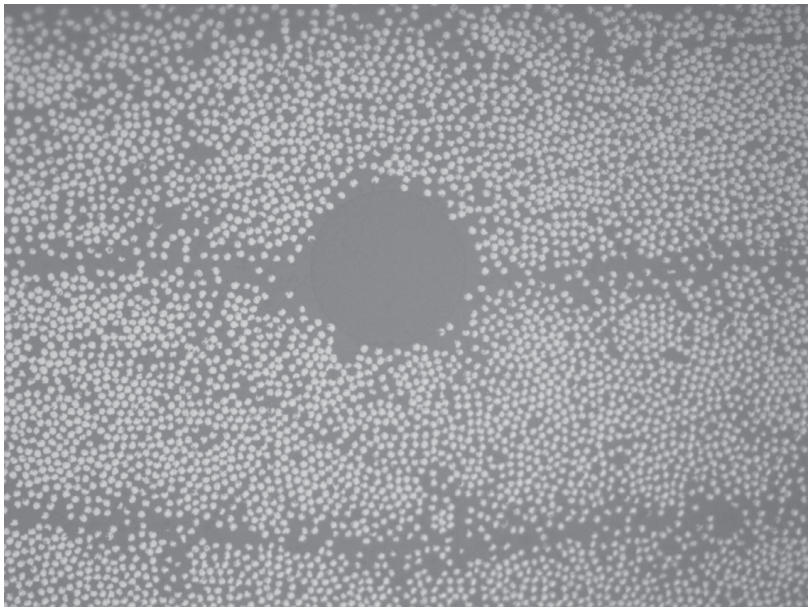

Figure 3.5: Specimen cross section with an embedded optical fiber

The FBG sensor is placed between two layers and well surrounded by carbon fibers. In this section no relevant voids, which may affect the measurement, are present close to the optical fiber.

3.1.1 Specimen preparation

The $200 \times 200mm$ unidirectional carbon plate, at the end of the curing process, is cut by using a diamond disc to obtain specimens of $25mm$ in width. The presence of water during the cutting procedure assures low local temperatures and allows for reducing the amount of carbon particles for health reasons. Each specimen side is painted white by an ultra-thin acrylic layer. Markers, obtained by scratching the white paint with a sharp blade, are added every $1mm$, to monitor the crack propagation during the experiments. In order to connect the specimen to the loading machine, steel blocks are added, differently for Mode I, Mode II and Mixed Mode tests, on the specimen surface by using epoxy resin. The steel blocks, used for Mode I and Mixed Mode tests, have a dimension of $10 \times 10 \times 25mm$ while for the Mode II case the block has a triangular section to constrain the horizontal axis during the bending test. Figure 3.6 shows two specimens for Mode I (a) and Mode II (b) delamination test equipped with the corresponding steel blocks and markers.

Before any test, the crack must be initiated in order to overcome the pop-in effect due to the rich resin zone present at the end of the PTFE film. The specimen is clamped in a vise $4mm$

(a)

(b)

Figure 3.6: Specimens with steel blocks and markers for (a) Mode I and Mixed Mode setting (b) Mode II setting

after the PTFE layer in order to stop any unstable crack propagation and a wedge is inserted to allow the crack to start. This technique allows an accurate control of the initial crack advance and a good repeatability of the process.

If an optical fiber is embedded, attention must be paid to avoid any damage. The fiber is kept in the middle of the specimen width and one side of the optical fiber is cut, which is used as reference to determine the FBG sensors positions, by using an OLCR measurement system, as described in section 3.3.1.

3.1.2 Testing machine and settings

Mode I, Mode II and Mixed Mode bending tests are run on the same Walter+Bai AG EC80-MS® testing machine able to monitor the applied displacement and load. This last is measured by a $1kN$ load cell previously calibrated and no extra moments are applied on it, to ensure the reliability of the measurement. The acquisition sample rate is set to $10Hz$ for all the tests, which is found to be more than sufficient for quasi-static applied loading.

All the tests are performed in constant displacement control. The applied displacement rate is different depending on the delamination tests, since this parameter has an important influence on the crack propagation stability. For Mode I tests, a DCB setting is used and the displacement rate set to $1.2mm/min$ that is in the range $0.5 - 5mm/min$ proposed by the ASTM standards [29]. For Mode II tests there are no standards, thus a lower value equal to $0.6mm/min$ is found to be experimentally suitable to improve the stability of crack propagation by using a 4ENF setting. The stability of crack propagation in Mixed Mode delamination tests strongly depends on the applied mode mixity. Thus, the corresponding displacement rate is changed, from $1.2mm/min$ at $\mu = 20\%$ up to *0.6mm/min* for $\mu = 30\% - 60\%$.

Table 3.2 resumes all the displacement rate values used during the experiments.

Setting test	DCB	MMB	MMB	4ENF
Mode Mixity *[%]*	Mode I	20	30,40,50,60	Mode II
Displacement rate *[mm/min]*	1.2	1.2	0.6	0.6

Table 3.2: Testing machine displacement rates

Mixed Mode Bending setting (MMB), shown in Figure 3.7, is widely described in the ASTM standard [43] which provides all the necessary steps to properly perform the delamination test. Here, the necessary equations, to impose the desired mode mixity by changing the C-arm, are summarized. The C-arm is a function of the material properties, specimen thickness and, obviously, the applied mode mixity as following:

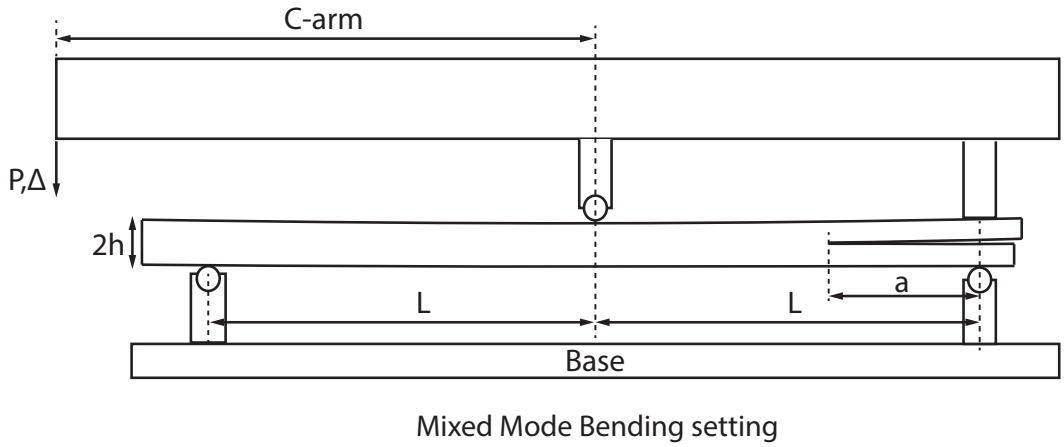

Figure 3.7: Mixed Mode Bending setting

$$C = \frac{12\beta^2 + 3\alpha + 8\beta\sqrt{3\alpha}}{36\beta^2 - 3\alpha} \cdot L \tag{3.1}$$

where L is the half span and α and β are parameters given by:

$$\alpha = \frac{1 - \frac{G_{II}}{G_{tot}}}{\frac{G_{II}}{G_{tot}}} \tag{3.2}$$

$$\beta = \frac{a + \chi h}{a + 0.42\chi h}. \tag{3.3}$$

where h is the half thickness, the term $\frac{G_{II}}{G_{tot}}$ represents the desired mode mixity, a is the crack length and χ is:

$$\chi = \sqrt{\frac{E_{11}}{11G_{13}}\left\{3 - 2\left(\frac{\Gamma}{1+\Gamma}\right)^2\right\}} \tag{3.4}$$

with:

$$\Gamma = 1.18\frac{\sqrt{E_{11}E_{22}}}{G_{13}}. \tag{3.5}$$

In the standard, the half span L is proposed to be $\sim 50mm$, to avoid geometrical non-linearities. In this work, L is set equal to $90mm$ in order to increase the crack propagation range and to better evaluate the bridging contribution. Any non-linearities are verified by the unloading curve at the end of the test, when the applied displacement is maximum. Even if the displacement value is high, the non linearity is found to be negligible as shown in Figure 4.19.

Mix mode conditions	20%	30%	40%	60%
C-arm *[mm]*	178.5	118	91.5	65

Table 3.3: MMB setting: C-arm length as a function of the applied mode mixity

In table 3.3, the C-arm lengths for all the tested mode mixities are collected.

In order to avoid any friction contribution on the loading pins, ball bearings are used and the connections, between the machine and the steel blocks bonded on the specimen, are treated with grease. The displacement is applied on the upper bar in two points, by using a fork. This contact must be perfectly balanced by using thin shims in order to avoid any rotation of the bar and, thus, an uneven crack front.

3.1.3 Crack measurement

The measurement of crack length is obtained by using two high resolution cameras, focused on the markers made on both sides of the specimen. This allows for averaging the crack length value in case of differences between the two sides. The sampling rate is set at $1Hz$, which ensures several images for each crack advance and, therefore, a precision of about $\pm 0.5mm$.

Figure 3.8 shows that the crack profile is not perfectly straight but has a curved shape through the specimen width due to the transition from plane stress to plane strain. Crack length is thus different if measured on the side or in the middle of the specimen. However this difference is small ($\sim 1.5mm$) and is kept constant during the crack propagation. This means that the calculation of ERR is not affected, since it depends on the derivative $\frac{dC}{da}$ and it is not linearly related to the absolute crack length value (see section 3.2).

3.2 Experimental energy release rate

The following explanation is based on Griffith theory [91], the first to assume that the presence of defects inside the material may lead to stress concentrations and premature breakage. Assuming a cracked plate with linear elastic material properties, loaded by a remote load P and with a crack inside, as shown in Figure 3.9, the corresponding total energy Ψ is calculated as [7]:

$$\Psi = \Pi + W_s \tag{3.6}$$

where Π represents the potential energy of the system and W_s is the work spent during crack propagation to create new surfaces. The term Π is defined as:

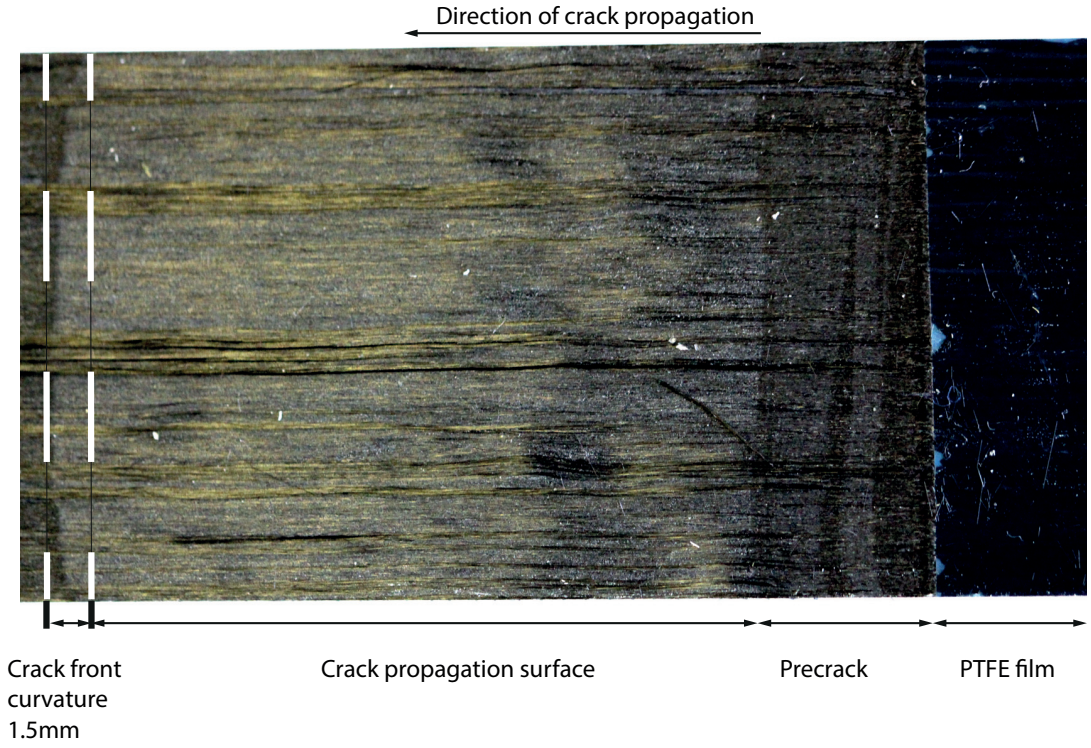

Figure 3.8: Crack front for a Mixed Mode delamination test

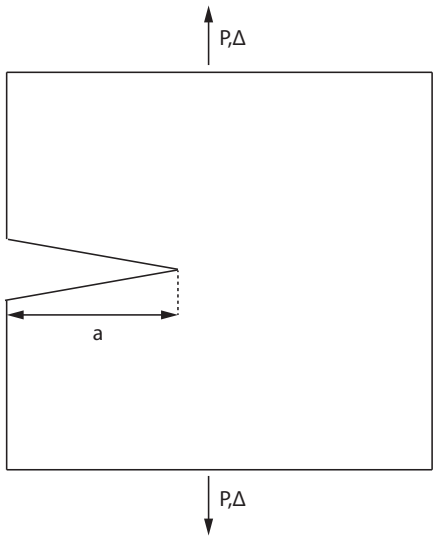

Figure 3.9: Crack in Griffith theory

$$\Pi = U - F \tag{3.7}$$

where U is the strain energy and F is the work provided by the external load P. This can be expressed as:

$$F = P\Delta \tag{3.8}$$

where Δ represents the applied displacement. Since the material is linear elastic, the strain energy can be written as:

$$U = \int_0^{\Delta} P(\Delta) d\Delta = \frac{1}{2} P\Delta \tag{3.9}$$

Substituting the equations 3.8 and 3.9 into 3.7, Π becomes:

$$\Pi = -\frac{1}{2} P\Delta \tag{3.10}$$

The energy derived by the creation of new surface during crack propagation is linearly dependent with the crack length a as following:

$$W_s = 2\gamma a \tag{3.11}$$

where γ is a constant coefficient.

The crack initiation depends on the total energy first derivative with respect to crack surface A and it is defined as:

$$\frac{d\Psi}{dA} = \frac{d\Pi}{dA} + \frac{dW_s}{dA} = 0 \tag{3.12}$$

where $A = a \cdot B$. The condition for an unstable crack involves the second derivative as:

$$\frac{d^2\Psi}{dA^2} = \frac{d^2\Pi}{dA^2} + \frac{d^2W_s}{dA^2} < 0$$

in which the term $\frac{d^2W_s}{dA^2} = 0$ because $\frac{dW_s}{dA}$ is a constant.

The term $-\frac{d\Pi}{dA}$ has been defined as the Energy Release Rate (ERR) by Irwin in 1954 [92], also called *as crack driving force*. It can be written as:

$$G = -\frac{d\Pi}{dA} \tag{3.13}$$

Substituting the equation 3.10 into 3.13, the ERR becomes:

$$G = \frac{P^2}{2B}\frac{dC}{da} \tag{3.14}$$

where the compliance $C = \frac{\Delta}{P}$.

3.2.1 Compliance method

The definition of ERR from equation 3.14 involves the variation of compliance with respect to the crack length. This relation can be derived from the beam theory equation as suggested by the ASTM standards. Unfortunately the analytical approach provides accurate results only for very simple cases and it may be inadequate if bridging, friction or large displacements are present. For this reason, *compliance calibration method* is widely used to obtain the ERR from experimental results. It consists of fitting the experimental compliance versus crack length, by using a 2^{nd} degree polynomial or a power law expression. Since, when derivatives are involved on experimental data, a lot of attention must be paid not to introduce noise and errors, a power law expression with 3 coefficients is used in order to provide the best possible fitting. The compliance expression becomes:

$$C = m + na^{\rho} \tag{3.15}$$

where m, n, ρ are the fitting parameters and a is the crack length.

If the experiment is affected by crack jumps or if the bridging influence is very strong, the compliance calibration may fail. This means that the Equation 3.15 is not able to properly represents the experimental compliance. If this happens, the derivative of the compliance will introduce significant errors in the final ERR calculation. Figure 3.10(a) shows an experimental compliance versus crack length fitted by a 2-terms ($C = na^{\rho}$) and 3-terms ($C = m + na^{\rho}$) power law. Figure 3.10(b) highlights the behavior of the compliance derivatives $^{dC}/_{da}$. Even if the quality between the two compliance fittings doesn't seem to be that different, the derivatives show complete different values causing non-negligible errors on the ERR calculation.

The use of high degree polynomial expressions will improve the fitting quality in terms of total residuals but it also increases local fluctuations, in particular in the first part which strongly affects the derivative. The 3-terms power law is found to be the most reliable expression in terms of fitting quality and stability of the derivative evolution.

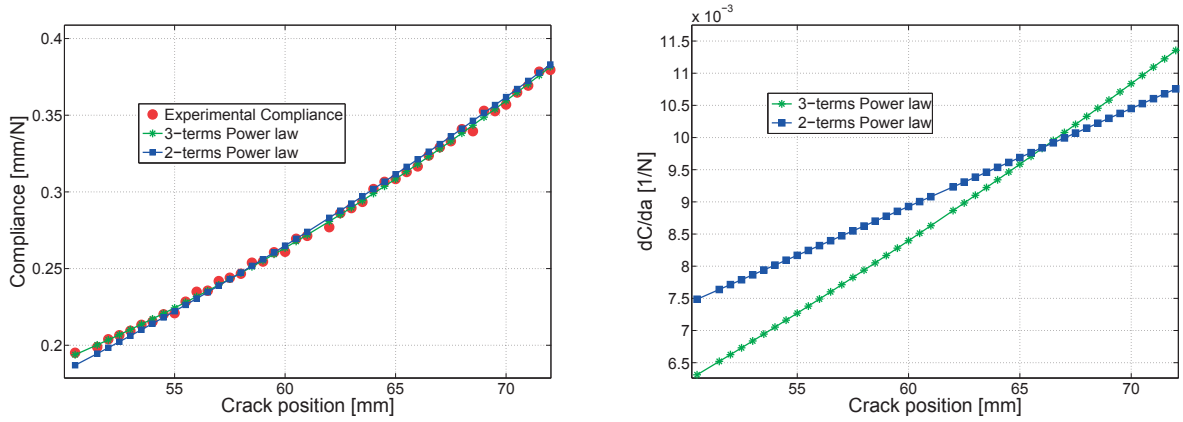

(a) (b)

Figure 3.10: (a) Compliance calibration method with 2 and 3-terms power law expression (b) Derivatives $\frac{dC}{da}$

3.3 Measurements by fiber Bragg grating sensors

Optical fibers provide the strain field around the crack tip and all over the bridging zone. They represent a key tool which allows to indirectly measure the bridging tractions in Mode I, Mode II and Mixed Mode delamination. The Multiplexed FBGs acquisition is performed by the Micron Optics® electronic device. An OLCR measurement is performed before the delamination test in order to detect the exact sensors position with respect the edge of the specimen. A good choice is to place the FBG sensors in a zone where the bridging is completely developed. In order to obtain a rough measurement of the maximum bridging length, a preliminary DCB test is performed to extract the ERR curve as a function of the crack increment. The beginning of the ERR plateau represents the complete development of bridging since the energy contribution is subsequently kept constant.

The optical fibers are composed by a $9\mu m$ core, made by silica doped with germanium for a better refractive index plus an external cladding ($125\mu m$ diameter, pure silica). In order to improve the mechanical properties, an external coating made of acrylate is added (Figure 3.11). The slight difference between the core and cladding refractive indexes, allows for the propagation of light along the fiber without any loss [82].

The Bragg sensor consists in a periodic variation of refractive index by exposing the core to ultraviolet light. By changing the exposure time of the core to a laser beam, different kind of Bragg sensors can be obtained. The effective core refractive index $n(z)$, along the axial z-axis of the fiber, is described as:

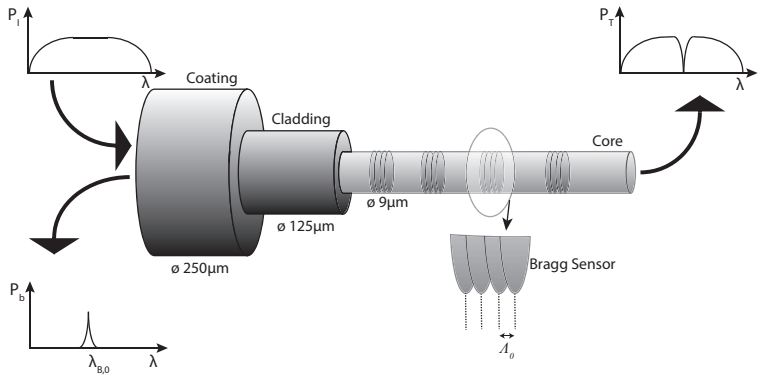

Figure 3.11: Optical Fiber

$$n(z) = n_0 + \Delta n_{ac}(z) cos\left(\frac{2\pi}{\Lambda} z + \theta(z)\right) + \Delta n_{dc}(z) = n_{eff} + \Delta n_{ac}(z) cos\left(\frac{2\pi}{\Lambda} z + \theta(z)\right) \quad (3.16)$$

where n_0 is the initial core refractive index, $\Delta n_{ac}(z)$ is the amplitude index change, $\Delta n_{dc}(z)$ the mean index change, $\theta(z)$ the grating chirp, η_{eff} the effective reflective index and Λ represents the grating period.

When a broadband light is coupled into the fiber, the Bragg wavelength $\lambda_{B,0}$ is reflected according to the formula:

$$\lambda_{B,0} = 2\eta_{eff} \cdot \Lambda_0 \quad (3.17)$$

By applying a strain to the optical fiber, Λ changes and, consequentially, λ_B. By monitoring the reflected wavelength, it is possible to obtain the applied strain. The relationship between multi-axial strains and λ_B is derived from the formula:

$$\frac{\lambda_B - \lambda_{B,0}}{\lambda_{B,0}} = \varepsilon_z + \frac{n_{eff}^2}{2}\left[p_{11}\varepsilon_x + p_{12}(\varepsilon_x + \varepsilon_y)\right] + (\alpha_f + \xi)\Delta T \quad (3.18)$$

where $p_{11} \approx 0.112$ and $p_{12} \approx 0.252$ are the Pocket's optic constants [93], $\alpha_f = 0.5 \cdot 10^{-7\circ} C^{-1}$ is the thermal expansion coefficient, $\xi = 8.916 \cdot 10^{-6\circ} C^{-1}$ the thermo-optic constant [94], ΔT the temperature variation and $\varepsilon_x, \varepsilon_y, \varepsilon_z$ are the mechanical strains, according to Figure 3.12.

In case $\varepsilon_x, \varepsilon_y$ are small comparing to ε_z:

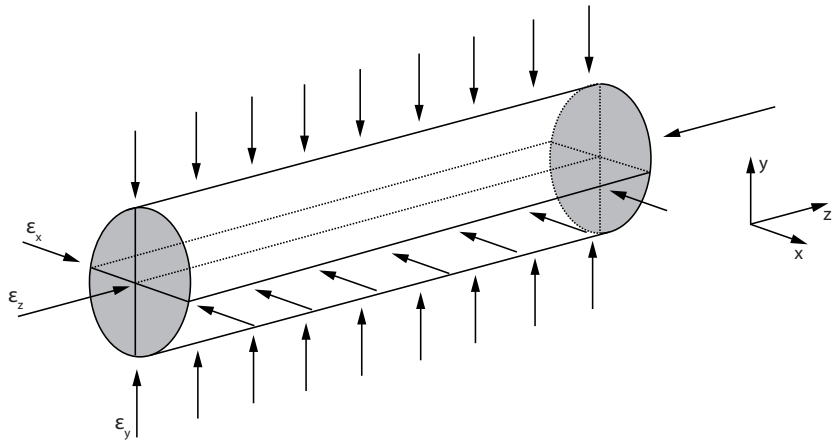

Figure 3.12: Optical fiber subjected to mechanical multi-axial strains

$$\varepsilon_x = \varepsilon_y = -\upsilon_f \varepsilon_z \tag{3.19}$$

Combining eq. 3.18 with eq. 3.19 we obtain:

$$p_e = \frac{n_{eff}^2}{2}\left[p_{12} - \upsilon_f(p_{11} + p_{12})\right] \tag{3.20}$$

The term p_e represents the Pockel's photo elastic coefficient taking into account the radial strains due to Poisson's coefficient. Thus, the following formula correlates the peak shift λ_B to the axial strain ε_z by assuming that the equation 3.19 is valid:

$$\frac{\lambda_B - \lambda_{B,0}}{\lambda_{B,0}} = (1 - p_e)\varepsilon_z + (\alpha_f + \xi)\Delta T \tag{3.21}$$

The value p_e can be experimentally obtained by loading the optical fiber with suspending weights and measuring the wavelength shift, since the applied axial strain ε_z is derived by the Young's modulus while the temperature is kept constant [95]. The experimental obtained value is $p_e = 0.2148$.

The reflected Bragg wavelength consists in a narrow spectrum if $\Lambda(z)$ is constant along the fiber grating. If uniform loads or temperature variations are applied, the peak λ_B shifts as shown in Figure 3.13(a). If the presence of axial loads causes a deformation of the fiber section, from circular to elliptical, or if a strain gradient is applied on the grating, the refractive index is not unique anymore and the fiber is called birefringent. The reflected peak is split, creating problems for the λ_B detection and making the measurement less accurate (Figure 3.13(b)).

In this work the acquisition system is performed by the Micron Optics® electronic device.

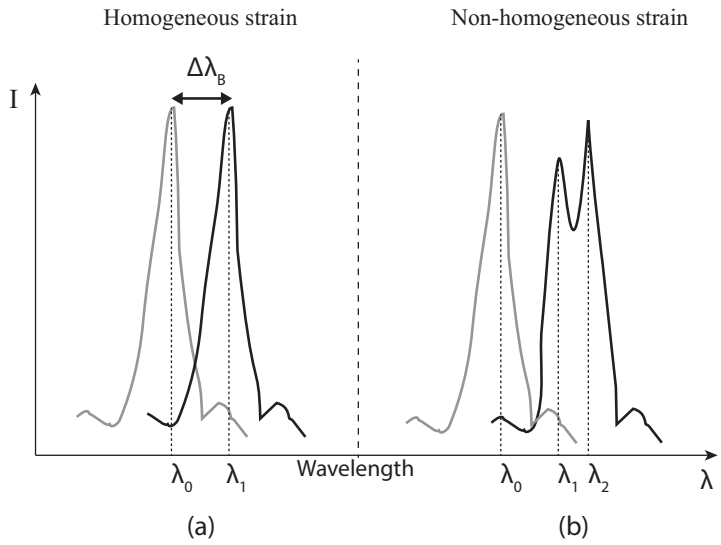

Figure 3.13: Reflected FBG spectrum from (a) homogeneous strain field and (b) non-homogeneous strain field

The implemented peak detection algorithm allows a sampling rate up to $1000Hz$. For our tests the sampling rate is decreased to $10Hz$ since the applied load is in quasi-static conditions.

3.3.1 Optical Low-Coherence Reflectometry

Optical Low-Coherence Reflectometry (OLCR) represents a measurement optical system in which the sensor consists in a very long Bragg grating, in contrast with the classic FBGs where the grating is kept as small as possible in order to get a high precision for local strain measurements. This method allows the measurement all over the Bragg sensor, without all the limitations of having a finite amount of discrete sensors. In this section the working principle and the advantages and disadvantages are analyzed.

The working principle of the Bragg grating is identical to the one described in section 3.3 with the advantage of a higher reflected spectrum intensity due to the longer grating. Since the grating spacing is constant, the reflected spectrum consists in a unique peak centered on the initial Bragg wavelength. The high length of the grating allows for the presence of non-uniform strains on and thus different grating spacing on the fiber. In this case the reflected spectrum will show multiple peaks, one for each wavelength activated by the local strains, with different intensities depending on the Bragg zone length involved. This is due to the fact that the intensity of the reflected spectrum depends on the grating length.

Unfortunately for the Bragg gratings, the reflected spectrum has no spatial information,

meaning that there is no correlation between a wavelength peak and the corresponding location along the fiber. For this reason the Optical Low-Coherence Reflectometry is needed, since it allows for associating the strains to the actual position on the fiber.

In case of perfect fiber without any loss, the evolution of forward and backward propagating field envelopes come from the following equations:

$$\frac{du(z,\delta)}{dz} = i\delta u + q(z)\nu \qquad (3.22) \qquad \frac{d\nu(z,\delta)}{dz} = -i\delta\nu + q*(z)u \qquad (3.23)$$

where $q(z)$ is the *complex coupling coefficient,* $\delta = \beta - \frac{\pi}{\Lambda_d}$ is the wave number detuning, $\beta = \frac{2\pi\eta_{eff}}{\lambda_d}$ is the propagation constant and $q*(z)$ is complex conjugate of $q(z)$. The corresponding amplitude $\mid q(z) \mid$ and phase $\Phi_q(z)$ are given by:

$$\mid q(z) \mid = \frac{\eta\pi\Delta\eta_{ac}(z)}{\lambda_d} \qquad (3.24)$$

$$\Phi_q(z) = \frac{\pi}{2} + \theta(z) - 2\eta k \int_0^z \Delta\eta_{dc}(z^{'})dz^{'} \qquad (3.25)$$

where η is the fraction of modal power in the fiber core, $k = {}^{2\pi}/_{\lambda_d}$ and λ_d is the design wavelength peak.

This method involves a broad-band light source and a Michelson interferometer. On one arm, the interrogator works with the FBG under test while on the other side a broadband mirror acts as reference. The source light is equally split in the two arms. The mirror can translate as a function of the sensors distance and the so obtained signal is analyzed in terms of amplitude $h(\tau)$ and phase . The spectral signal coming from the testing arm is calculated by applying the Fourier transform to $h(\tau)$ while $q(z)$ is obtained from the complex spectral response $r(\lambda)$, by using the layer-peeling reconstruction algorithm [96].

Figure 3.14 schematically shows the whole process. The laser and broad band light are activated and the optical switch alternates the two flows. After the circulator, the light is split in the reference and testing arm by a 3dB coupler. The reflected light coming from the two arms interferes in the coupler only if the optical length difference is smaller than the coherence length $L_c = 25\mu m$. By moving the mirror in the reference arm, the optical length changes until the two signals are synchronized. The displacement $\triangle z$, imposed to the mirror, is related to the distance $\triangle z^{'}$ at which the the optical fiber is interrogated, according to the formula:

$$\triangle z^{'} = \frac{\triangle z}{\eta_g} \qquad (3.26)$$

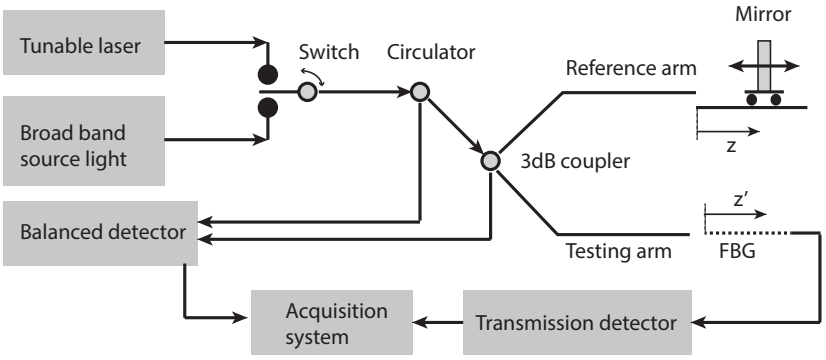

Figure 3.14: OLCR schema

where η_g is fiber refractive group index. By imposing a continuous displacement to the mirror, the optical fiber can be scanned all over the long Bragg grating.

The local Bragg wavelength $\lambda_B(z)$ is calculated by deriving the phase of the complex coupling coefficient:

$$\lambda_B(z) = 2\eta_{eff}\Lambda_d \left(1 + \frac{\Lambda_d}{2\pi}\frac{d\phi_q(z)}{dz}\right)^{-1}. \tag{3.27}$$

Inserting the equation 3.27 in 3.21, relation becomes:

$$\frac{\lambda_B(z) - \lambda_{B,0}(z)}{\lambda_{B,0}(z)} = (1 - p_e)\varepsilon_z + (\alpha_f + \xi)\Delta T. \tag{3.28}$$

The Bragg wavelength $\lambda_B(z)$ is finally associated to a specific position of the mirror and thus to the axial coordinate z on the fiber.

Figure 3.15 shows a typical signal from an OLCR test performed to obtain the exact position of ten Bragg gratings inscribed on a multiplexed optical fiber, with respect to its end. The end of the fiber is detected because it reflects a portion of the light spectrum and, therefore, provides an additional peak.

The OLCR can be used to measure the strains during quasi-static delamination tests but the biggest disadvantage is represented by the low speed of the acquisition. During the experiment, indeed, the testing machine must be stopped for some minutes to allow the OLCR to complete the measurement. Unfortunately, during this interval, the crack tends to propagate even if the applied displacement is stopped and the measurements are consequentially affected.

In this work, OLCR measurements are performed only to get the precise sensors position along the optical fiber, once it is embedded in the composite material. This measurement is performed before the delamination test.

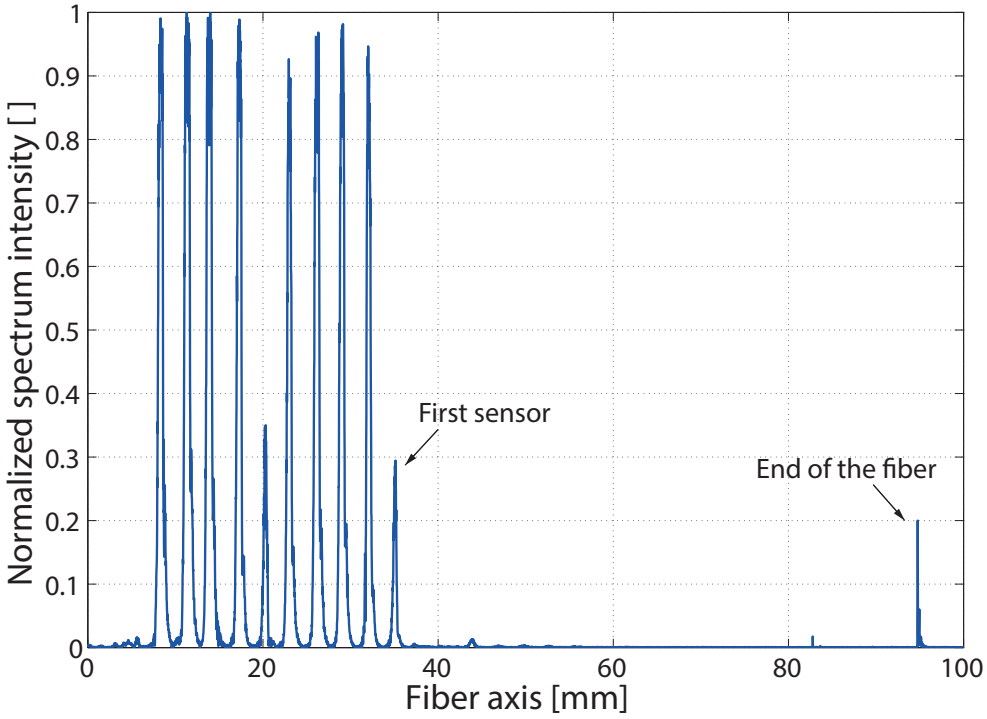

Figure 3.15: OLCR signal

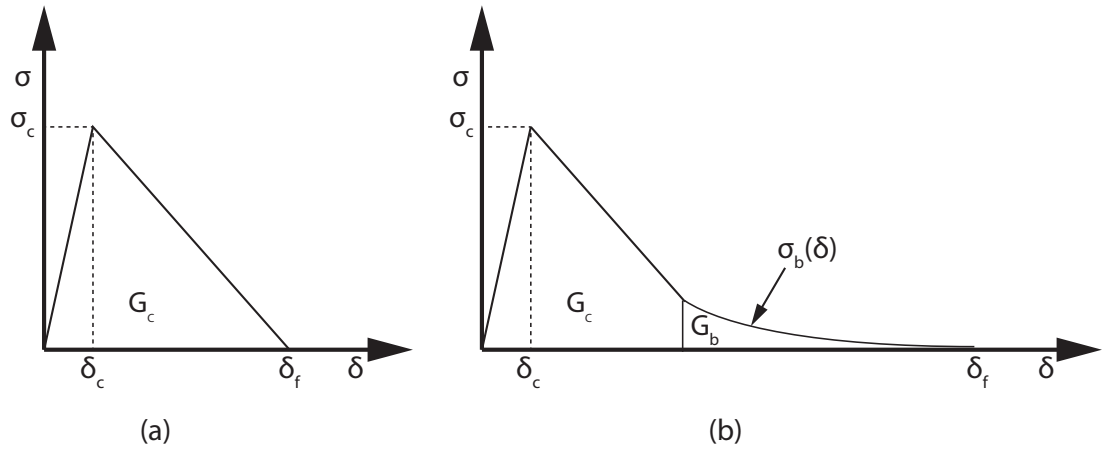

Figure 3.16: Cohesive law for fracture simulation (a) without bridging contribution (b) with bridging contribution

3.4 Cohesive Elements

The numerical simulation for a delamination process can be performed by using cohesive elements. In this section, a general overview about cohesive elements is provided. The state of the art and the main references are collected in Section 2.3.

The behavior of these elements, as shown in Figure 3.16(a), is characterized by a linear initial part in which the stress increases with the applied displacement and by a second region, representing the damage, in which the stress decreases down to zero. The relationship between stresses and the crack opening displacements is the so called *cohesive law*. This is characterized by the initial stiffness value K, the critical stress and corresponding displacement $\sigma_c(\delta_c)$ and the total area G_c which represents the critical energy release rate. This king of cohesive law is able to simulate fracture propagation if no toughening processes are involved.

When bridging occurs, the corresponding energy contribution must be taken into account. This is possible by adding a trailing part, where the corresponding area represents the bridging contribution G_b, as shown in Figure 3.16(b). In literature, this contribution mostly consists in a decreasing linear trailing part. This approach is found to be appropriate if a load-displacement curve fitting is required while it fails if a strain distribution, provided by the FBGs, has to be predicted. For this second case, a non- linear decreasing part is found to be more accurate. Bridging tractions are assumed to provide the maximum stress close to the crack tip, since the bridging fiber density is higher, and to decrease their contribution as it moves far, following a negative exponential trend. The bridging tractions σ_b can be written as a function of the

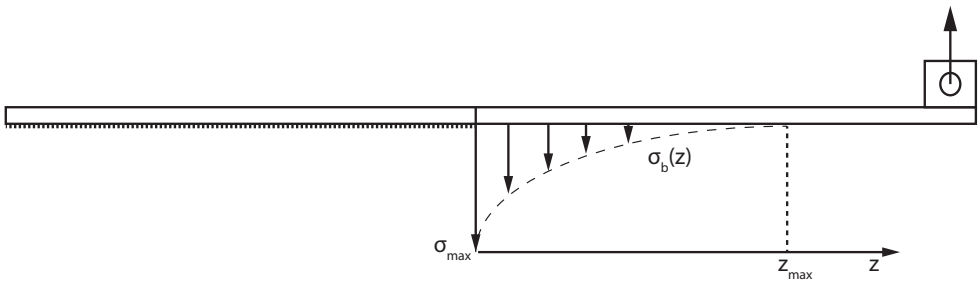

Figure 3.17: Bridging tractions

distance z from the crack tip and defined by the maximum stress σ_{max}, a coefficient γ and the maximum length z_{max} for which the tractions decrease to zero, as indicated by the following equation:

$$\sigma_b(z) = \sigma_{max} \cdot e^{-\gamma z} \cdot \left(1 - \frac{z}{z_{max}}\right) \tag{3.29}$$

Figure 3.17 shows a schematic of the bridging tractions, acting on the specimen crack plane. Since the relationship between the z coordinate and the crack opening displacement δ is obtained by the FE Model, the bridging tractions $\sigma_b(z)$ can be written as $\sigma_b(\delta)$, which represents the bridging trailing part for the cohesive law. The bridging energy G_b is obtained by integrating the tractions over δ as:

$$G_b = \int_0^{\delta_{max}} \sigma_b(\delta) d\delta. \tag{3.30}$$

The total energy release rate is obtained by adding the two contributions as follows:

$$G_{tot} = G_c + G_b. \tag{3.31}$$

In order to properly simulate the interlaminar fracture process, the thickness of the cohesive layer is set to zero, by collapsing the upper and the lower nodes.

Chapter 4

Experimental results

This chapter aims to show and discuss the experimental results obtained in Mode I, Mode II and Mixed Mode delamination tests. The main characteristics of each setting are pointed out. The delamination behavior in terms of load-displacement curve, crack advance and ERR is discussed. The strains provided by the embedded optical fibers, used to indirectly identify bridging tractions as described in Chapter 5, are also presented. The data from these tests represent the basis to characterize the bridging tractions over a wide range of mode mixities.

4.1 Mode I delamination test

Mode I delamination has been already well described and investigated over the years in terms of G_c and bridging tractions. ASTM standard [29] provides all the main information to properly run the DCB test, as already described in section 3.1.2 . Figure 4.1 shows the specimen used for the DCB test. The optical fiber is embedded in the upper part of the specimen.

The typical load-displacement curve is shown in Figure 4.2. After the rising linear part, the crack propagates when G reaches the critical value G_c for the Mode I delamination. The crack propagation is found to be very stable and smooth without any crack jump. This is mainly due to the large extent of bridging, developed during the crack propagation.

The corresponding crack length, obtained by the markers on both sides of the specimen, is shown in Figure 4.3(a). The difference between the two sides is almost negligible which means the crack front propagates evenly. An averaged value between the two signals can be considered as the actual crack length, as shown in Figure 4.3(b). Note that the value measured by the markers is actually underestimated due to the curved shape of the crack front, as discussed in section 3.1.3. The difference between the crack length measured by the external markers and the one in the middle of the specimen is $\sim 1.5mm$. A good compromise is to define the crack

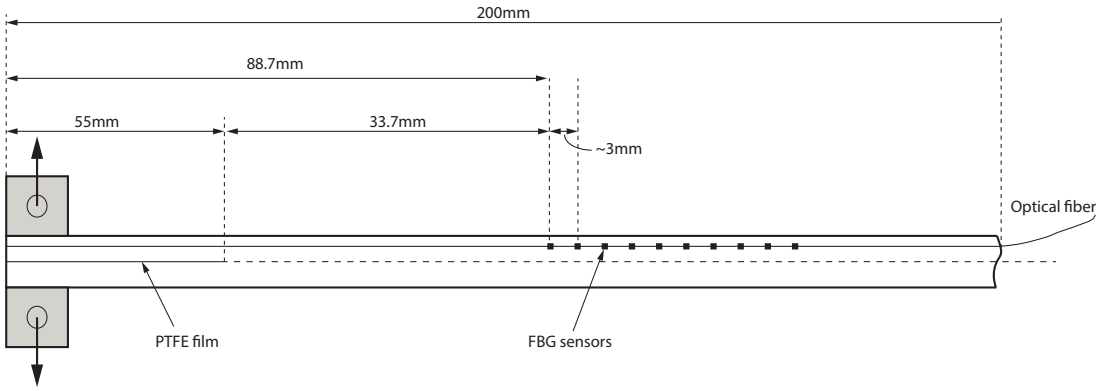

Figure 4.1: Mode I specimen with embedded optical fiber

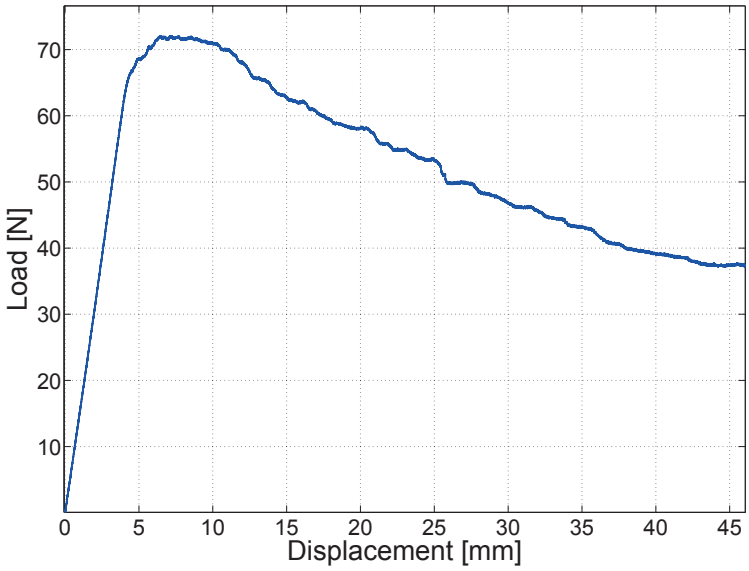

Figure 4.2: Mode I typical load-displacement curve obtained by a DCB test

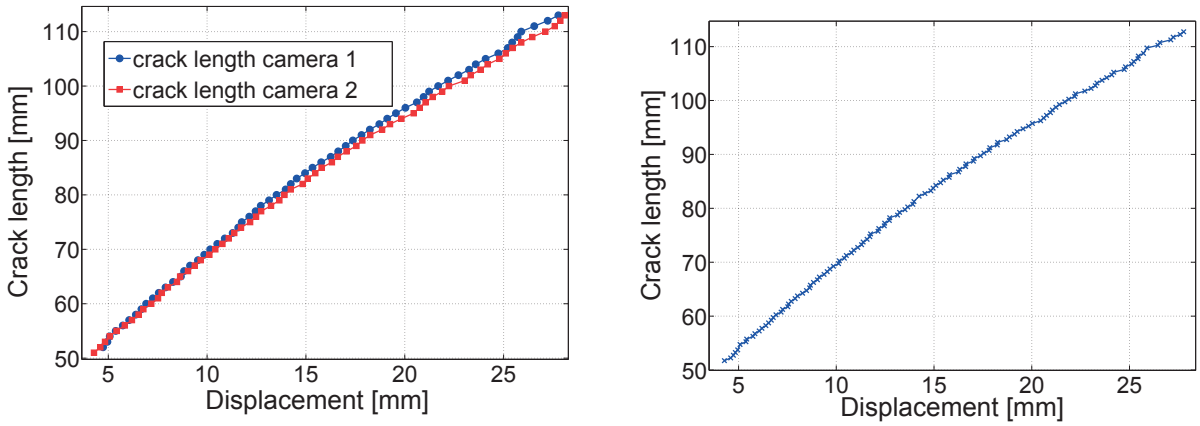

Figure 4.3: Mode I, crack length versus applied displacement obtained by markers; (a) measurement on both sides, (b) averaged value increased by $0.75mm$ to take into account the crack front curvature

length value as an average between the two values, which means to shift by $0.75mm$ the crack length curve. From this point on, all the averaged crack length curves shown in this work take into account this detail.

An accurate measurement of the crack length is extremely important in order to obtain a reliable fitting of the compliance C versus the crack length a. By fitting the curve with a power law, it is possible to analytically calculate the corresponding derivative $\frac{dC}{da}$ to obtain the ERR. Figure 4.4 shows the compliance versus crack length and the corresponding fitting curve. The power law equation, as discussed in section 3.2.1, provides an optimal fitting over the whole range of the experimental data.

The energy release rate, shown in Figure 4.5, is obtained by using the compliance calibration method. The critical energy at initiation is found to be equal to $G_c = 280\frac{J}{m^2}$. The rising part of the curve well points out that large scale bridging occurs on the crack faces, increasing the fracture energy up to a plateau around $G_{tot} = 720\frac{J}{m^2}$. The difference between G_{tot} and G_c represents the maximum bridging energy contribution $G_b = G_{tot} - G_c = 440\frac{J}{m^2}$. Once the bridging tractions are completely developed, the ERR curve becomes flat.

The bridging contribution G_b in Mode I delamination is found to be a relevant toughening process since it represents $\sim 60\%$ of the total energy G_{tot}. For this reason, bridging tractions must be taken into account to properly simulate the crack propagation in a finite element model.

The load-displacement curve and, mainly, the ERR well indicate an important influence of bridging. In order to obtain a visual evidence, a high resolution camera is used to show the

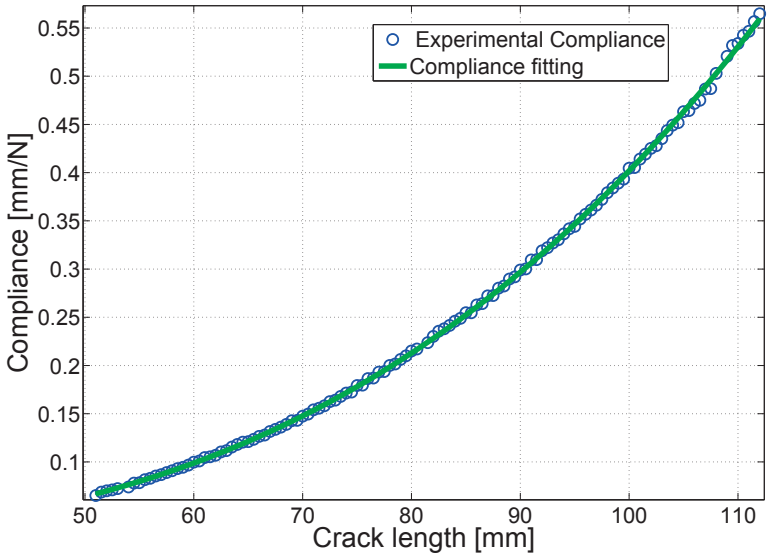

Figure 4.4: Mode I, compliance calibration method. Compliance versus crack length fitted by a power law equation

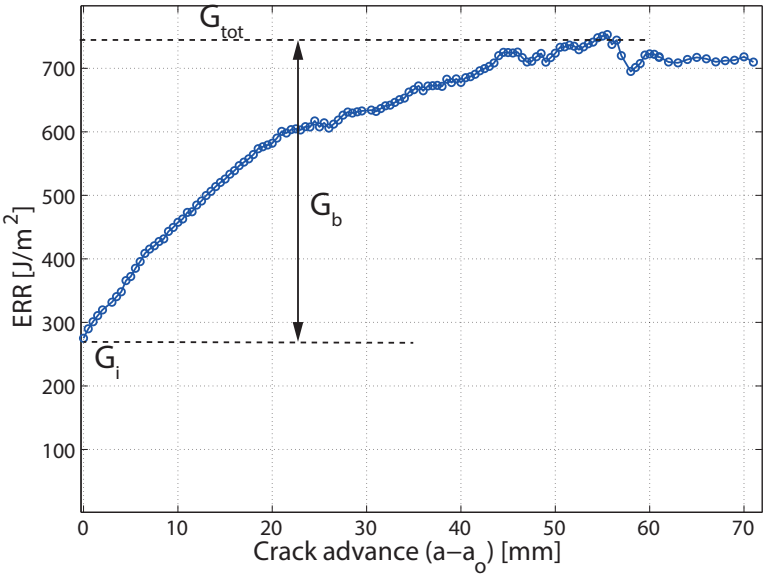

Figure 4.5: Mode I, ERR curve. Critical value and evolution with crack propagation

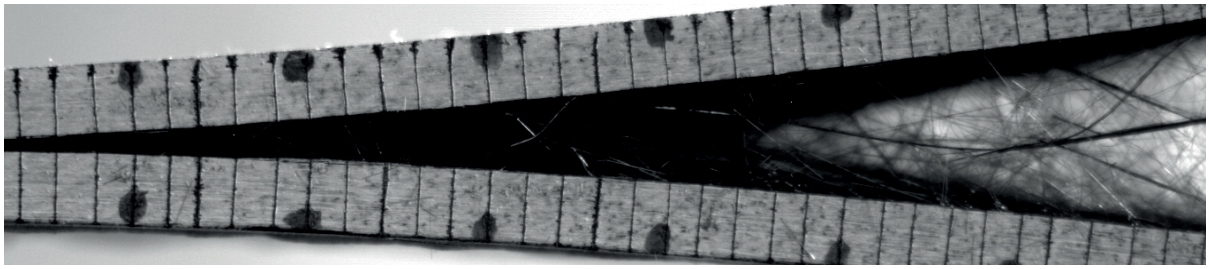

Figure 4.6: Mode I, bridging tractions in the middle of the crack with the toughening process completely developed

Sensor n°	1	2	3	4	5	6	7	8	9	10
Position [mm]	88.7	92.2	94.8	98.1	100.6	103.8	106.7	110.3	113.2	117.1
$\triangle$ [mm]		3.5	2.6	3.3	2.5	3.2	2.9	3.6	2.9	3.9

Table 4.1: Mode I: FBGs positions measured with respect to the edge of the specimen on the crack side

bridging bundles acting between the two crack faces once the toughening process is completely developed. Figure 4.6 shows a very dense and dark bridging area close to the crack tip which indicates a high level of tractions. If we move far from the crack, the amount of bridging fibers decreases. The approximation chosen to represent the bridging tractions, as discussed in section 3.4, equation 3.29, which implicates a negative exponential, comes from this assumption. Since the delamination process is symmetrical, the direction of the bridging tractions is considered to be normal with respect to the crack plane.

In a delamination process with large scale bridging, the tractions affect not only the behavior of crack propagation and the ultimate load but also the curvature of the specimen and, therefore, the strains along the bridging area. Multiplexed optical fibers represent an extremely important tool able to monitor the strains inside the specimen. As explained in section 3.1, the optical fiber is placed between the layer 19 and 20. The position of the ten sensors, with respect to the edge of the specimen on the crack side, is measured by using the OLCR (see section 3.3.1), as shown in table 4.1. Even if the optical fiber manufacturer indicates a $3mm$ spacing between the Bragg sensors, the measurement obtained by the OLCR revealed that this value is accurate with a scatter of $\pm 0.87mm$.

Figure 4.7 shows the strains measured by the ten FBGs as a function of the applied displacement. The small dip at the end of the steep part of each curve is due to the stress field perturbation generated by the crack tip. Consequently, this additional information can be used as crack tip indicator. Figure 4.8 shows a comparison between the crack length visually measured by the markers on the side of the specimen and the one indicated by the embedded FBGs.

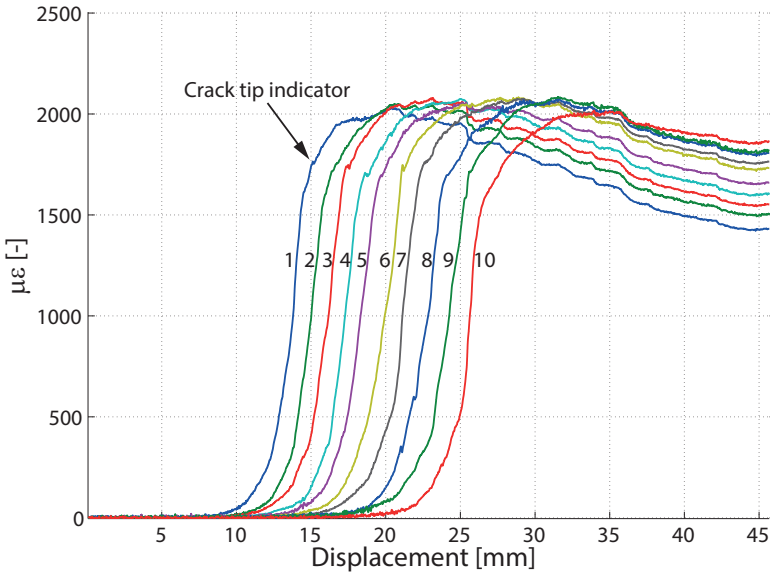

Figure 4.7: Mode I, strains measured by Multiplexed FBGs as a function of the applied displacement

It is found out that the crack length measured by the FBGs is $\sim 1.5mm$ higher, which perfectly matches with crack front curvature analyzed in section 3.1.3. This comparison is a proof of the high measurement accuracy provided by the FBGs.

In order to check the self-similarity of crack growth, the strain values are plotted in Figure 4.9 as a function of the crack length and then shifted to common crack tip position. The fact that the strains in the bridging zone perfectly coincide, indicates that a self-similar crack propagation occurs.

The strain values, measured when the crack tip coincides with the 10^{th} Bragg sensor, are plotted as a function of the FBGs position in Figure 4.10. This method allows to know the strain profile over the crack plane and along the bridging area. This curve will be used in the iterative optimization process (see Chapter 5), combined with the corresponding finite element model, as objective function, in order to indirectly obtain the bridging tractions.

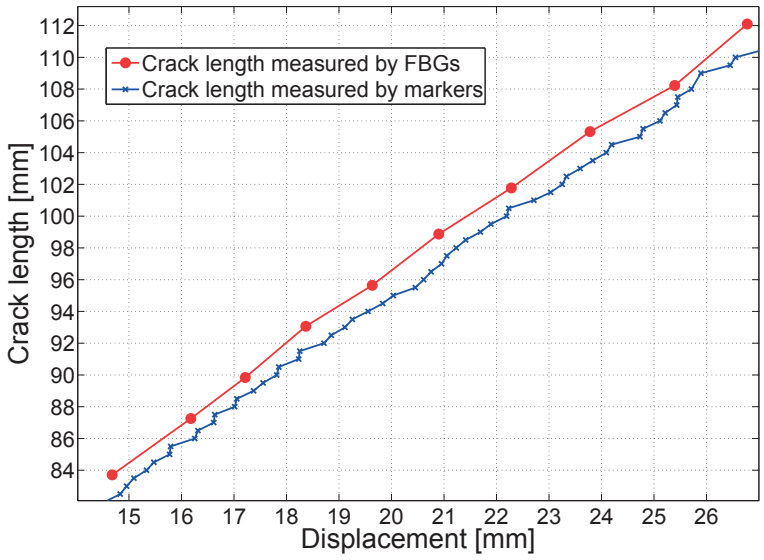

Figure 4.8: Mode I, crack length versus applied displacement measured by side markers and FBGs

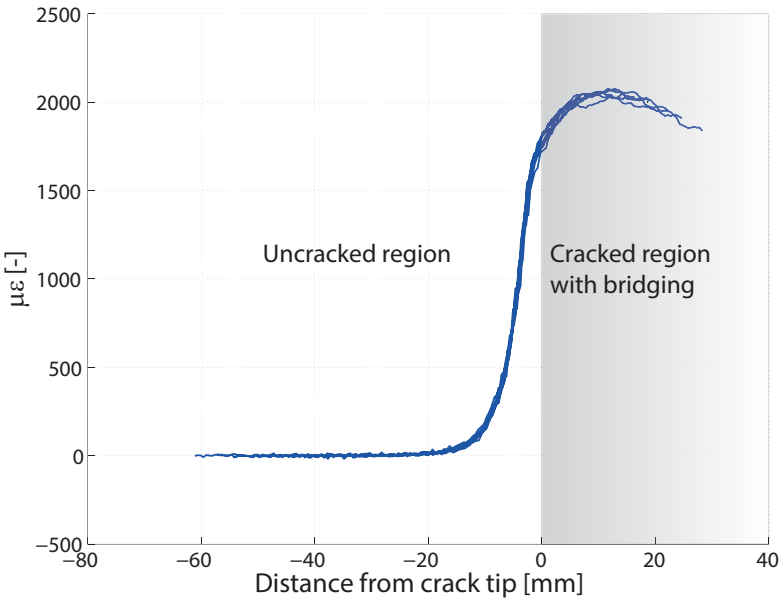

Figure 4.9: Mode I, shifted FBGs strains to common crack tip position

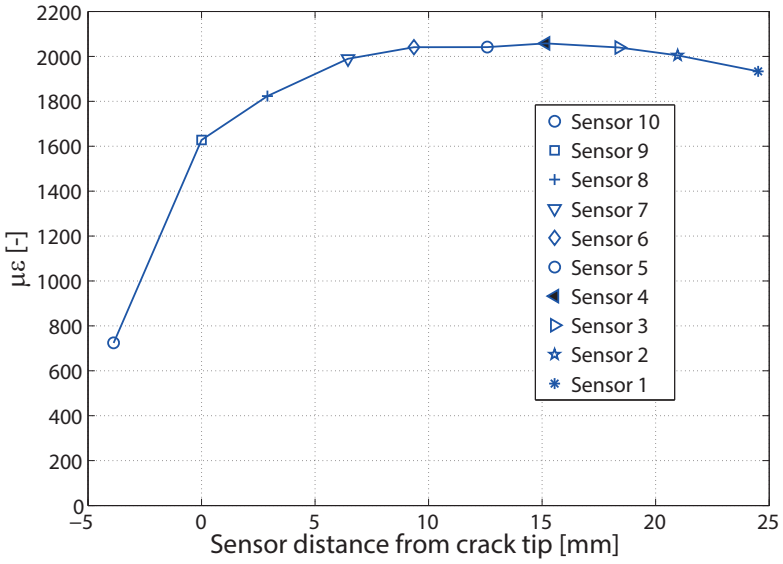

Figure 4.10: Mode I, strain profile measured by the FBGs above the crack plane, along the bridging zone

4.2 Mixed Mode Delamination tests

In this section, the experimental results obtained from 20%, 30%, 40% and 60% Mixed Mode delamination tests are shown. The tests are performed by using the MMB setting according to the ASTM standards [43]. The stability of the crack propagation and the repeatability of the results represent an important issue in Mixed Mode delamination, since the behavior after the crack onset is very sensitive to the material properties and the applied mode mixity. In order to compare results in terms of load-displacement curves, crack propagation and ERR over different batches of specimens, the fabrication process must be highly reproducible. Since scatter is still present, mostly in 40% and 60%, a large number of specimens are tested in the same test conditions in order to average the experimental data. For this reason, in the following subsections, average curves are shown with the corresponding standard deviations.

According to Figure 4.11, the optical fiber is placed in the upper part of the specimen, subjected to a higher curvature with respect to the lower one, to increase the sensitivity of the measurement. The applied mode mixity changes with the length of the C-arm, as discussed in section 3.1.2. The half-span $L = 90mm$ has been increased with respect to the one recommended in the ASTM standards ($L = 50mm$) in order to extend the crack propagation and to allow a complete development of bridging. Any geometrical non-linearities are checked by looking at

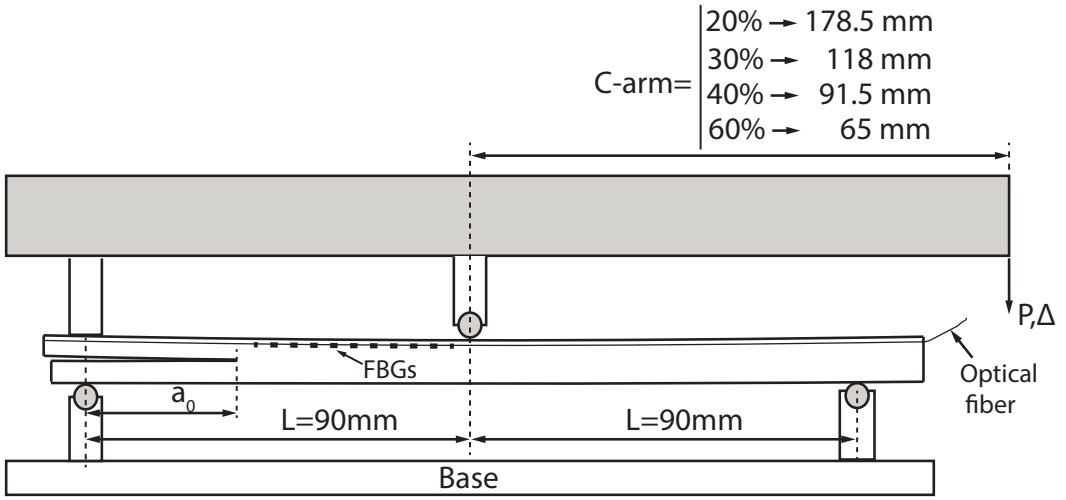

Figure 4.11: Mixed Mode Bending setting, specimen and embedded optical fiber

the unloading curve at the end of the test, as pointed out in the following results.

4.2.1 Mixed Mode test: 20%

Figure 4.12 shows the load-displacement curve obtained by a Mixed Mode delamination test performed at $\mu = \frac{G_{II}}{G_{tot}} = 20\%$. The curve shows the average load calculated over six specimens and the corresponding standard deviation. The test is found to be very stable in terms of crack propagation, without any jump during the whole process. The standard deviation in the first linear part is almost negligible, meaning that thickness, initial crack length and material properties are very similar between each specimen. In the crack propagation region, the standard deviation increases due to the fact that the crack interface characteristics play a major role.

The crack length versus applied displacement is shown in Figure 4.13. The standard deviation is similar to the one obtained in the load-displacement curve, pointing out that the scatter over the two curves is not mutual independent.

The energy release rate is obtained by compliance calibration method. Figure 4.14 shows the initiation value and the trend along the crack propagation. The average energy at initiation is $G_c = 335\frac{J}{m^2}$ while it increases as the crack advances up to $G_{tot} = 515\frac{J}{m^2}$, indicating the development of a bridging toughening process. The scatter over the G_c is relatively small while, as already checked, the crack propagation region is more affected to noise. The standard deviation of the ERR is computed by combining the one measured on the load and the one measured on the crack length, taking into account that the two factors are not mutually independent. Unfortunately the set-up does not allow the energy to achieve a steady state, due to the short

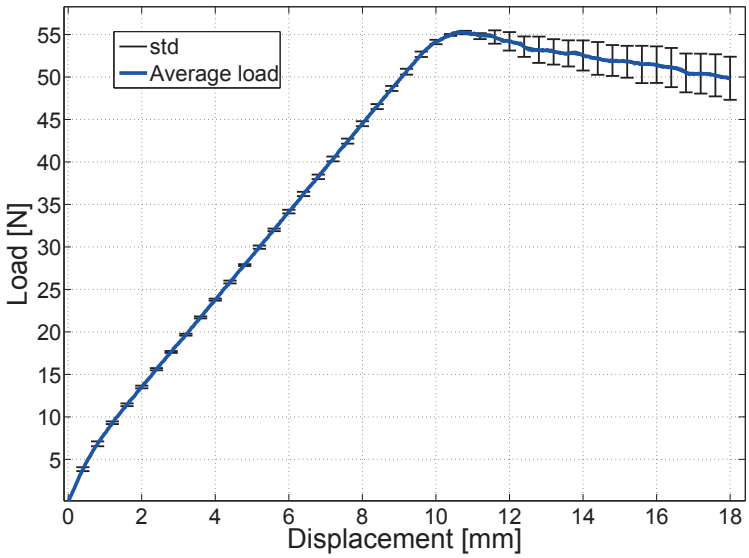

Figure 4.12: Mixed Mode $\mu = 20\%$, average load-displacement curve and standard deviation

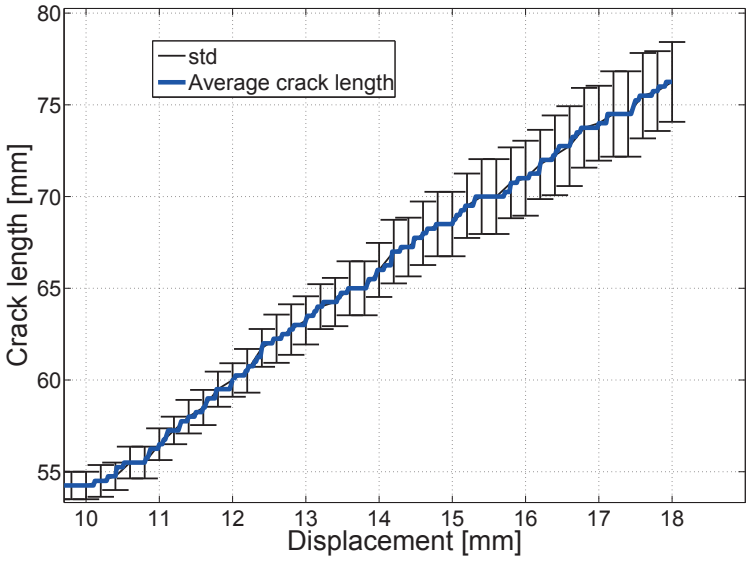

Figure 4.13: Mixed Mode $\mu = 20\%$, crack length measured by markers versus applied displacement

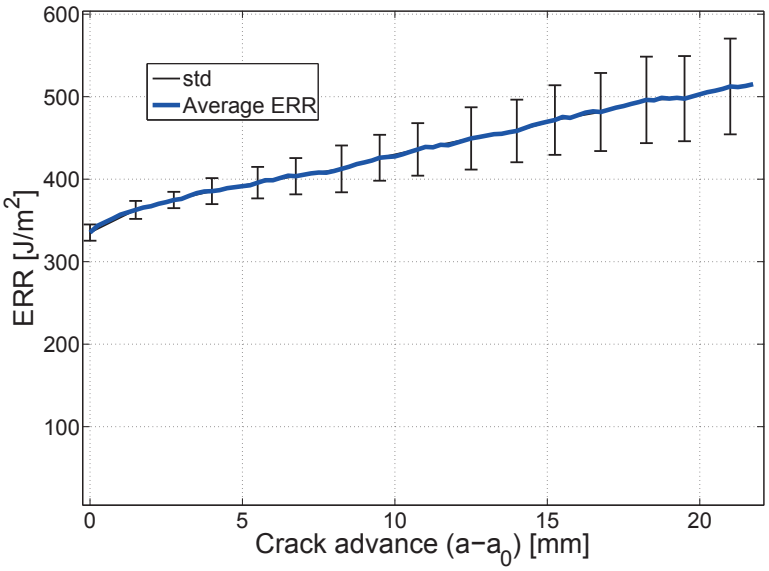

Figure 4.14: Mixed Mode $\mu = 20\%$, ERR. Critical value at crack initiation and evolution with the crack propagation

crack propagation range. For this reason, we cannot calculate the actual bridging contribution as the difference $G_b = G_{tot} - G_c$, but it can be assumed that $G_b \geq G_{tot} - G_c = 180\frac{J}{m^2}$.

The presence of a large scale bridging is also shown in Figure 4.15, captured at the end of the test when the crack advance is at $\triangle a = 20mm$, just before the central pin of the MMB setting. As it happens for Mode I delamination, an important amount of bridging fibers is visible in the cracked area. Even if a large scale bridging still occurs, the maximum range of influence is clearly reduced with respect to the Mode I case.

Another relevant difference between Mode I and Mixed Mode is represented by the bridging fibers direction. Unlike the bridging developed in Mode I, the tractions in Mixed Mode are clearly set according to an angle θ due to the simultaneous presence of sliding and opening.

The multiplexed optical fiber is embedded into the specimen with the Bragg sensors placed over the bridging zone. Table 4.2 shows the position of each sensor, measured by OLCR, with respect to the edge of the specimen.

Figure 4.16 shows the strains measured by the FBG sensors as a function of the applied displacement. Unlike the strain curves obtained in Mode I delamination test, the dip shape at the end of the rising part is less evident. Taking as crack tip reference the end of the rising part as indicated, the comparison between the crack length obtained by markers and FBGs is shown in Figure 4.17. The difference between the two curves, as obtained in the Mode I delamination

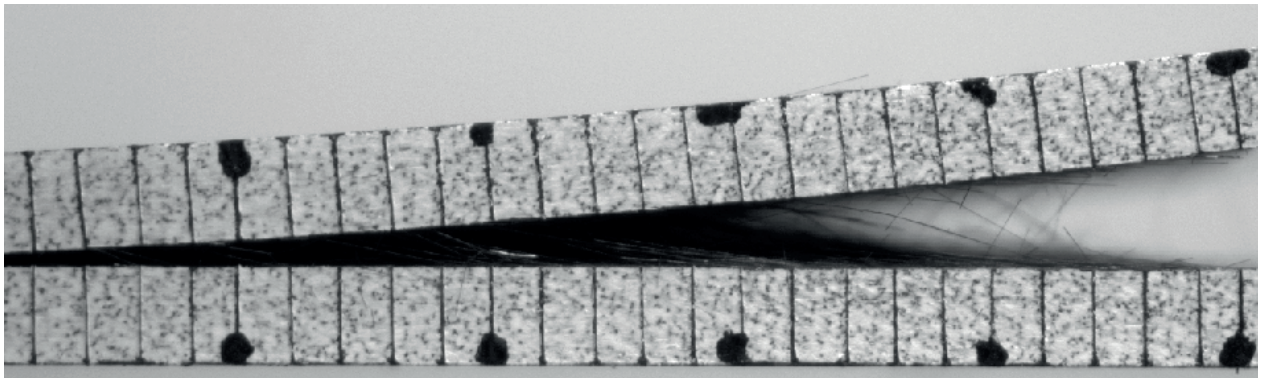

Figure 4.15: Mixed Mode $\mu = 20\%$, bridging tractions in the middle of the crack at $\triangle a = 20mm$

Sensor n°	1	2	3	4	5	6	7	8	9	10
Position [mm]	59.7	62.8	65.5	68.3	71.6	74.4	77.4	80.7	83.5	86.5
$\triangle$ [mm]		3	2.8	2.8	3.3	2.8	3	3.3	2.8	3

Table 4.2: Mixed Mode $\mu = 20\%$, FBGs positions measured with respect to the edge of the specimen

test, is $\sim 1.5mm$, which indicates the same curved crack front shape.

As already discussed, the ERR does not show any steady state, which indicates that the bridging tractions are not fully developed. For this reason, as shown in Figure 4.18, the FBGs strains measured in the bridging zone are not superimposed, indicating that self-similar crack propagation is not achieved. This behavior must be taken into account if the strains coming from FBGs are used to indirectly measure the bridging tractions and, therefore, to implement the numerical model.

The higher length of the half-span used in the MMB setting imposes to check if the linearity of the system is kept. A reliable way to verify this assumption is to look at the unloading curve starting from the maximum displacement. Figure 4.19 shows a typical loading and unloading curve. The linear fitting of the unloading part, with the $R^2 = 0.9987$, shows that the geometrical non-linearity is almost negligible. The initial drop of the load when the unloading part begins is due to the bridging fibers that switch from tensile to compression stresses. At the end of the unloading curve, the bridging fibers in buckling cause the final non-linear part.

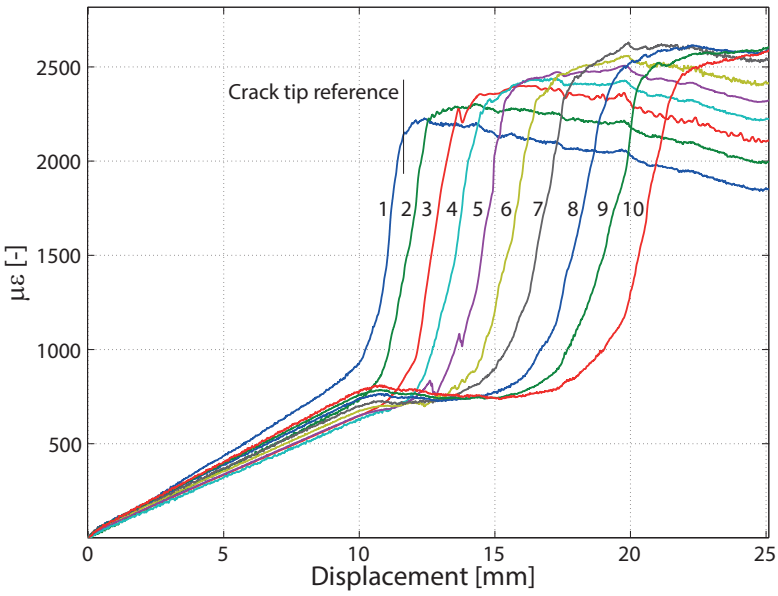

Figure 4.16: Mixed Mode $\mu = 20\%$, strains measured by Multiplexed FBGs as a function of the applied displacement

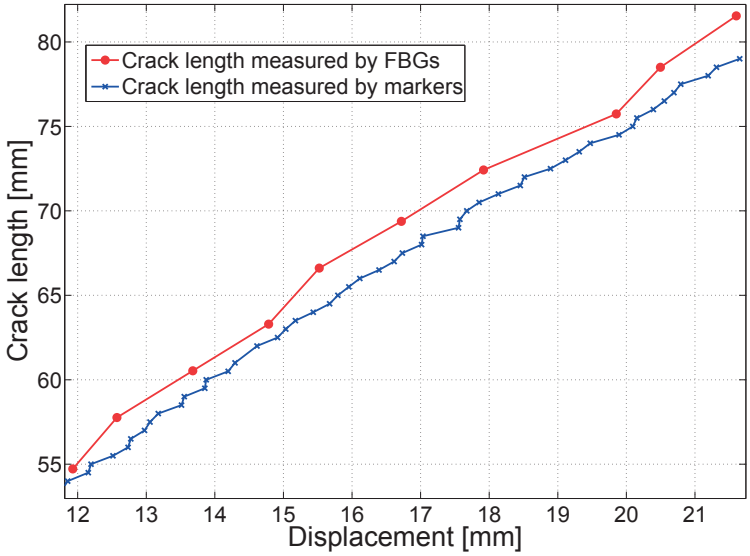

Figure 4.17: Mixed Mode $\mu = 20\%$, crack length measured by side markers and FBGs, versus applied displacement

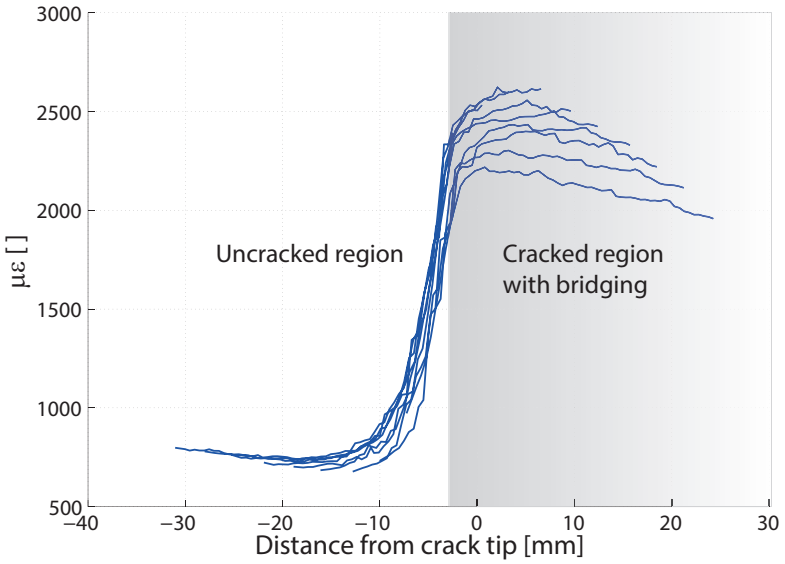

Figure 4.18: Mixed Mode $\mu = 20\%$, shifted FBGs strains to common crack tip position

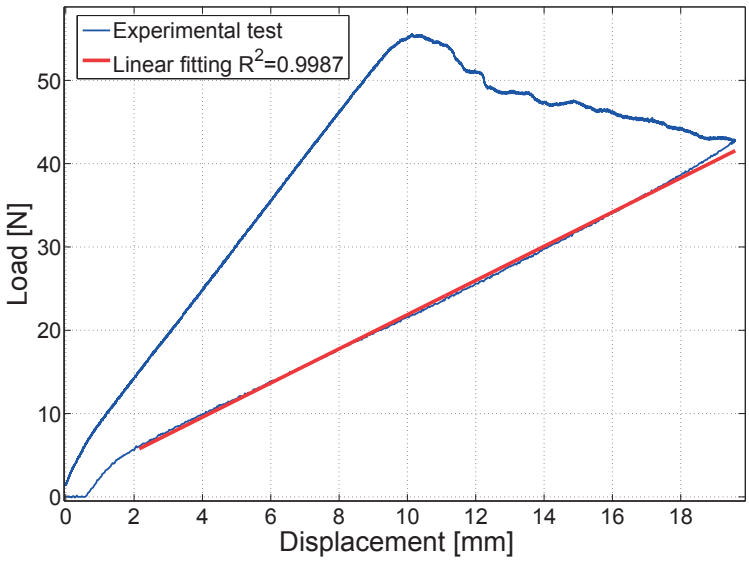

Figure 4.19: Mixed Mode $\mu = 20\%$, unloading curve to check the linearity of the system

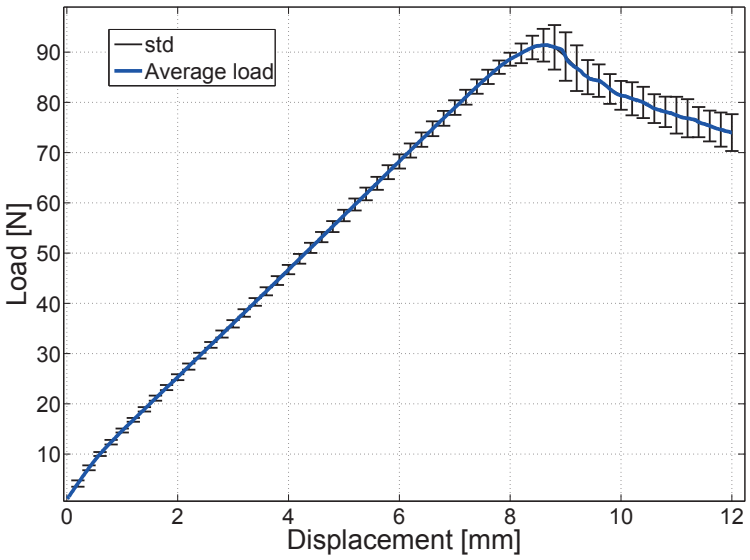

Figure 4.20: Mixed Mode $\mu = 30\%$, average load-displacement curve and standard deviation

4.2.2 Mixed Mode test: 30%

Figure 4.20 shows the load displacement curve at $\mu = 30\%$. Average load and standard deviation are computed over eight specimens, tested in the same conditions. Comparing with the curve obtained with $\mu = 20\%$, the load after crack initiation drops more quickly but no instabilities are present.

The crack length versus displacement is shown in Figure 4.21. As in the previous case, the test is not affected by any crack jump, resulting in stable and smooth crack propagation.

Figure 4.22 shows the ERR as a function of the crack advance. With $\mu = 30\%$ the contribution of bridging is clearly reduced with respect to Mode I and Mixed Mode at $\mu = 20\%$. After a short initial rising part, the steady state is reached after a few millimeters of crack advance. The initiation is found to be $G_c = 400\frac{J}{m^2}$, the plateau $G_{tot} \backsimeq 470\frac{J}{m^2}$ and the contribution of bridging in terms of energy is $G_b = G_{tot} - G_c \backsimeq 70\frac{J}{m^2}$. The standard deviation over the initiation value is within the 3% while in the crack propagation region is within the 10%. The small amount of bridging is proved by Figure 4.23, which shows the fibres in the middle of the delamination plane. Fiber bundles are still present but the density is lower if compared with Mode I and 20% Mixed Mode tests.

Table 4.2 indicates the position of each sensor, measured by OLCR, with respect to the edge of the specimen and the strains, measured by FBGs, are shown in Figure 4.24. Taking the end

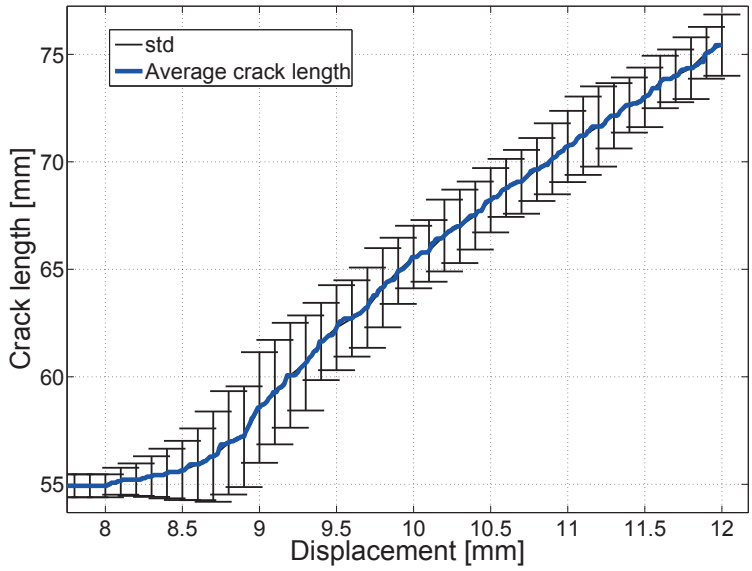

Figure 4.21: Mixed Mode $\mu = 30\%$, crack length measured by markers versus applied displacement

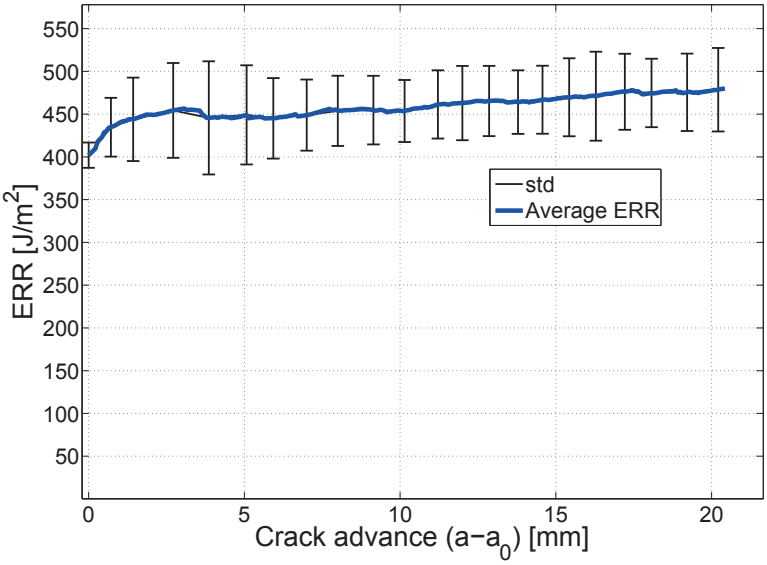

Figure 4.22: Mixed Mode $\mu = 30\%$, ERR. Critical value at crack initiation and evolution with crack propagation

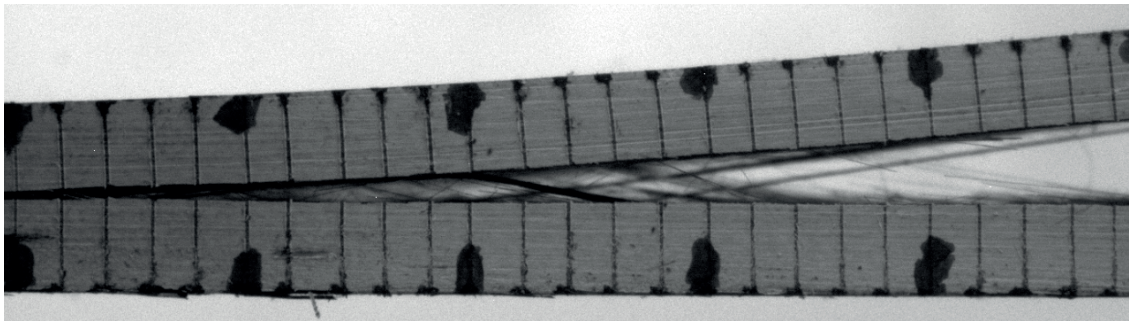

Figure 4.23: Mixed Mode $\mu = 30\%$, bridging tractions in the middle of the crack at $\triangle a = 20mm$

Sensor n°	1	2	3	4	5	6	7	8	9	10
Position [mm]	58.4	61.8	65.4	69.2	72.6	75.7	79.2	82.7	86.3	90.2
$\triangle$ [mm]		3.4	3.6	3.8	3.4	3.1	3.5	3.5	3.5	3.9

Table 4.3: Mixed Mode $\mu = 30\%$, FBGs positions measured with respect to the edge of the specimen

of the rising part as crack tip reference, as already done in the previous case at $\mu = 20\%$, the crack length compared to the one obtained by the markers is shown in Figure 4.25. Also in this test the optical fiber is found to be a reliable tool to measure the crack length since the difference between the two curves still represents the curvature of the crack front.

Figure 4.26 shows the strains measured by the ten FBGs, shifted in order to obtain coinciding crack tip. As the ERR indicates that the delamination process reached a steady state, also the strains in the bridging zone are superimposed which proves that the assumption of self-similar crack propagation is verified.

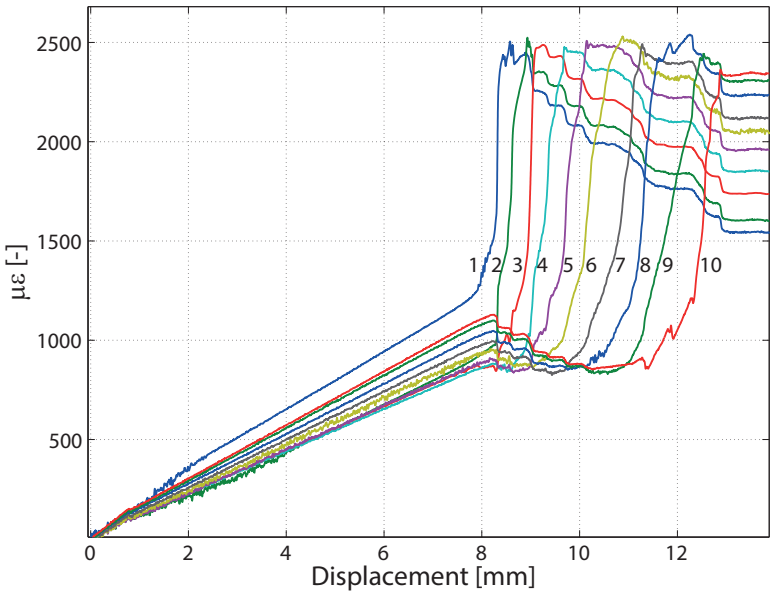

Figure 4.24: Mixed Mode $\mu = 30\%$, strains measured by Multiplexed FBGs as a function of the applied displacement

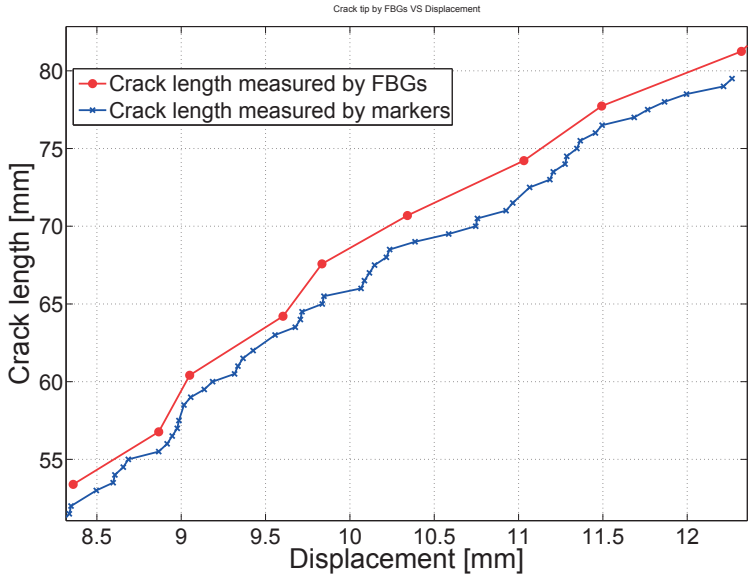

Figure 4.25: Mixed Mode $\mu = 30\%$, crack length versus applied displacement measured by side markers and FBGs

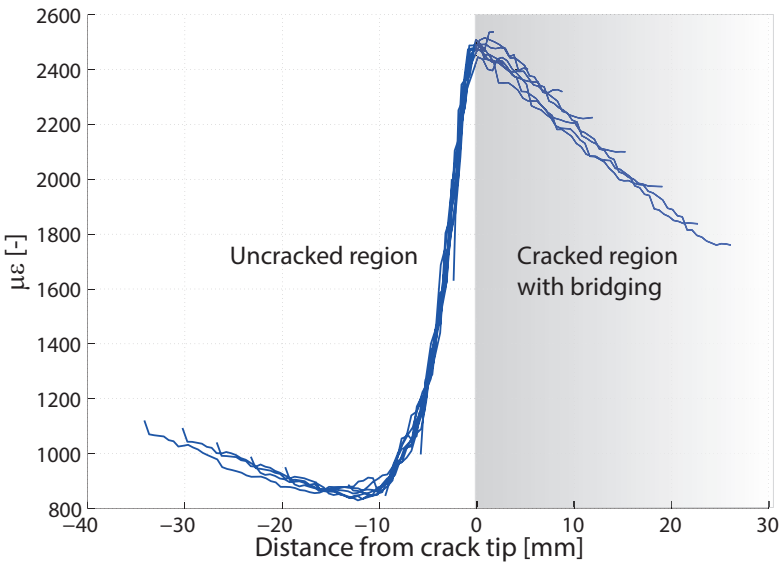

Figure 4.26: Mixed Mode $\mu = 30\%$, shifted FBGs strains to common crack tip position

4.2.3 Mixed Mode test: 40%

The Mixed Mode test performed at 40% is found to be more problematic than the previous ones in terms of stability at crack initiation and smoothness of the post-peak region. The higher Mode II percentage and a lower toughening contribution in crack propagation, make the threshold between stability and instability closer. Small differences of material properties between the tested specimens generate large scatter. Figure 4.27 shows the average load-displacement curve computed over five specimens. The amount of tested specimen is higher but the ones in which the crack jumped after initiation are not considered, since it is not possible to apply the compliance calibration method and, therefore, to compute the ERR.

The crack length shown in Figure 4.28 represents the average of the stable tests. The standard deviation is higher if compared to the one obtained at $\mu = 20\%$ and 30%, indicating that the crack propagation can be easier affected by variations of the material properties along its path.

The ERR is shown in Figure 4.29. The critical energy at initiation is $G_c = 460\frac{J}{m^2}$, the $G_{tot} = 520\frac{J}{m^2}$ and, therefore, $G_b = G_{tot} - G_c \backsimeq 60\frac{J}{m^2}$. The fact that for $\mu = 40\%$ only tests with a stable crack propagation are taken into account, makes these results less representative of the applied mode mixity. Indeed the crack propagation stability improves as bridging contribution increases. This means that the unstable specimens did not develop enough bridging tractions.

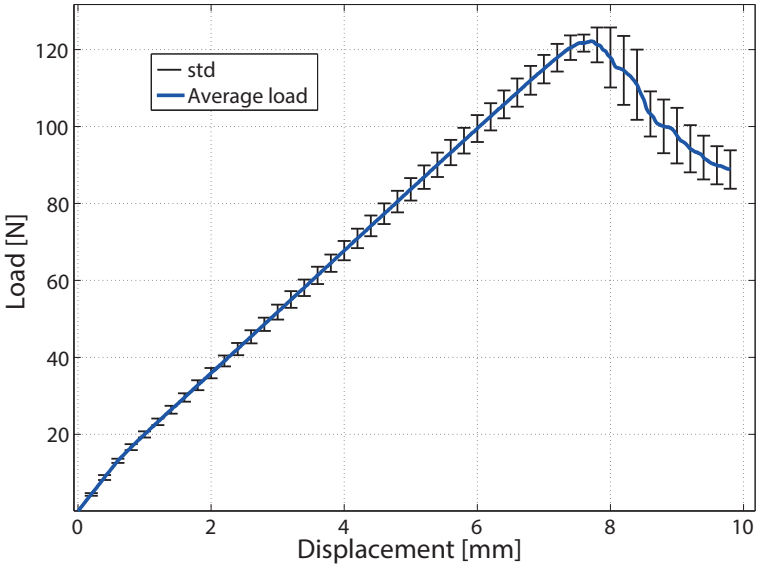

Figure 4.27: Mixed Mode $\mu = 40\%$, average load-displacement curve and standard deviation

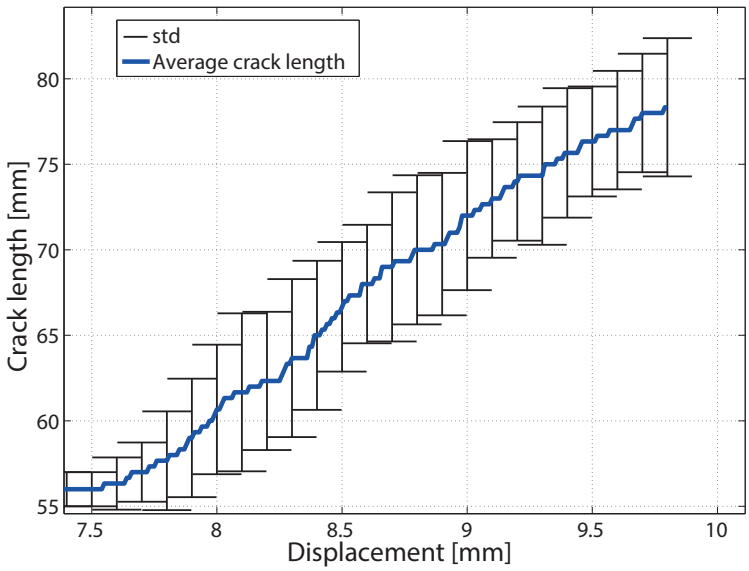

Figure 4.28: Mixed Mode $\mu = 40\%$, crack length measured by markers versus applied displacement

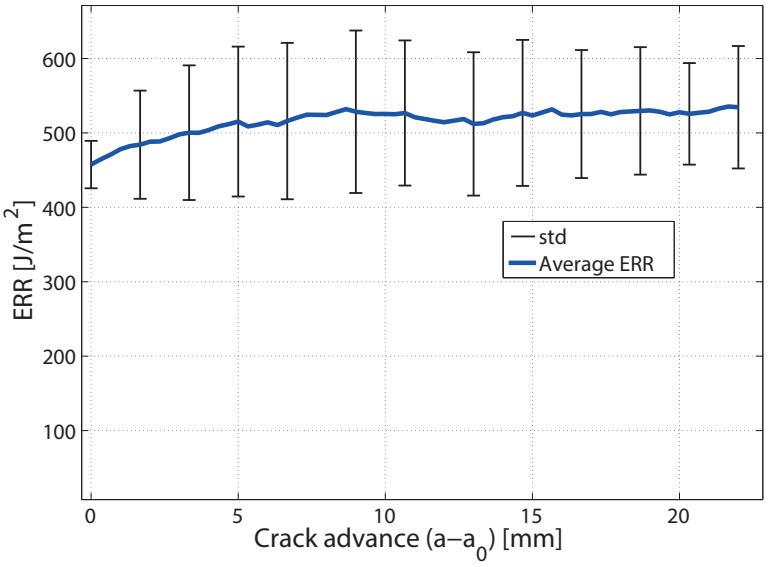

Figure 4.29: Mixed Mode $\mu = 40\%$, ERR. Critical value at crack initiation and evolution with crack propagation

For this reason, it can be assumed that the curves obtained at $\mu = 40\%$ are representative of specimens with higher bridging contribution. This may explain why the bridging contribution G_b is similar to the one obtained at $\mu = 30\%$.

Figure 4.30 shows the bridging bundles between the crack faces. The image proves that bridging occurs in 40% Mixed Mode test but the contribution is small compared to lower mode mixities.

Figure 4.31 shows the strains measured by the ten FBGs, positioned according to the Table 4.4, with respect to the applied displacement. By looking at the FBGs strains, it is clear that, for this particular test, a crack jump at initiation is present. After this instability, a smooth crack propagation occurs.

Figure 4.32 shows the crack length measured by FBGs and markers. Due to an initial crack jump, the first 3 sensors do not allow to obtain a reliable crack length. The remaining sensors, instead, provide an accurate measurement of the crack propagation, with the usual difference due to the curved crack front.

Since the contribution of bridging is small all along the crack propagation, a self-similar crack propagation can be assumed. Figure 4.33 shows the FBGs strains shifted in order to obtain a coinciding crack tip. The strains in the cracked region are almost superimposed which indicates a self-similar crack propagation.

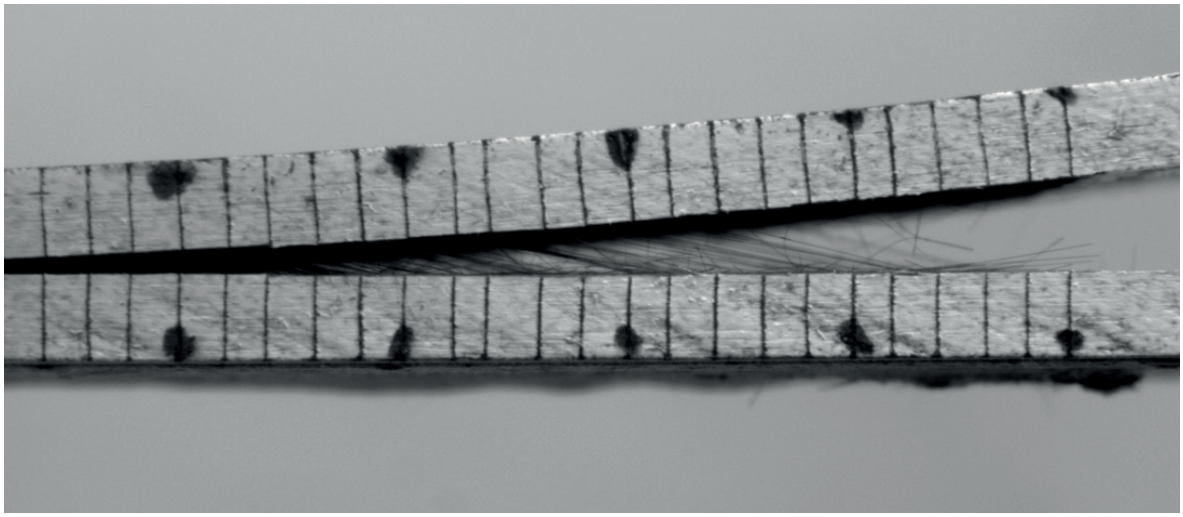

Figure 4.30: Mixed Mode $\mu = 40\%$, bridging tractions in the middle of the crack at $\triangle a = 20mm$

Sensor n°	1	2	3	4	5	6	7	8	9	10
Position [mm]	55.1	58.1	61.3	64.5	67.5	70.3	73	76.3	79	82
$\triangle$ [mm]		3	3.2	3.2	3	2.8	2.8	3.2	2.8	3

Table 4.4: Mixed Mode $\mu = 40\%$, FBGs positions measured with respect to the edge of the specimen

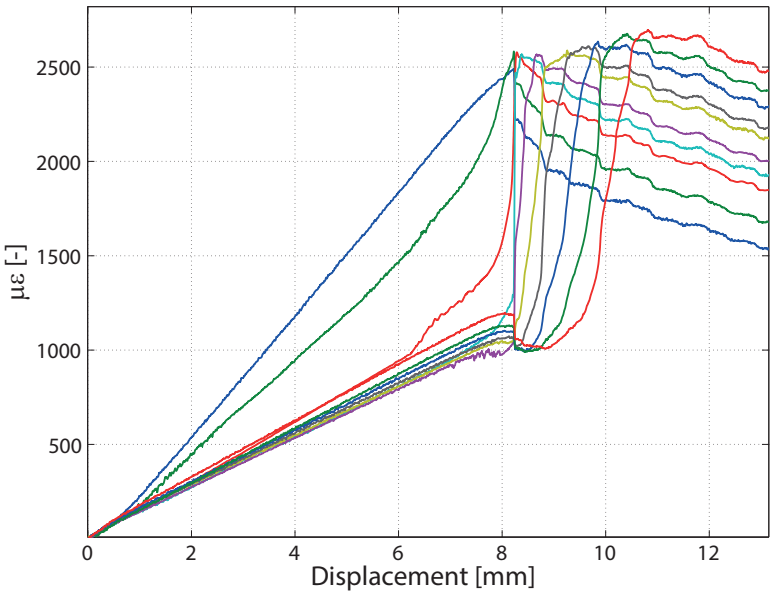

Figure 4.31: Mixed Mode $\mu = 40\%$, strains measured by Multiplexed FBGs as a function of the applied displacement

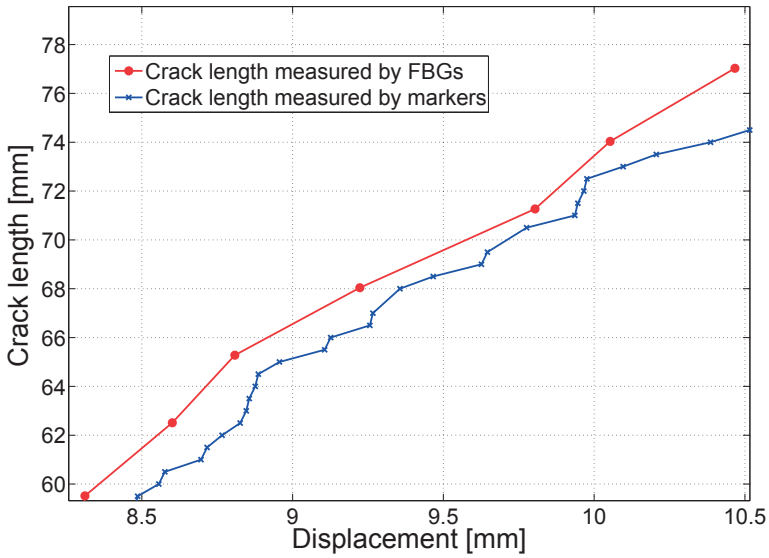

Figure 4.32: Mixed Mode $\mu = 40\%$, crack length versus applied displacement measured by side markers and FBGs

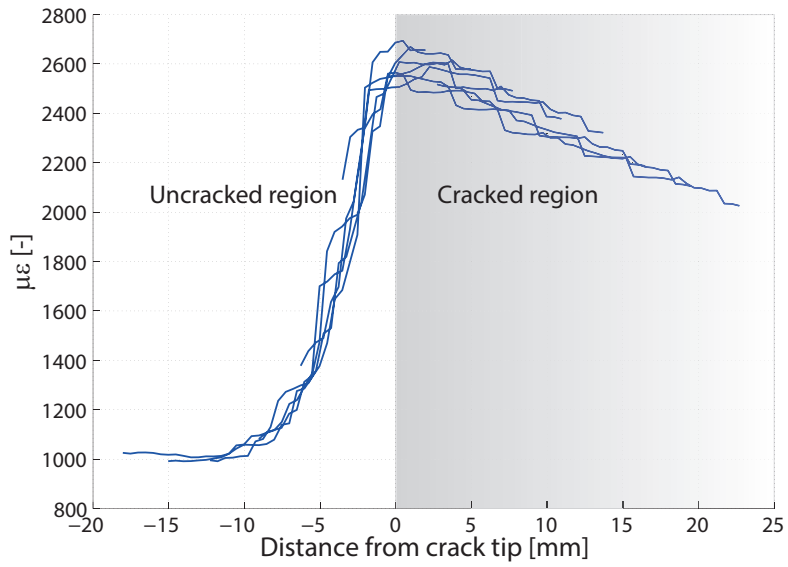

Figure 4.33: Mixed Mode $\mu = 40\%$, shifted FBGs strains to common crack tip position

4.2.4 Mixed Mode test: 60%

The Mixed Mode delamination tests performed at 30% and 40% of mode mixity well show that the amount of bridging generated between the crack faces is small, especially if compared with the one obtained in Mode I and 20% Mixed mode. The test at $\mu = 60\%$ is, therefore, performed to obtain extra information in terms of load displacement curve, crack length and ERR to compare with a numerical finite element model. As expected, the test is found to be the more unstable, with frequent crack jumps and, therefore, relevant scatter between the different specimens. As for the 40% case, only stable tests are kept to compute average curves. Figure 4.34 shows the average load-displacement curve while the crack propagation is displayed in Figure 4.35. The standard deviation is clearly high, especially after the initiation, generated by the lack of bridging and the high Mode II component.

The measured ERR, shown in Figure 4.36, points out that the energy at crack initiation $G_c = 530\frac{J}{m^2}$ is higher with respect to the lower mode mixities. However, the contribution of bridging $G_b \backsimeq 40\frac{J}{m^2}$ is almost negligible, as proved by Figure 4.37 which shows the lack of bridging fibres in the middle of the crack.

Since the scatter over the 60% mode mixity is relevant and the bridging tractions are almost negligible, the results from the optical fiber are not meaningful.

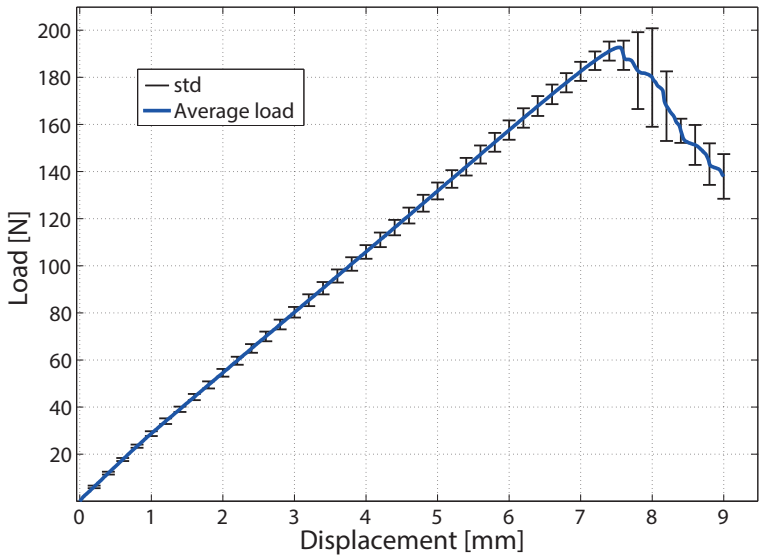

Figure 4.34: Mixed Mode $\mu = 60\%$, average load-displacement curve and standard deviation

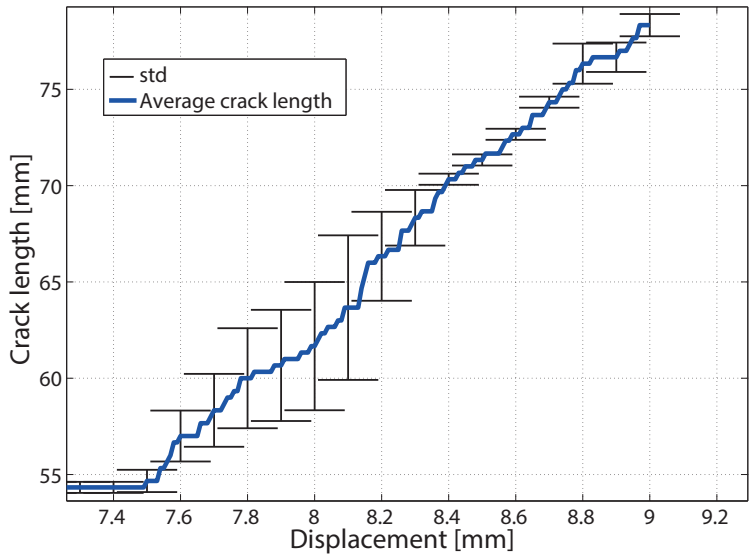

Figure 4.35: Mixed Mode $\mu = 60\%$, crack length measured by markers versus applied displacement

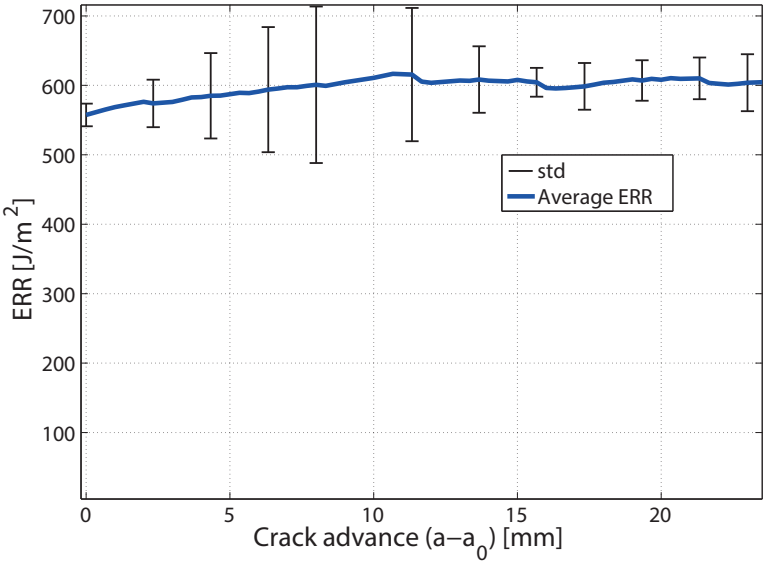

Figure 4.36: Mixed Mode $\mu = 60\%$, ERR. Critical value at crack initiation and evolution with crack propagation

Figure 4.37: Mixed Mode $\mu = 60\%$, bridging tractions in the middle of the crack at $\triangle a = 20mm$

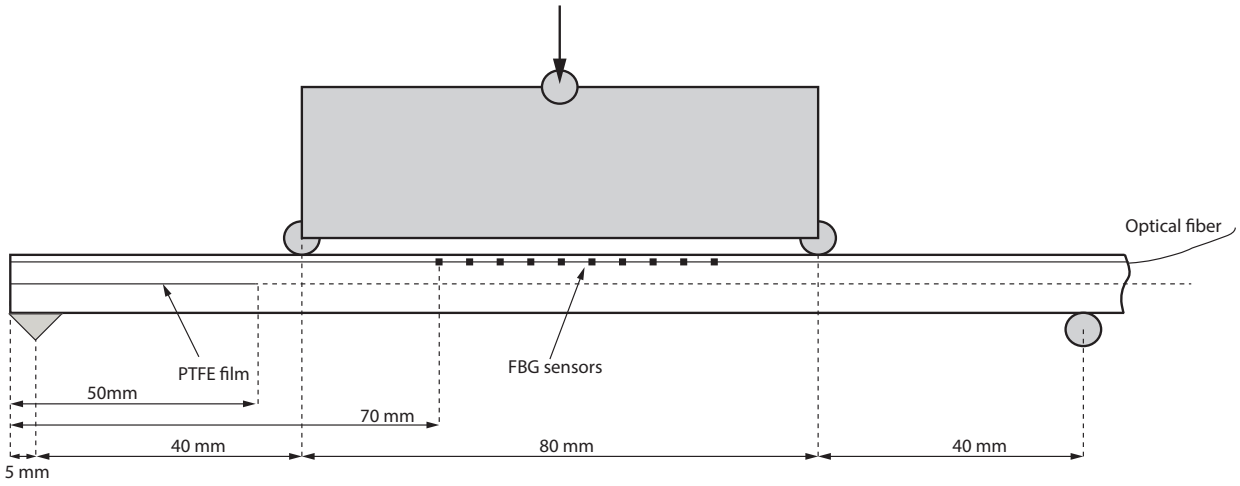

Figure 4.38: Mode II 4ENF setting. Specimen and embedded optical fiber

4.3 Mode II delamination test

The Mode II delamination test is performed by using a 4ENF setting. This setup allows for obtaining a wide central region for crack propagation in which the applied moment is constant. The stability of crack propagation represents the main requirement when the behavior after the onset is studied. By literature review and the experiments, the 4ENF if found to be the best choice to study the crack propagation in pure shear. Figure 4.38 shows the schematic setting, the specimen and the position of the embedded fiber.

By using the 4ENF setting, the crack propagation is found to be stable if combined with very low displacement rates, equal to $0.6mm/min$. Figure 4.39 shows the average load-displacement curve and standard deviation calculated over five specimens. The crack length versus applied displacement is shown in Figure 4.40.

In order to calculate the ERR, the initiation point is set by evaluating a 5% difference on the initial compliance. The first part shows a nonlinear compliance which is due to the fixture as also discussed in the ASTM standards for 3ENF tests [97]. The curve, shown in Figure 4.41, is almost flat which indicates a lack of fiber bridging. The energy at initiation is $G_c = 1100\frac{J}{m^2}$ with a standard deviation of $\pm 40\frac{J}{m^2}$. The complete lack of bridging is well pointed out by the Figure 4.42, in which the specimen is opened by using a wedge after the 4 ENF test.

Optical fibers are also embedded in the specimen. Figure 4.43 shows the strains measured during the Mode II delamination test.

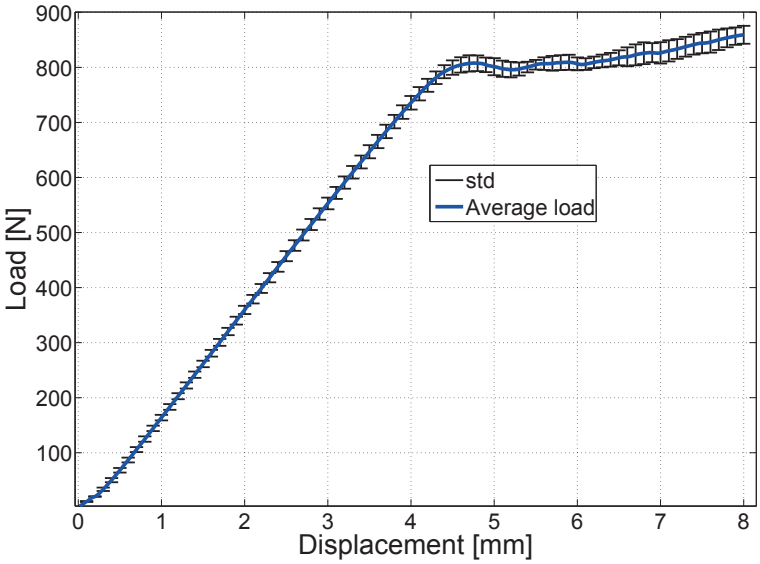

Figure 4.39: Mode II, average load-displacement curve and standard deviation

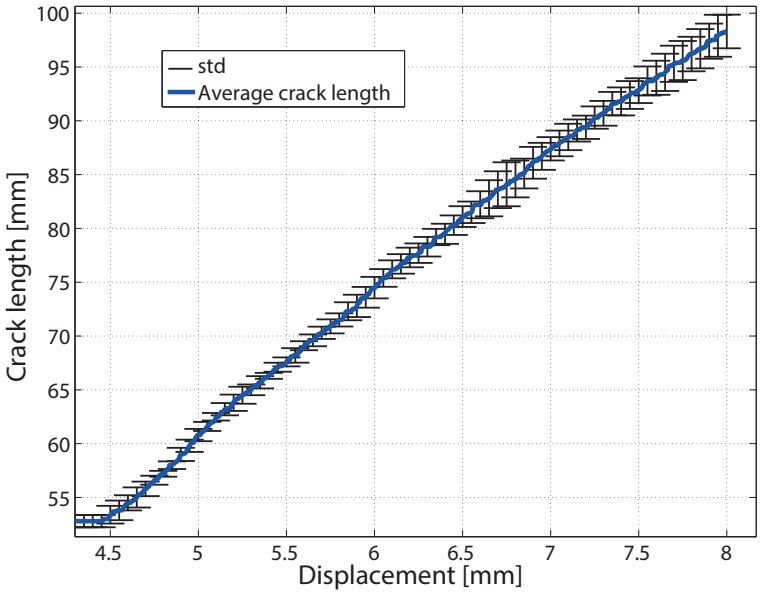

Figure 4.40: Mode II, crack length measured by markers versus applied displacement

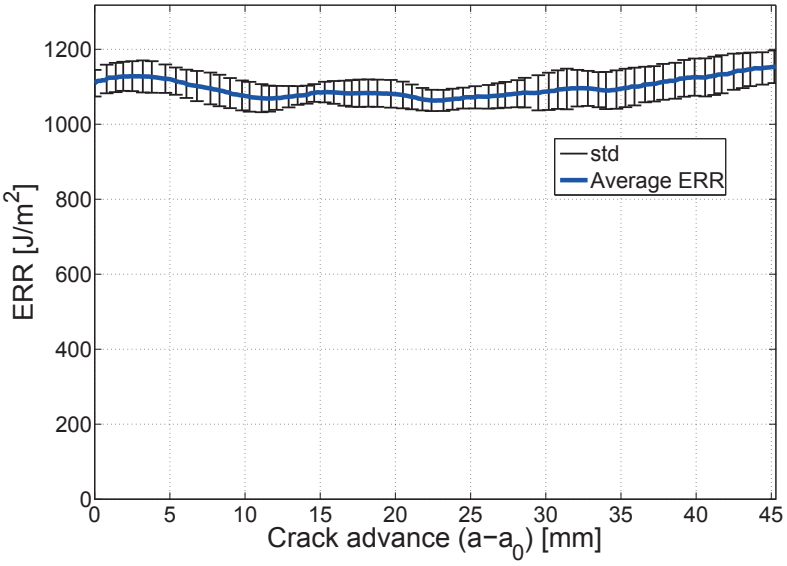

Figure 4.41: Mode II ERR. Critical value at crack initiation and evolution with crack propagation

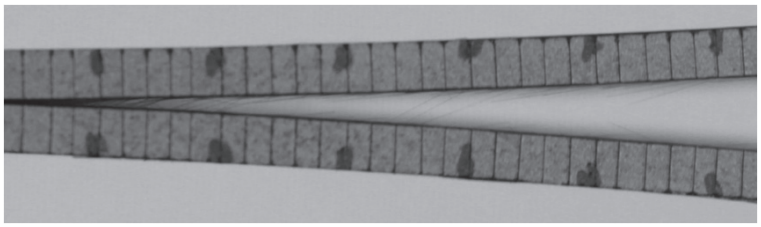

Figure 4.42: Mode II, no bridging tractions in the middle of the crack. Picture taken by opening the specimen in Mode I after the 4ENF test

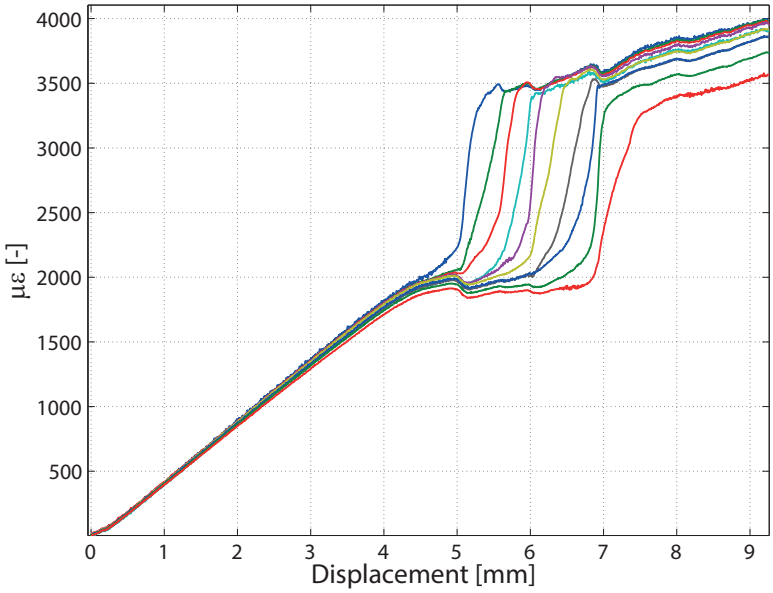

Figure 4.43: Mode II, strains measured by Multiplexed FBGs as a function of the applied displacement

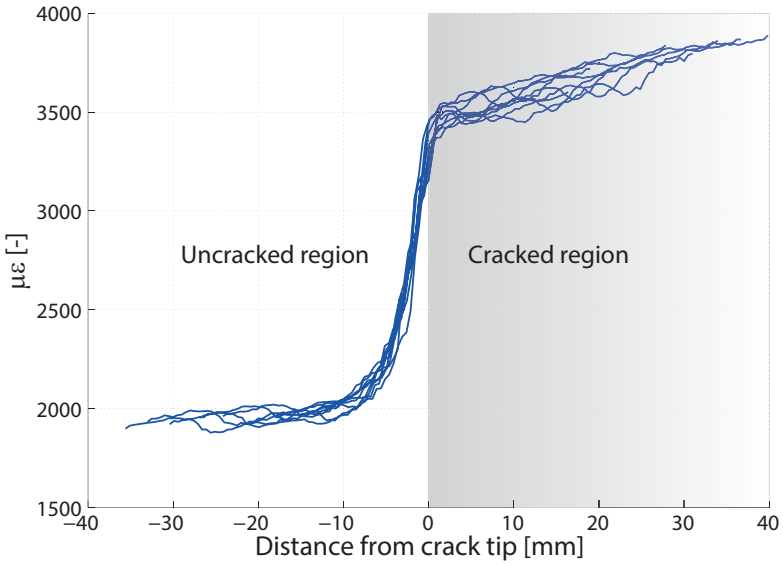

Figure 4.44: Mode II, shifted FBGs strain to common crack tip position

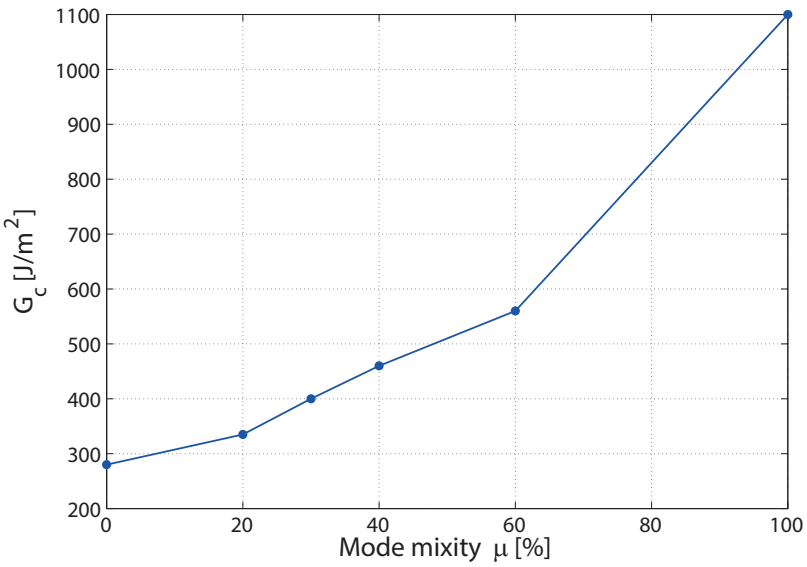

Figure 4.45: ERR at crack initiation as a function of mode mixity μ[%]

4.4 Summary

This work combines several delamination tests performed in pure Mode I, 20%, 30%, 40%, 60% Mixed Mode and pure Mode II. The corresponding experimental results provide an important set of data to shed some light on the influence of the mode mixity on the fracture toughness G_c and the contribution of bridging in unidirectional composite laminates.

Figure 4.45 shows the trend of the G_c as a function of the applied mode mixity. The curve can be fitted by the Benzeggagh and Kenane relationship [54].

The contribution of bridging also changes with the mode mixity. In Mode I delamination, bridging represents an important contribution to the total fracture energy as proved by the significant amount of bridging fibers clearly visible in the cracked area. On the other side, in pure Mode II delamination, no toughening processes occur. In Figure 4.46 the bridging contribution in terms of energy is shown as a function of the applied mode mixity. Since in the 20% delamination test a complete development of bridging is not reached, we can assume that the corresponding energy contribution is higher than the one calculated as $G_{tot} - G_c$, as indicated by the bar line.

A visual comparison of the bridging fibers, developed during the delamination process, is shown in Figure 4.47. As it is clear from the pictures, in Mode I and 20% Mixed Mode delamination a large scale bridging occurs. An important amount of fibers, represented by the dark area

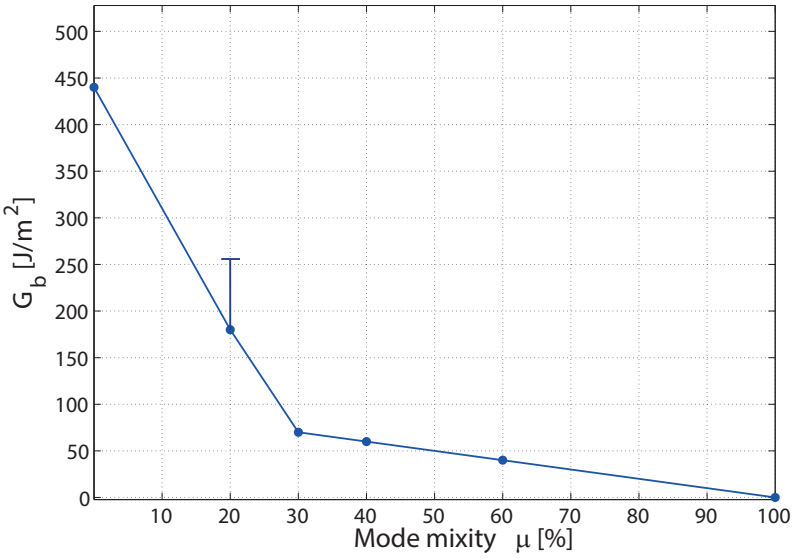

Figure 4.46: Bridging contribution G_b as a function of mode mixity $\mu[\%]$

in the middle of the crack, is involved acting as a toughening mechanism. If the mode mixity increases, the amount of active bridging fibers quickly decreases. The specimen performed in Mode II is opened after the 4ENF test in order to show the complete lack of bridging fibers.

Figure 4.48 shows the combined ERR curves, obtained from the experiments performed at different mode mixities. Note here the difference in terms of bridging contribution between Mode I delamination and the other tests. Delamination in Mode I occurs at a lower G_c value compared to the other curves but it develops enough bridging to increase the fracture toughness up to $\sim 720\frac{J}{m^2}$. For higher mode mixities, the initiation point increases but the bridging developed during the crack propagation does not increase significantly the total toughness. Starting from these experimental results, it is possible to conclude that a large scale bridging mainly occurs in Mode I and 20% Mixed Mode delamination tests, while its contribution becomes small for mode mixities $\mu > 30\%$.

A numerical model shown in Chapter 5, with cohesive elements to simulate the crack propagation, will better highlight the influence of bridging for each delamination test in terms of crack propagation, load displacement curve, ERR and strains over the FBGs path.

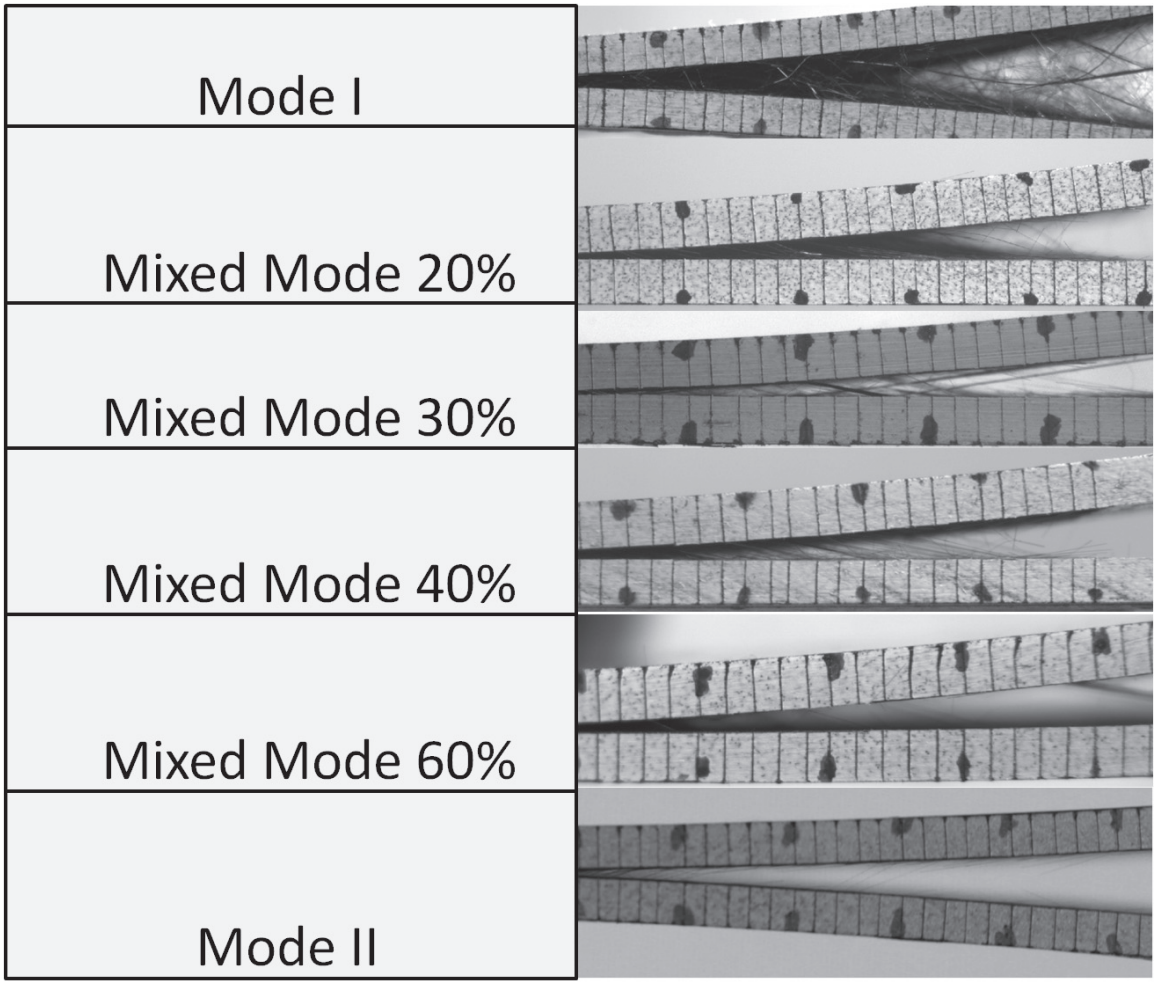

Figure 4.47: Bridging fibers involved during the delamination process, for different mode mixities

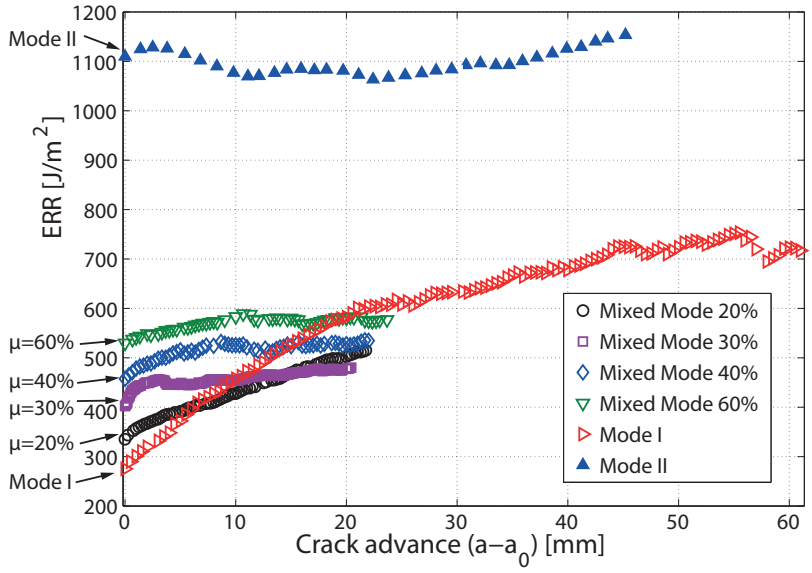

Figure 4.48: ERR curves for different mode mixities, as a function of the crack propagation

Chapter 5

Traction separation law in Mixed Mode delamination and optimization approach

The numerical FE Models known so far, implemented in the commercial software to simulate the fracture behavior in Mixed Mode delamination, do not provide accurate results, especially when large scale bridging occurs. In this chapter both the standard numerical models and an innovative implementation based on cohesive elements are described. The main issues which affect the numerical simulations of Mixed Mode delamination are pointed out, analyzed and solved.

The optimization process scheme, used to characterize the bridging tractions, is also described for Mode I and Mixed Mode tests. The optimization process allows obtaining the parameters which characterize the bridging tractions acting on the crack faces. This approach, also called indirect method, combines experimental results with the ones obtained by the FE Model. The main characteristics of the numerical model, the corresponding mode mixity definition and the method to distribute the proper bridging contribution are described in the following sections.

5.1 Optimization scheme

The optimization scheme, presented in this work, combines experimental and numerical results. In this particular case, the objective function is represented by the least square mismatch of the strains measured by the Multiplexed FBGs embedded in the tested specimens and the ones obtained by the FE Model. By changing the bridging parameters in the numerical model, the

optimization process is able to determine the best set of parameters which allows the optimal match between the experimental and the numerical results. The optimization code is implemented by using the *lsqnonlin* solver of the commercial software Matlab®.

The error function F, dependent on the parameters $\overline{x} = [x_i]$ describing the bridging tractions, is defined as:

$$F(\overline{x}) = \frac{1}{2} \| \frac{\varepsilon_{FBG} - \varepsilon_{FEM}}{\varepsilon_{FBG}} \|^2 \tag{5.1}$$

where ε_{FBG} and ε_{FEM} respectively represent the strains measured by the FBGs and the ones obtained by the numerical model.

The best set of parameters is based on the evaluation of the Jacobian, which represents the partial derivative of $F(x_i)$ with respect to the corresponding parameter x_i. The nonlinear equation is solved by using the *trust-region-reflective* algorithm which involves the Newton method and allows for parameter bounds.

The optimization process starts from a first set of parameters $X = [x_i]$, close to the optimal solution in order to avoid convergence issues and being trapped into a local minimum. The algorithm first calculates $F(X)$ and then evaluates the perturbation by changing by 1% the initial parameters. Once the Jacobian is calculated, the algorithm computes a new set of parameters. The routine keeps on until the variation of the residuals is lower than a certain threshold or by fixing the maximum number of iterations. Figure 5.1 shows the steps of the optimization scheme.

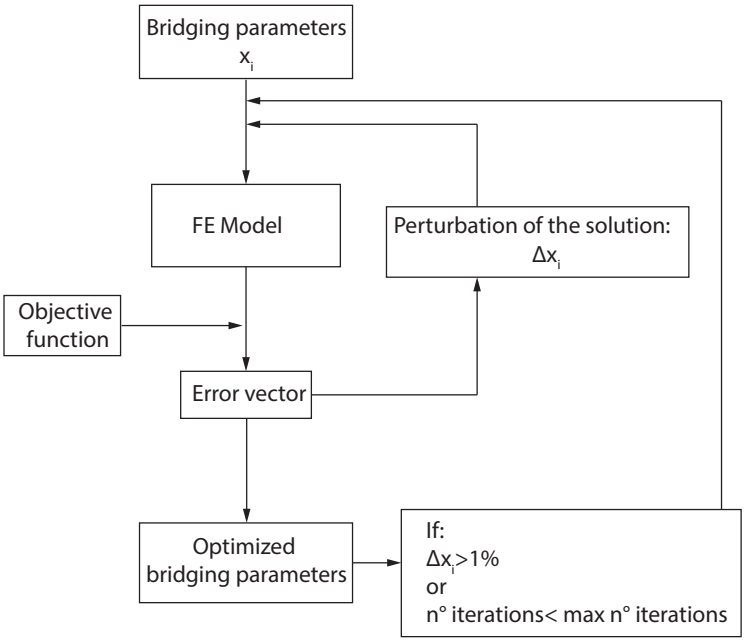

Figure 5.1: Optimization scheme for the evaluation of bridging tractions

5.2 Mode I: numerical model and bridging identification

5.2.1 Numerical model for bridging identification

The numerical approach used for bridging identification in Mode I delamination consists of a 2D planar model, composed by the upper and the lower beam meshed with quadratic elements. It does not involve cohesive elements. The mesh size is set to $\sim 0.25mm$. The crack length coincides with the position of the last FBG sensor and the corresponding displacement obtained by the experimental results is applied. On both crack faces, bridging tractions are added according to the equation 3.29. Figure 5.2 shows the FE model and the bridging tractions.

5.2.2 Optimization process for bridging identification

In Mode I delamination, a clear steady state and, therefore, a self-similar crack propagation are obtained as shown in the experiments. The FBGs sensors are placed so that the strains are measured when bridging is completely developed. Figure 5.3(a) better explains the FBGs position and the correlated strains over the bridging zone. The strain profile, measured when the crack coincides with the last sensor represents the objective data used in the optimization process. By assuming self-similar crack propagation, the strain values are measured with a variation of $\pm 1.5mm$ of crack length in order to improve the spatial resolution provided by the

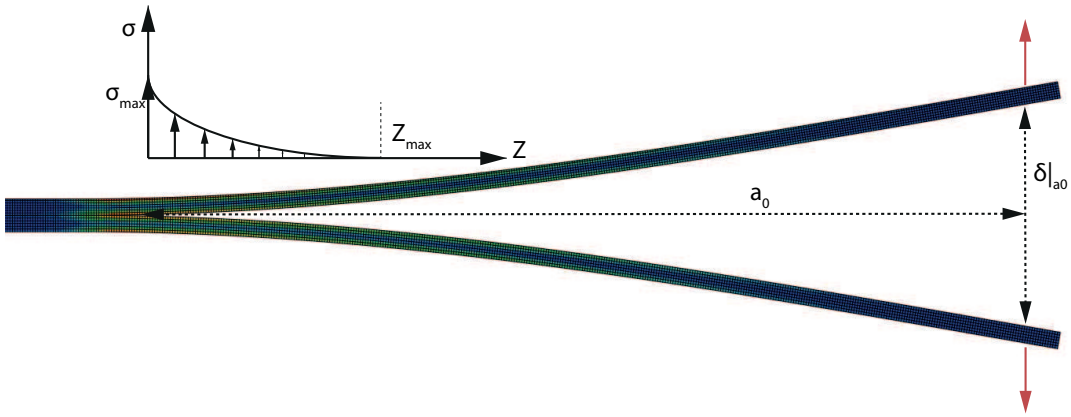

Figure 5.2: FE Model for bridging identification in Mode I delamination

10 sensors. The objective strain distribution, obtained by the FBGs, is shown in Figure 5.3(b).

The bridging traction model and the parameters σ_{max}, z_{max} and γ, chosen to represent the bridging tractions in the FE Model, are defined in section 3.4, equation 3.29. The strain field measured by the FBGs is influenced by the bridging tractions and, therefore, by σ_{max}, z_{max} and γ. The FE model is constructed specifically to represent the experimental conditions at the identification point: the experimentally applied displacement is also imposed on the loading point and a parametric surface traction model representing σ_b is implemented to reflect the effect of bridging tractions on the local strains captured by the FBGs. By using the optimization routine, the three parameters are gradually varied until the objective function is properly minimized.

The initial parameters values, used at the beginning of the optimization process, are defined after a coarse manual fitting. In this way the possibility that the algorithm could fall in a local minimum far from the best solution is avoided. Figure 5.4 shows the percentage variation of σ_{max}, z_{max} and γ with respect to the initial values, during the whole optimization process. The optimization algorithm allows for the parameters to change in order to decrease the error vector $F(\overline{x})$, defined in equation 5.1. The algorithm is found to be able to immediately reduce the error vector until a steady state is reached for both parameters and residuals. The optimized parameters set $\overline{x}_{opt}$ corresponding to the lowest value of $F(\overline{x})$ is collected in Table 5.1.

Figure 5.5 shows the comparison between the axial strains measured by the FBGs and the ones obtained by the FE model with and without bridging tractions. The relevant influence of bridging over the axial strains is pointed out by the fact that the curve with no bridging tractions is not able to properly match the FBG strains. The curve obtained after the optimization process provides an optimal fitting with the experimental one.

The corresponding cohesive law is obtained by tabulating the bridging tractions as a function

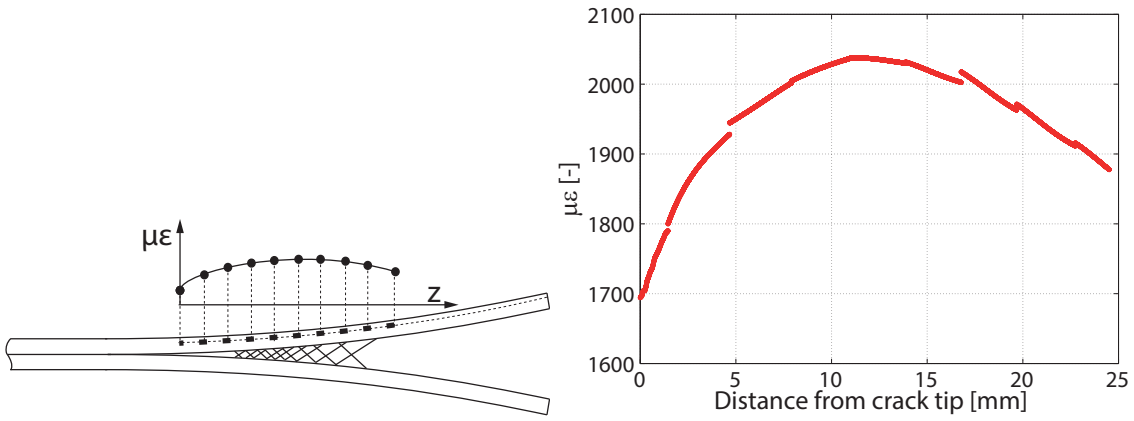

(a) (b)

Figure 5.3: Axial strain profile over the bridging zone measured by the FBG sensors: (a) schematic view (b) actual FBGs strains

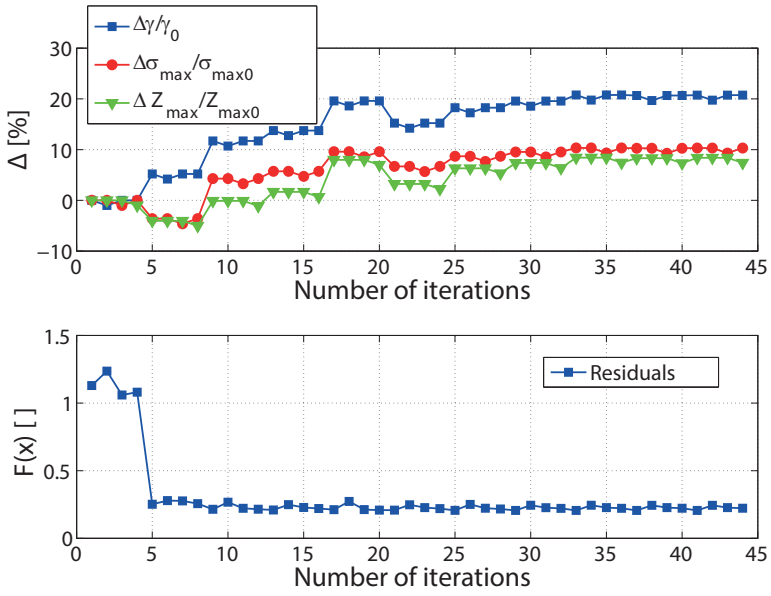

Figure 5.4: Evolution of the bridging parameters during the optimization process

Mode I bridging parameters	$\sigma_{max}[MPa]$	$z_{max}[mm]$	γ	COD δ_{max}=$\delta(z_{max})[mm]$
	0.986	41.22	0.079	5.1

Table 5.1: Optimized bridging parameters for Mode I delamination

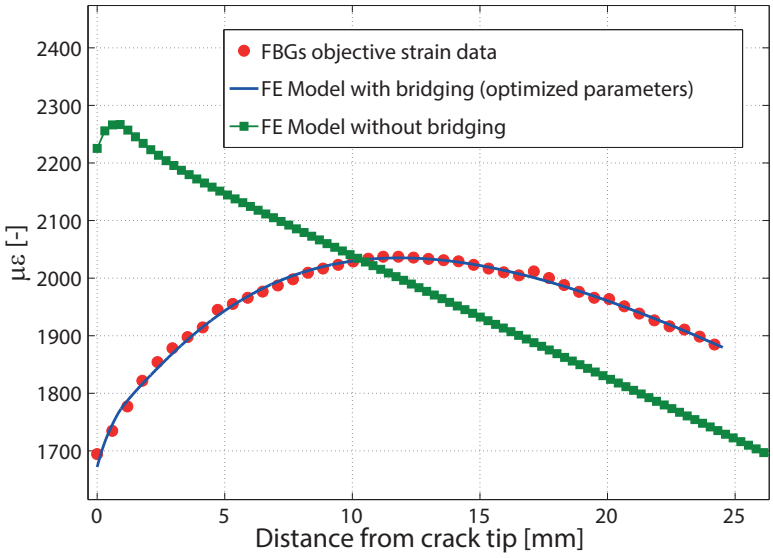

Figure 5.5: Fitting of the objective function

of the crack opening displacement δ instead of the distance from the crack tip z, as discussed in section 3.4.

A second FE Model is created and cohesive elements are added over the delamination plane in order to simulate the crack propagation. The upper and the lower cohesive nodes are collapsed in order to have a zero-thickness layer. The optimized cohesive law for Mode I delamination is shown in Figure 5.6. The critical stress at damage initiation $\sigma_{3,0} = 20MPa$ is a good approximation obtained from the epoxy resin properties. The final result in terms of crack initiation and maximum load is weakly affected by $\sigma_{3,0}$ while it is strongly dependent by the energy $G_{I,c}$. The bridging tail is very long, especially if compared with the first cohesive triangle which represents the fracture process zone. The maximum crack opening displacement at complete failure $\delta_{3,f}$, which corresponds to the maximum bridging length z_{max}, is $\delta_{3,f}(Z_{max}) = 5.1mm$. The cohesive stiffness in the linear part is set to $20.000^{MPa}/_{mm}$ based on a convergence analysis. According to the experimental results, the critical energy at initiation is $G_c = 280^{J}/_{m^2}$.

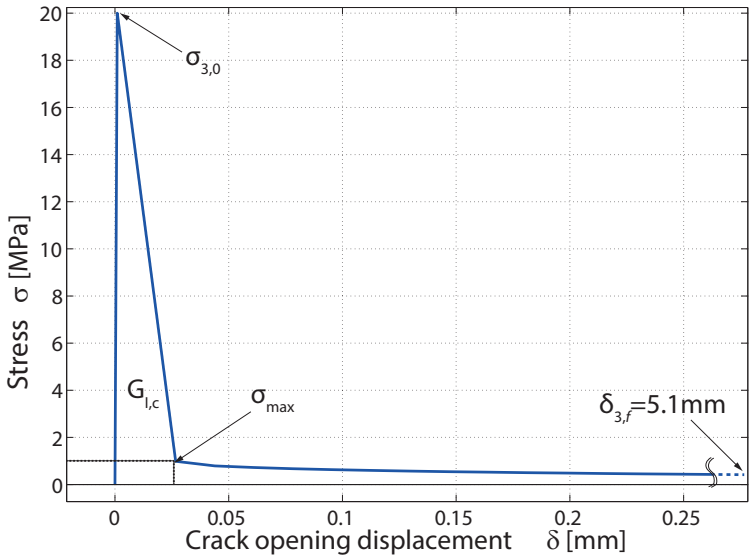

Figure 5.6: Optimized cohesive law for Mode I delamination

5.3 Mixed Mode: numerical model and bridging identification

The aim of this work is to provide a numerical tool able to simulate the crack propagation over the whole range of mode mixities between pure Mode I and Mode II. By using the same method for bridging identification used for Mode I, we can only obtain several cohesive laws, one for each mode mixity, which would represent a trivial result. For this reason, a Mode Dependent approach must be followed. In the following section, the method to obtain a mode dependent cohesive law with the proper bridging contribution is described.

5.3.1 Mode mixity with cohesive elements

If a mode dependent approach is used, the behavior of a single cohesive element depends on the applied mode mixity. The work proposed by Camanho [98] and recalled by the Abaqus® manual, aims to correlate the mode mixity $\mu = \frac{G_{II}}{G_{tot}}$ with the ratio of shear and normal displacements as:

$$\beta = \frac{\delta_1}{\delta_3} \tag{5.2}$$

where δ_1 and δ_3 respectively represents the shear and normal displacements applied to the cohesive element.

In the following part, all the main equations, used to define the stresses provided by the cohesive elements as a function of β, are explained. The general idea of these developments is to compute the Mode I and Mode II ERR by integrating the cohesive law. To do so, the following assumptions are made:

- the mode mixity is kept constant during loading
- the displacement field is self similar in the process zone.

Nomenclature

Normal direction (Mode I)

- δ_3 : displacement in normal direction
- σ_3 :normal stress
- $\sigma_{3,0}$: critical normal stress in pure Mode I at damage initiation
- $\sigma_{3,i}$: normal stress component at failure initiation under Mixed Mode conditions
- $\delta_{3,i}$: normal displacement component at failure initiation under Mixed Mode conditions
- $\delta_{3,f}$: normal displacement at complete failure (zero stress)

Shear direction (Mode II)

- δ_1 : displacement in shear direction
- σ_1 : shear stress
- $\sigma_{1,0}$: critical shear stress in pure Mode II at damage initiation
- $\sigma_{1,i}$: shear stress component at failure under Mixed Mode conditions
- $\delta_{1,i}$: shear displacement component at failure under Mixed Mode conditions
- $\delta_{1,f}$: shear displacement at complete failure (zero stress)

Mixed Mode

- $\mu = \frac{G_{II}}{G_{tot}}$: energy mode mixity
- $\beta = \frac{\delta_1}{\delta_3}$: displacement mode mixity
- δ_m : norm of the displacement vector in mixed mode
- σ_m : norm of the mixed mode cohesive surface tractions
- $\sigma_{m,i}$: norm of the mixed mode tractions at damage initiation
- $\delta_{m,i}$: norm of the mixed mode displacements at damage initiation
- $\delta_{m,f}$: norm of the mixed mode displacements at complete failure (zero stress)
- $\bar{\delta}_m$: critical displacement at a given damage $D\,|_{\overline{\delta_m}}$

Cohesive elements

- E_0 : initial element stiffness in normal and shear direction
- D : damage parameter $\left\{ \begin{array}{ll} D = 0 & No\,damage \\ D = 1 & Full\,damage \end{array} \right\}$
- $E = E_0 \cdot (1 - D)$: element stiffness associated to damage D

Energies

- G_I : ERR in Mode I
- $G_{I,c}$: critical ERR in Mode I
- G_{II} : ERR in Mode II
- $G_{II,c}$: critical ERR in Mode II

Relation between stresses and displacements

In Abaqus® , the stresses in the damaged region are defined trough the damage parameter D as:

$$\sigma_3 = E_0 \cdot (1 - D) \cdot \delta_3 \tag{5.3}$$

$$\sigma_1 = E_0 \cdot (1 - D) \cdot \delta_1 = E_0 \cdot (1 - D) \cdot \beta \cdot \delta_3. \tag{5.4}$$

Dividing member by member:

$$\frac{\sigma_1}{\sigma_3} = \frac{\delta_1}{\delta_3} = \beta \tag{5.5}$$

meaning that, when E_0 is the same for Mode I and Mode II, the ratio of displacements corresponds to the ratio of stresses and thus the stresses are collinear to displacements.

The displacement magnitude in Mixed Mode is defined as:

$$\delta_m = \sqrt{\delta_3^2 + \delta_1^2} = \delta_3 \cdot \sqrt{1 + \beta^2} \tag{5.6}$$

Therefore:

$$\delta_3 = \frac{\delta_m}{\sqrt{1 + \beta^2}} \tag{5.7}$$

and

$$\delta_1 = \frac{\beta \cdot \delta_m}{\sqrt{1 + \beta^2}}. \tag{5.8}$$

the Mixed Mode traction magnitude σ_m can be written as:

$$\sigma_m = \sqrt{\sigma_3^2 + \sigma_1^2} = \sigma_3 \cdot \sqrt{1 + \beta^2} = E_0 \cdot (1 - D) \cdot \delta_3 \sqrt{1 + \beta^2} = E_0 \cdot (1 - D) \cdot \delta_m \tag{5.9}$$

and the damage parameter as:

$$D = 1 - \frac{\sigma_m}{\delta_m \cdot E_0}. \tag{5.10}$$

Fracture initiation criterion

For pure Mode I and Mode II conditions, damage initiation occurs when the stress reaches respectively $\sigma_{3,0}$ and $\sigma_{1,0}$. In Mixed Mode delamination, a criterion which combines the two extremes must be used. In our case, a quadratic criterion is used as follows:

$$\left(\frac{\sigma_{3,i}}{\sigma_{3,0}}\right)^2 + \left(\frac{\sigma_{1,i}}{\sigma_{1,0}}\right)^2 = 1. \tag{5.11}$$

The equation 5.11 can be written as:

$$1 = \left(\frac{\sigma_{3,i}}{\sigma_{3,0}}\right)^2 + \left(\frac{\beta\sigma_{3,i}}{\sigma_{1,0}}\right)^2 = \frac{\sigma_{1,0}^2 \cdot \sigma_{3,i}^2 + \sigma_{3,0}^2 \cdot \sigma_{3,i}^2 \cdot \beta^2}{\sigma_{3,0}^2 \cdot \sigma_{1,0}^2} = \frac{\sigma_{3,i}^2 \cdot \left(\sigma_{1,0}^2 + \sigma_{3,0}^2 \cdot \beta^2\right)}{\sigma_{3,0}^2 \cdot \sigma_{1,0}^2} \tag{5.12}$$

which leads to the corresponding normal and shear stresses and displacements at fracture initiation:

$$\sigma_{3,i} = \sqrt{\frac{\sigma_{3,0}^2 \cdot \sigma_{1,0}^2}{\sigma_{1,0}^2 + \sigma_{3,0}^2 \cdot \beta^2}} \tag{5.13}$$

$$\sigma_{1,i} = \beta \cdot \sqrt{\frac{\sigma_{3,0}^2 \cdot \sigma_{1,0}^2}{\sigma_{1,0}^2 + \sigma_{3,0}^2 \cdot \beta^2}} \tag{5.14}$$

$$\delta_{3,i} = \frac{\sigma_{3,i}}{E_0} \tag{5.15}$$

$$\delta_{1,i} = \frac{\sigma_{1,i}}{E_0} \tag{5.16}$$

The stress and displacement magnitudes in Mixed Mode at fracture initiation are written as:

$$\sigma_{m,i} = \sqrt{\sigma_{3,i}^2 + \sigma_{1,i}^2} = \sqrt{\frac{\sigma_{3,0}^2 \cdot \sigma_{1,0}^2}{\sigma_{1,0}^2 + \sigma_{3,0}^2 \cdot \beta^2} \cdot (1 + \beta^2)} \tag{5.17}$$

$$\delta_{m,i} = \frac{\sigma_{m,i}}{E_0}. \tag{5.18}$$

5.3.1.1 Relationship between β and μ

Case 1: $\delta = \delta_f$

According to the formula proposed by Camanho, the relationship between the mode mixity μ in terms of energy and β is obtained from the following equations:

$$G_I = \frac{\sigma_{3,i} \cdot \delta_{3,f}}{2} \tag{5.19}$$

$$G_{II} = \frac{\sigma_{1,i} \cdot \delta_{1,f}}{2} = \frac{\beta^2 \cdot \sigma_{3,i} \cdot \delta_{3,f}}{2} \tag{5.20}$$

$$G_{tot} = G_I + G_{II} = \frac{\sigma_{3,i} \cdot \delta_{3,f}}{2} \cdot \left(1 + \beta^2\right) \tag{5.21}$$

$$\mu(\beta) = \frac{G_{II}}{G_{tot}} = \frac{\beta^2}{1 + \beta^2}. \tag{5.22}$$

Equation 5.22 is calculated for $\delta = \delta_f$. This means that for $\delta_i < \delta < \delta_f$ the relationship is not supposed to be valid anymore. Note that the calculation of G_I and G_{II} performed here supposes that the mode mixity does not change in the process zone and thus the integrals are very simple to compute.

The definition of the mode mixity for $\delta_i < \delta < \delta_f$ is explained in Case 2.

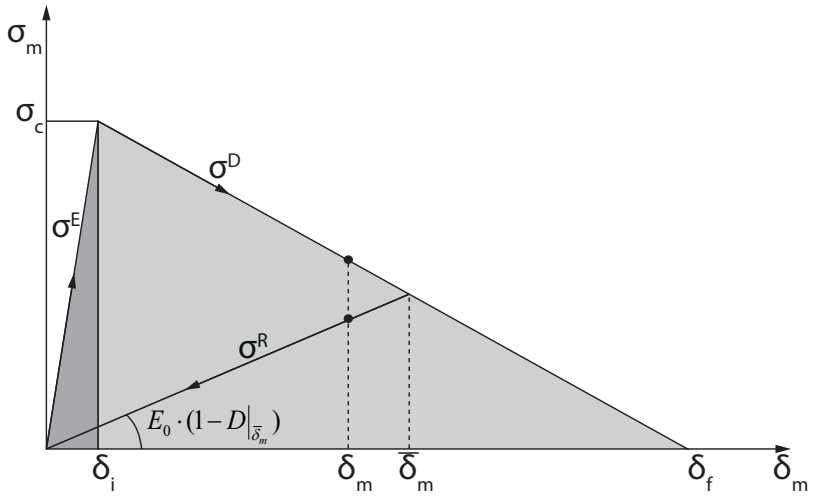

Figure 5.7: Cohesive law with linear decay

Case 2: $\delta_i < \delta < \delta_f$

According to Figure 5.7, the stresses provided by a cohesive element at a constant mode mixity β are defined as:

σ_m^E = linear elastic stress before fracture initiation
σ_m^D = stress in damaged region
σ_m^R = release linear elastic stress at damage $\overline{D}$
$K = \frac{\sigma_{\mathrm{m,i}}}{\delta_{m,f}-\delta_{m,i}}$
$a = \frac{\sigma_{\mathrm{m,i}}\cdot\delta_{m,f}}{\delta_{m,f}-\delta_{m,i}}$

$$\sigma_m\,|_\beta = \begin{cases} \sigma_m^E & E_0\cdot\delta_m & 0<\delta_m\le\delta_{m,i} \\ \sigma_m^D \quad = & a-K\cdot\delta_m & \delta_{m,i}<\delta_m\le\delta_{m,f} \\ \sigma_m^R & \left(1-D\,|_{\overline{\delta_m}}\right)\cdot E_0\cdot\delta_m & 0<\delta_m<\overline{\delta}_m \end{cases} \tag{5.23}$$

$$= \begin{cases} E_0\cdot\delta_m & 0<\delta_m\le\delta_{m,i} \\ \frac{\sigma_{\mathrm{m,i}}\cdot\delta_{m,f}}{\delta_{m,f}-\delta_{m,i}} - \frac{\sigma_{\mathrm{m,i}}}{\delta_{m,f}-\delta_{m,i}}\cdot\delta_m & \delta_{m,i}<\delta_m\le\delta_{m,f} \\ \left(1-D\,|_{\overline{\delta_m}}\right)\cdot E_0\cdot\delta_m & 0<\delta_m<\overline{\delta}_m \end{cases}$$

$$= \begin{cases} E_0\cdot\delta_m & 0<\delta_m\le\delta_{m,i} \\ \frac{\sigma_{\mathrm{m,i}}\cdot\left(\delta_{m,f}-\delta_m\right)}{\delta_{m,f}-\delta_{m,i}} & \delta_{m,i}<\delta_m\le\delta_{m,f} \\ \left(1-D\,|_{\overline{\delta_m}}\right)\cdot E_0\cdot\delta_m & 0<\delta_m<\overline{\delta}_m \end{cases}$$

$$= \begin{cases} E_0 \cdot \delta_m & 0 < \delta_m \leq \delta_{m,i} \\ \frac{E_0 \cdot \delta_{\mathrm{m,i}} \cdot \left(\delta_{m,f} - \delta_m\right)}{\delta_{m,f} - \delta_{m,i}} & \delta_{m,i} < \delta_m \leq \delta_{m,f} \\ \left(1 - D\,|_{\overline{\delta_m}}\right) \cdot E_0 \cdot \delta_m & 0 < \delta_m < \overline{\delta}_m \end{cases} \tag{5.24}$$

The damage parameter D can be written as:

$$\sigma_m^D = (1 - D) \cdot E_0 \cdot \delta_m$$

$$\rightarrow \left(1 - D\,|_{\overline{\delta_m}}\right) = \frac{\delta_{\mathrm{m,i}} \cdot \left(\delta_{m,f} - \overline{\delta_m}\right)}{\left(\delta_{m,f} - \delta_{m,i}\right) \overline{\delta_m}} \tag{5.25}$$

$$\rightarrow D\,|_{\overline{\delta_m}} = 1 - \frac{\delta_{\mathrm{m,i}} \cdot \left(\delta_{m,f} - \overline{\delta_m}\right)}{\left(\delta_{m,f} - \delta_{m,i}\right) \overline{\delta_m}} \tag{5.26}$$

Combining equations 5.24 and 5.25, $\sigma_m\,|_\beta$ becomes:

$$\sigma_m\,|_\beta = \begin{cases} E_0 \cdot \delta_m & 0 < \delta_m \leq \delta_{m,i} \\ \frac{E_0 \cdot \delta_{\mathrm{m,i}} \cdot \left(\delta_{m,f} - \delta_m\right)}{\delta_{m,f} - \delta_{m,i}} & \delta_{m,i} < \delta_m \leq \delta_{m,f} \\ \frac{\delta_{\mathrm{m,i}} \cdot \left(\delta_{m,f} - \overline{\delta_m}\right)}{\left(\delta_{m,f} - \delta_{m,i}\right) \overline{\delta_m}} \cdot E_0 \cdot \delta_m & 0 < \delta_m < \overline{\delta}_m \end{cases} \tag{5.27}$$

Integrals

The ERR at a constant mode mixity β in Mixed Mode conditions is calculated as the integral of σ_m with respect to δ_m:

$$\overline{G}\,|_{\beta}= \int_0^{\overline{\delta}_m} \sigma_m \cdot d\delta_m. \tag{5.28}$$

The integrals in the linear elastic and damaged regions are defined as:

- For $0 < \delta_m < \delta_{m,i}$ $\qquad \sigma_m^E(\delta_m) = E_0 \cdot \delta_m$

$$\overline{G^E}\,|_{\beta}= \int E_0 \cdot \delta_m \cdot d\delta_m = \frac{E_0 \cdot \delta_m^2}{2} \tag{5.29}$$

- For $\delta_{m,i} < \delta_m < \delta_{m,f}$ $\qquad \sigma_m^D(\delta_m) = a - K \cdot \delta_m$

$$\overline{G^D}\,|_{\beta}= \int a - K \cdot \delta_m \cdot d\delta_m = a \cdot \delta_m - \frac{K \cdot \delta_m^2}{2} = \frac{\sigma_{\mathrm{m,i}} \cdot \delta_{m,f}}{\delta_{m,f} - \delta_{m,i}} \cdot \delta_m - \frac{1}{2}\frac{\sigma_{\mathrm{m,i}} \cdot \delta_m^2}{\delta_{m,f} - \delta_{m,i}}$$

$$= \frac{E_0 \cdot \delta_{\mathrm{m,i}} \cdot \delta_{m,f}}{\delta_{m,f} - \delta_{m,i}} \cdot \delta_m - \frac{1}{2}\frac{E_0 \cdot \delta_{\mathrm{m,i}} \cdot \delta_m^2}{\delta_{m,f} - \delta_{m,i}} \tag{5.30}$$

- For $0 < \delta_m < \delta_{m,i}$

$$\overline{G^R}\,|_{\beta}= \int \frac{\delta_{\mathrm{m,i}} \cdot \left(\delta_{m,f} - \overline{\delta_m}\right)}{\left(\delta_{m,f} - \delta_{m,i}\right)\overline{\delta_m}} \cdot E_0 \cdot \delta_m \cdot d\delta_m = \frac{\delta_{\mathrm{m,i}} \cdot \left(\delta_{m,f} - \overline{\delta_m}\right)}{\left(\delta_{m,f} - \delta_{m,i}\right)\overline{\delta_m}} \cdot E_0 \cdot \frac{\delta_m^2}{2} \tag{5.31}$$

Energies

The energies G_I, G_{II} and G_{tot} are written as a function of δ_m.

The Mode I contribution to ERR is:

$$G_I\mid_\beta = \int_0^{\delta_{3,\mathrm{i}}} \sigma_3^E \cdot d\delta_3^E + \int_{\delta_{3,\mathrm{i}}}^{\delta_3} \sigma_3^D \cdot d\delta_3^D - \int_0^{\delta_3} \sigma_3^R \cdot d\delta_3^R$$

$$= \int_0^{\frac{\delta_{\mathrm{m,i}}}{\sqrt{1+\beta^2}}} \frac{\sigma_m^E}{\sqrt{1+\beta^2}} \cdot \frac{d\delta_{\mathrm{m}}}{\sqrt{1+\beta^2}} + \int_{\frac{\delta_{\mathrm{m,i}}}{\sqrt{1+\beta^2}}}^{\frac{\delta_{\mathrm{m}}}{\sqrt{1+\beta^2}}} \frac{\sigma_m^D}{\sqrt{1+\beta^2}} \cdot \frac{d\delta_{\mathrm{m}}}{\sqrt{1+\beta^2}} - \int_0^{\frac{\delta_{\mathrm{m}}}{\sqrt{1+\beta^2}}} \frac{\sigma_m^R}{\sqrt{1+\beta^2}} \cdot \frac{d\delta_{\mathrm{m}}}{\sqrt{1+\beta^2}}$$

$$= \int_0^{\frac{\delta_{\mathrm{m,i}}}{\sqrt{1+\beta^2}}} \frac{\sigma_m^E}{1+\beta^2} d\delta_{\mathrm{m}} + \int_{\frac{\delta_{\mathrm{m,i}}}{\sqrt{1+\beta^2}}}^{\frac{\delta_{\mathrm{m}}}{\sqrt{1+\beta^2}}} \frac{\sigma_m^D}{1+\beta^2} d\delta_{\mathrm{m}} - \int_0^{\frac{\delta_{\mathrm{m}}}{\sqrt{1+\beta^2}}} \frac{\sigma_m^R}{1+\beta^2} d\delta_{\mathrm{m}}$$

$$= \frac{1}{1+\beta^2} \cdot \overline{G^E}\mid_\beta \left(0, \frac{\delta_{\mathrm{m,i}}}{\sqrt{1+\beta^2}}\right) + \frac{1}{1+\beta^2} \cdot \overline{G^D}\mid_\beta \left(\frac{\delta_{\mathrm{m,i}}}{\sqrt{1+\beta^2}}, \frac{\delta_m}{\sqrt{1+\beta^2}}\right) - \frac{1}{1+\beta^2} \cdot \overline{G^R}\mid_\beta \left(0, \frac{\delta_m}{\sqrt{1+\beta^2}}\right)$$

$$= \frac{1}{1+\beta^2} \cdot \left[\overline{G^E}\mid_\beta \left(0, \frac{\delta_{\mathrm{m,i}}}{\sqrt{1+\beta^2}}\right) + \overline{G^D}\mid_\beta \left(\frac{\delta_{\mathrm{m,i}}}{\sqrt{1+\beta^2}}, \frac{\delta_m}{\sqrt{1+\beta^2}}\right) - \overline{G^R}\mid_\beta \left(0, \frac{\delta_m}{\sqrt{1+\beta^2}}\right)\right] \tag{5.32}$$

$$= \frac{1}{1+\beta^2} \cdot [\frac{E_0 \cdot \delta_{m,i}^2}{2\left(1+\beta^2\right)} + \frac{E_0 \cdot \delta_{\mathrm{m,i}} \cdot \delta_{m,f}}{\delta_{m,f} - \delta_{m,i}} \cdot \frac{(\delta_m - \delta_{m,i})}{\sqrt{1+\beta^2}} - \frac{1}{2} \frac{E_0 \cdot \delta_{\mathrm{m,i}}}{\delta_{m,f} - \delta_{m,i}} \cdot \frac{\left(\delta_m^2 - \delta_{m,i}^2\right)}{1+\beta^2} +$$

$$- \frac{\delta_{\mathrm{m,i}} \cdot \left(\delta_{m,f} - \overline{\delta_m}\right)}{\left(\delta_{m,f} - \delta_{m,i}\right)\overline{\delta_m}} \cdot E_0 \cdot \frac{\delta_m^2}{2\left(1+\beta^2\right)}] \tag{5.33}$$

The Mode II contribution to ERR is:

$$G_{II}\mid_{\beta}=\int_0^{\delta_{1,\mathrm{i}}}\sigma_1^E\cdot d\delta_1^E+\int_{\delta_{1,\mathrm{i}}}^{\delta_1}\sigma_1^D\cdot d\delta_1^D-\int_0^{\delta_1}\sigma_1^R\cdot d\delta_1^R$$

$$=\int_0^{\frac{\beta\cdot\delta_{\mathrm{m,i}}}{\sqrt{1+\beta^2}}}\frac{\beta\cdot\sigma_m^E}{\sqrt{1+\beta^2}}\cdot\frac{\beta\cdot d\delta_{\mathrm{m}}}{\sqrt{1+\beta^2}}+\int_{\frac{\beta\cdot\delta_{\mathrm{m,i}}}{\sqrt{1+\beta^2}}}^{\frac{\beta\cdot\delta_{\mathrm{m}}}{\sqrt{1+\beta^2}}}\frac{\beta\cdot\sigma_m^D}{\sqrt{1+\beta^2}}\cdot\frac{\beta\cdot d\delta_{\mathrm{m}}}{\sqrt{1+\beta^2}}-\int_0^{\frac{\beta\cdot\delta_{\mathrm{m}}}{\sqrt{1+\beta^2}}}\frac{\beta\cdot\sigma_m^R}{\sqrt{1+\beta^2}}\cdot\frac{\beta\cdot d\delta_{\mathrm{m}}}{\sqrt{1+\beta^2}}$$

$$=\int_0^{\frac{\beta\cdot\delta_{\mathrm{m,i}}}{\sqrt{1+\beta^2}}}\frac{\beta^2\sigma_m^E}{1+\beta^2}d\delta_{\mathrm{m}}+\int_{\frac{\beta\cdot\delta_{\mathrm{m,i}}}{\sqrt{1+\beta^2}}}^{\frac{\beta\cdot\delta_{\mathrm{m}}}{\sqrt{1+\beta^2}}}\frac{\beta^2\sigma_m^D}{1+\beta^2}d\delta_{\mathrm{m}}-\int_0^{\frac{\beta\cdot\delta_{\mathrm{m}}}{\sqrt{1+\beta^2}}}\frac{\beta^2\sigma_m^R}{1+\beta^2}d\delta_{\mathrm{m}}$$

$$=\frac{\beta^2}{1+\beta^2}\cdot\left[\overline{G^E}\mid_{\beta}\left(0,\frac{\beta\cdot\delta_{\mathrm{m,i}}}{\sqrt{1+\beta^2}}\right)+\overline{G^D}\mid_{\beta}\left(\frac{\beta\cdot\delta_{\mathrm{m,i}}}{\sqrt{1+\beta^2}},\frac{\beta\cdot\delta_m}{\sqrt{1+\beta^2}}\right)-\overline{G^R}\mid_{\beta}\left(0,\frac{\beta\cdot\delta_m}{\sqrt{1+\beta^2}}\right)\right] \tag{5.34}$$

$$=\frac{\beta^2}{1+\beta^2}\cdot\left[\frac{E_0}{2}\cdot\frac{\beta^2\cdot\delta_{\mathrm{m,i}}^2}{1+\beta^2}+\frac{E_0\cdot\delta_{\mathrm{m,i}}\cdot\delta_{m,f}}{\delta_{m,f}-\delta_{m,i}}\cdot\frac{\beta}{\sqrt{1+\beta^2}}\cdot(\delta_m-\delta_{m,i})-\frac{1}{2}\frac{E_0\cdot\delta_{\mathrm{m,i}}}{\delta_{m,f}-\delta_{m,i}}\cdot\frac{\beta^2}{1+\beta^2}\cdot\left(\delta_m^2-\delta_{m,i}^2\right)+\right.$$

$$\left.-\frac{\delta_{\mathrm{m,i}}\cdot\left(\delta_{m,f}-\overline{\delta_m}\right)}{(\delta_{m,f}-\delta_{m,i})\,\overline{\delta_m}}\cdot E_0\cdot\frac{\beta^2}{1+\beta^2}\cdot\frac{\delta_m^2}{2}\right] \tag{5.35}$$

The total ERR is obtained by the sum of G_I and G_{II} which gives:

$$G_{tot}\mid_{\beta} = G_I\mid_{\beta} + G_{II}\mid_{\beta}$$

$$= \frac{1}{1+\beta^2}\cdot\left[\frac{E_0\cdot\delta_{m,i}^2}{2\left(1+\beta^2\right)} + \frac{E_0\cdot\delta_{\mathrm{m,i}}\cdot\delta_{m,f}}{\delta_{m,f}-\delta_{m,i}}\cdot\frac{\left(\delta_m-\delta_{m,i}\right)}{\sqrt{1+\beta^2}} - \frac{1}{2}\frac{E_0\cdot\delta_{\mathrm{m,i}}}{\delta_{m,f}-\delta_{m,i}}\cdot\frac{\left(\delta_m^2-\delta_{m,i}^2\right)}{1+\beta^2} + \right.$$

$$\left. - \frac{\delta_{\mathrm{m,i}}\cdot\left(\delta_{m,f}-\overline{\delta_m}\right)}{\left(\delta_{m,f}-\delta_{m,i}\right)\overline{\delta_m}}\cdot E_0\cdot\frac{\delta_m^2}{2\left(1+\beta^2\right)}\right] +$$

$$+\frac{\beta^2}{1+\beta^2}\cdot\left[\frac{E_0}{2}\cdot\frac{\beta^2\cdot\delta_{\mathrm{m,i}}^2}{1+\beta^2} + \frac{E_0\cdot\delta_{\mathrm{m,i}}\cdot\delta_{m,f}}{\delta_{m,f}-\delta_{m,i}}\cdot\frac{\beta}{\sqrt{1+\beta^2}}\cdot\left(\delta_m-\delta_{m,i}\right) - \frac{1}{2}\frac{E_0\cdot\delta_{\mathrm{m,i}}}{\delta_{m,f}-\delta_{m,i}}\cdot\frac{\beta^2}{1+\beta^2}\cdot\left(\delta_m^2-\delta_{m,i}^2\right) + \right.$$

$$\left. - \frac{\delta_{\mathrm{m,i}}\cdot\left(\delta_{m,f}-\overline{\delta_m}\right)}{\left(\delta_{m,f}-\delta_{m,i}\right)\overline{\delta_m}}\cdot E_0\cdot\frac{\beta^2}{1+\beta^2}\cdot\frac{\delta_m^2}{2}\right]$$

$$= \frac{1}{1+\beta^2}\cdot\left[\frac{E_0\cdot\delta_{m,i}^2}{2\left(1+\beta^2\right)}\cdot\left(1+\beta^4\right) + \frac{E_0\cdot\delta_{\mathrm{m,i}}\cdot\delta_{m,f}}{\delta_{m,f}-\delta_{m,i}}\cdot\frac{\left(\delta_m-\delta_{m,i}\right)}{\sqrt{1+\beta^2}}\cdot\left(1+\beta^3\right) - \frac{1}{2}\frac{E_0\cdot\delta_{\mathrm{m,i}}}{\delta_{m,f}-\delta_{m,i}}\cdot\frac{\left(\delta_m^2-\delta_{m,i}^2\right)}{1+\beta^2}\cdot\left(1+\beta^4\right) + \right.$$

$$\left. - \frac{\delta_{\mathrm{m,i}}\cdot\left(\delta_{m,f}-\overline{\delta_m}\right)}{\left(\delta_{m,f}-\delta_{m,i}\right)\overline{\delta_m}}\cdot E_0\cdot\frac{\delta_m^2}{2\left(1+\beta^2\right)}\cdot\left(1+\beta^4\right)\right] \tag{5.36}$$

The Mode mixity $\mu = \frac{G_{II}}{G_{tot}}$ as a function of β is written as:

$$\mu(\delta_m) \mid_{\beta} = \frac{G_{II}}{G_{tot}}$$

$$= \frac{\frac{\beta^2}{1+\beta^2} \cdot \left[\frac{E_0}{2} \cdot \frac{\beta^2 \cdot \delta_{\mathrm{m,i}}^2}{1+\beta^2} + \frac{E_0 \cdot \delta_{\mathrm{m,i}} \cdot \delta_{m,f}}{\delta_{m,f} - \delta_{m,i}} \cdot \frac{\beta}{\sqrt{1+\beta^2}} \cdot (\delta_m - \delta_{m,i}) - \frac{1}{2} \frac{E_0 \cdot \delta_{\mathrm{m,i}}}{\delta_{m,f} - \delta_{m,i}} \cdot \frac{\beta^2}{1+\beta^2} \cdot \left(\delta_m^2 - \delta_{m,i}^2 \right) - \frac{\delta_{\mathrm{m,i}} \cdot \left(\delta_{m,f} - \overline{\delta_m} \right)}{(\delta_{m,f} - \delta_{m,i}) \overline{\delta_m}} \cdot E_0 \cdot \frac{\beta^2}{1+\beta^2} \cdot \frac{\delta_m^2}{2} \right]}{\frac{1}{1+\beta^2} \cdot \left[\frac{E_0 \cdot \delta_{m,i}^2}{2(1+\beta^2)} \cdot (1+\beta^4) + \frac{E_0 \cdot \delta_{\mathrm{m,i}} \cdot \delta_{m,f}}{\delta_{m,f} - \delta_{m,i}} \cdot \frac{(\delta_m - \delta_{m,i})}{\sqrt{1+\beta^2}} \cdot (1+\beta^3) - \frac{1}{2} \frac{E_0 \cdot \delta_{\mathrm{m,i}}}{\delta_{m,f} - \delta_{m,i}} \cdot \frac{\left(\delta_m^2 - \delta_{m,i}^2 \right)}{1+\beta^2} \cdot (1+\beta^4) - \frac{\delta_{\mathrm{m,i}} \cdot \left(\delta_{m,f} - \overline{\delta_m} \right)}{(\delta_{m,f} - \delta_{m,i}) \overline{\delta_m}} \cdot E_0 \cdot \frac{\delta_m^2}{2(1+\beta^2)} \cdot (1+\beta^4) \right]} \tag{5.37}$$

For the μ calculated in Case 1 and Case 2 (see 5.3.1.1) the limits for $\beta \to 0$ and $\beta \to \infty$ are the same:

$$\begin{cases} \lim_{\beta \to 0} \mu = 0 \\ \lim_{\beta \to \infty} \mu = 1 \end{cases} \tag{5.38}$$

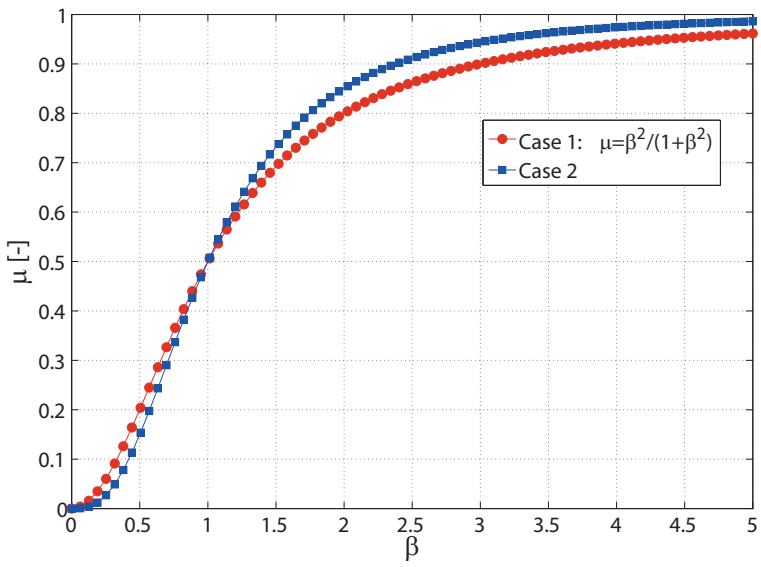

Figure 5.8: Evolution of $\mu\,(\beta)$, comparison between equations 5.22 and 5.37

Although equation 5.37 is a function of δ_m and β, it is found to be weakly dependent on δ_m. This means that energy mode mixity μ does not vary much during loading at a constant displacement mode mixity β. For this reason, it is possible to calculate μ at $\delta_m = \delta_f$ without committing an important error.

Figure 5.8 shows the relationship between μ and β calculated by equations 5.22 and 5.37 for $\delta_m = \delta_f$. The value $\mu(0) = 0$ represents the pure Mode I while $\mu(\beta \to +\infty) = 1$ the pure Mode II. The small mismatch between the two curves is due to the different approach, since the formula proposed in [98] computes the decoupled mode mixity starting from the energies in Mode I and Mode II while in the other case the integrals are performed at all intermediate openings $\overline{\delta}_m$, using the mixed mode displacements and stress norms δ_m and σ_m . The difference, however, is relatively small and, as shown in equations 5.38, the limits for $\beta \to 0$ and $\beta \to \infty$ are the same. For this reasons, the formula proposed by Camanho is used in this work to correlate μ and β whenever applicable. It should be reminded here that those formulas can be considered valid under the assumption of self-similar displacement field and uniform displacement mode mixity β in the process zone.

This approach could be extended to take into account bridging by considering piece-wise non linear traction separation relationships in the integrals. However due to the complexity of those computations and the limitations of the methods, this calculation is not performed here.

Figure 5.9 shows the cohesive laws corresponding to the pure modes and the intermediate ones

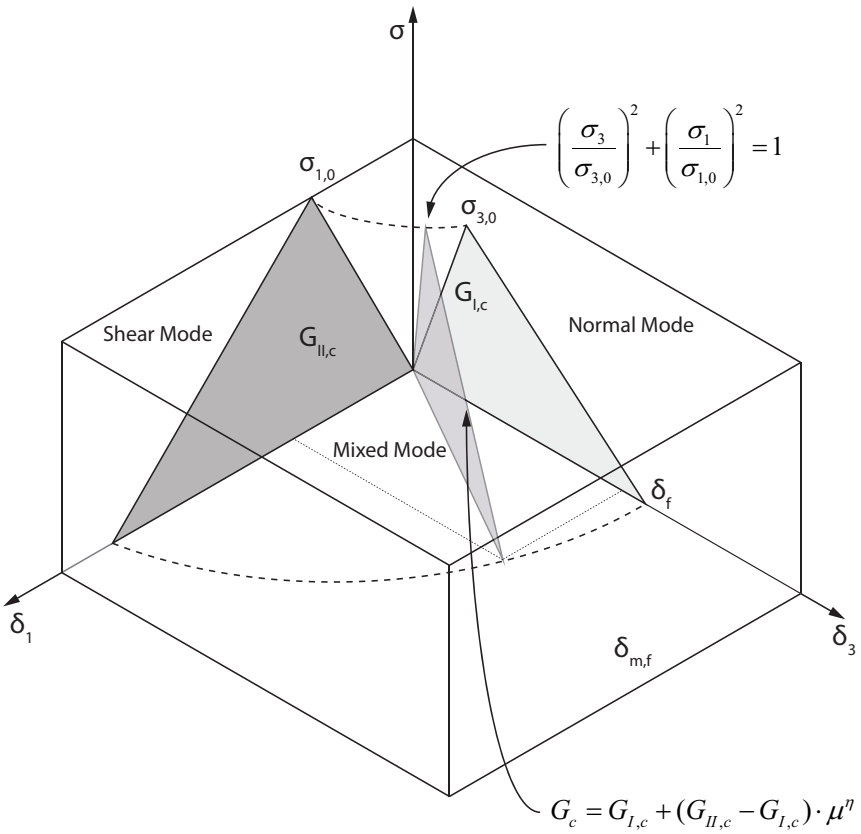

Figure 5.9: Schematic cohesive law for Mixed Mode conditions

for Mixed Mode conditions. It points out how δ_f and $\sigma_{m,i}$ vary if the ratio of the displacements β changes. The energy at crack initiation G_c in Mixed Mode is defined by the B-K relationship (equation 2.2).

5.3.2 Cohesive law in Mixed Mode

In order to obtain a unique cohesive law able to predict the delamination behavior for whatever mode mixity, we need a model describing the evolution of the bridging tractions σ_b as a function of both opening δ_m and displacement mode mixity β. The model can be generically described by a tabular function $D(\delta_m, \beta)$ in which the damage evolution is computed by interpolation over a grid of prescribed points $D_{i,j}(\delta_i, \beta_j)$. This model can also be seen as a collection of cohesive laws corresponding to constant β values. All the next Figures are defined up to $\beta_{max} = 5$ which represents the most meaningful part while the numerical simulations are performed with $\beta_{max} = 20$ which improves the accuracy of the final result.

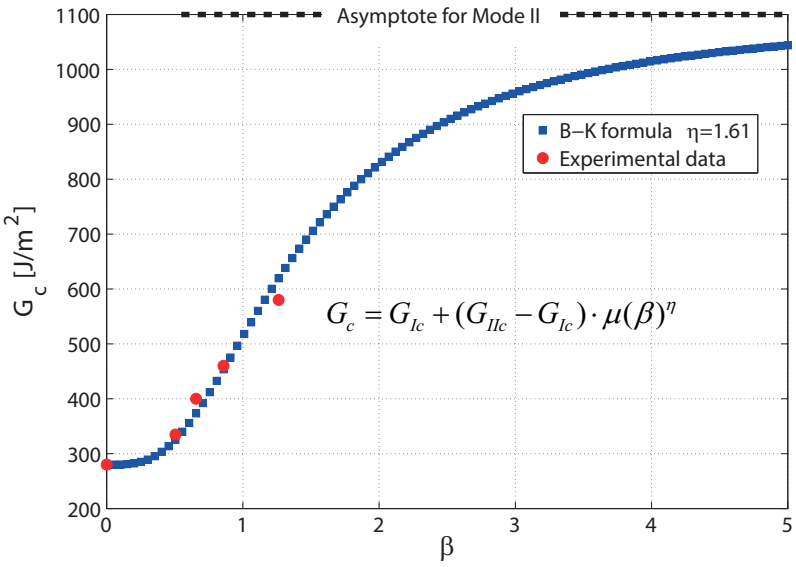

Figure 5.10: Critical ERR at initiation as a function of β

The cohesive law is composed by the first triangle which represents the ERR at initiation and a second tail to simulate the bridging tractions. The experimental data, discussed in Chapter 4, provide the G_c values at fracture initiation for pure Mode I, Mode II and for the intermediate mode mixities. The data are fitted with the B-K formula (equation 2.2) using as parameter the displacement mode mixity β with an the exponent $\eta = 1.61$. Figure 5.10 shows the experimental G_c as a function of $\beta(\mu)$ and the fitting function. The energy in pure Mode II is not plotted since it corresponds to $\beta \to \infty$.

Once $G_c(\beta)$ is set, the critical load at damage initiation must be defined as a function of β, as obtained in equation 5.17. Figure 5.11 shows the trend of $\sigma_{m,i}(\beta)$, which changes between $20MPa$ for $\beta = 0$ (pure Mode I) and $38MPa$ for $\beta \to \infty$ (pure Mode II).

The contribution of bridging can be added by defining the corresponding parameters as a function of β. The parameters, shown in Figure 5.12, are:

- $\sigma_{max}(\beta)$: maximum bridging stress
- $G_b(\beta) = \int_0^{\delta_{max}} \sigma_m(\delta) d\delta_m \mid_\beta$: energy provided by bridging tractions
- $\delta_f(\beta) = \sqrt{\delta_3^2 + \delta_1^2}$: ultimate opening.

In this case two different zones can be identified: a first process zone represents the cracked matrix region while the bridging zone implies the presence of bridging fibres.

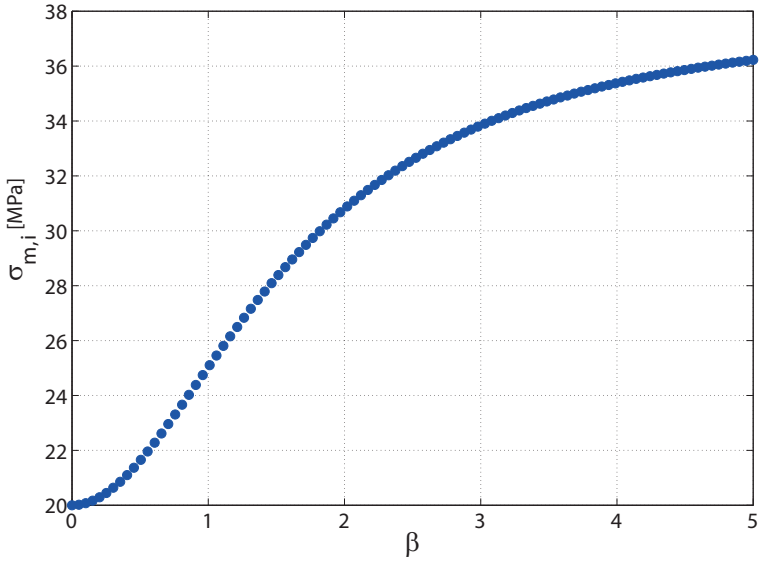

Figure 5.11: Mixed Mode stress at damage initiation $\sigma_{m,i}$ as function of β

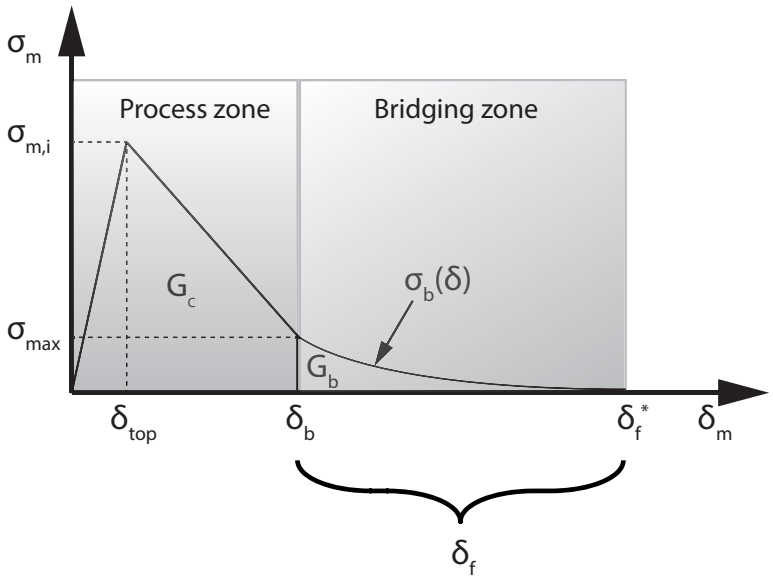

Figure 5.12: Cohesive law for a constant β value: definition of the bridging parameters

The shape of the functions $\sigma_{max}(\beta)$, $G_b(\beta)$ and $\delta_f(\beta)$ is initially unknown. Looking at the trend of G_b obtained by the experimental results (see Figure 4.46), it is evident that the bridging contribution shows a quick drop between Mode I and 30% Mixed Mode and than decreases slower as the mode mixity increases. Thus, the functions $\sigma_{max}(\beta)$ and $\delta_f(\beta)$ are supposed to be monotonically decreasing. According to these considerations, three different functions are defined by equations 5.39, 5.40, 5.41 and shown in Figure 5.39 5.40 5.41 respectively.

$$G_b(\beta) = \begin{cases} G_b(\beta) = G_{b,30} + (G_{b,ModeI} - G_{b,30}) \cdot \left(1 - \frac{\beta}{\beta_{b,30}}\right) \cdot e^{\left(\xi_{G_b} \cdot \beta\right)} & 0 < \beta < \beta_{b,30} \\ G_b(\beta) = G_{b,30} \cdot \left(1 - \frac{\beta}{\beta_{b,end}}\right) \cdot e^{\left(-\xi_{G_b} \cdot \beta\right)} & \beta_{b,30} < \beta < \beta_{b,end} \end{cases} \tag{5.39}$$

$$\sigma_{max}(\beta) = \sigma_{max,ModeI} \cdot \left(1 - \frac{\beta}{\beta_{b,end}}\right) \cdot e^{\left(\xi_{\sigma_{max}} \cdot \beta\right)} \tag{5.40}$$

$$\delta_f(\beta) = \delta_{f,ModeI} \cdot \left(1 - \frac{\beta}{\beta_{b,end}}\right) \cdot e^{\left(\xi_{\delta_f} \cdot \beta\right)} \tag{5.41}$$

where:

- $G_{b,ModeI}$: bridging energy contribution for pure Mode I test
- $G_{b,30}$: bridging energy contribution for 30% Mixed Mode test
- $\sigma_{max,ModeI}$: maximum stress provided by the bridging tractions in Mode I test (see Tab 5.1)
- $\delta_{f,ModeI} = \delta(z_{max})$ maximum COD for bridging tractions in Mode I test (see Tab 5.1)

and ξ_i are the bridging parameters which will be obtained by the optimization process:

- ξ_{G_b} : bridging parameter describing the evolution of G_b as a function of β
- $\xi_{\sigma_{max}}$: bridging parameter describing the evolution of σ_{max} as a function of β
- ξ_{δ_f} : bridging parameter describing the evolution of δ_f as a function of β

The definitions of $\beta_{b,30}$ and $\beta_{b,end}$ are explained in section 5.3.6 since they derives from the numerical results.

By assuming a decreasing trend for the three bridging parameters $G_b, \sigma_{max}, \delta_f$, a preliminary mode-dependent cohesive law is shown in Figure 5.16. The stresses are tabulated as a function

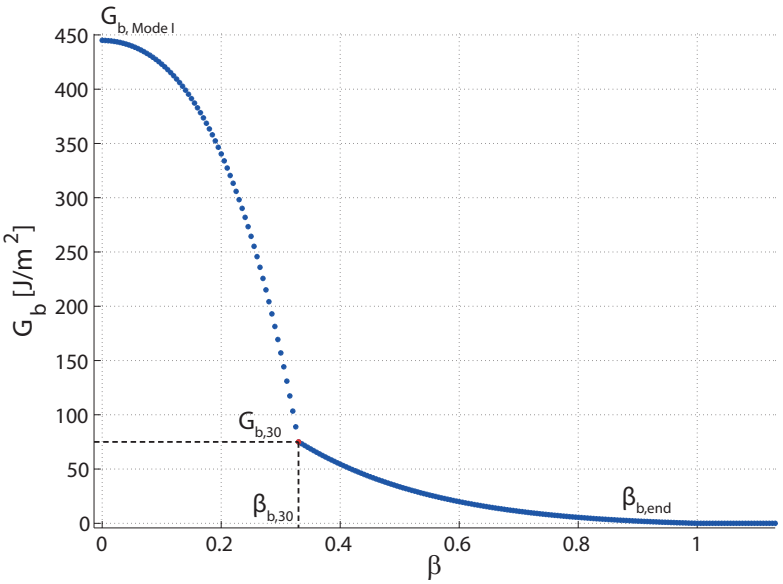

Figure 5.13: Evolution of $G_b(\beta)$ as a function of β by equation 5.39

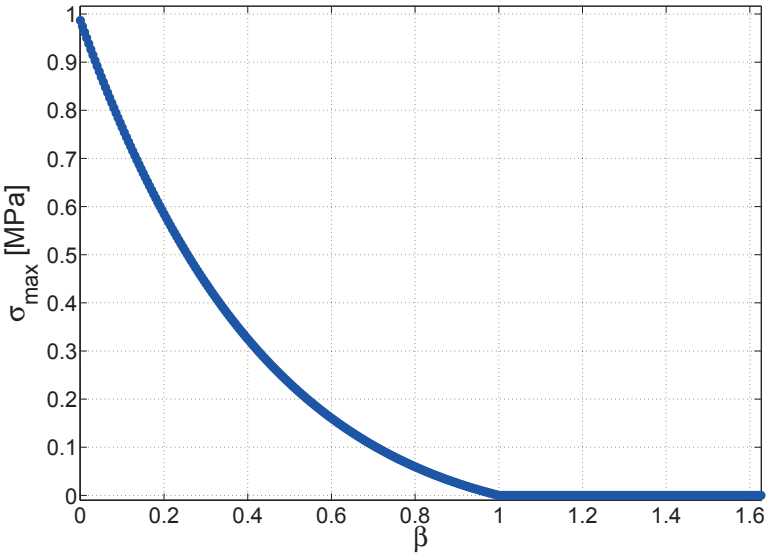

Figure 5.14: Evolution of $\sigma_{max}(\beta)$ as a function of β by equation 5.40

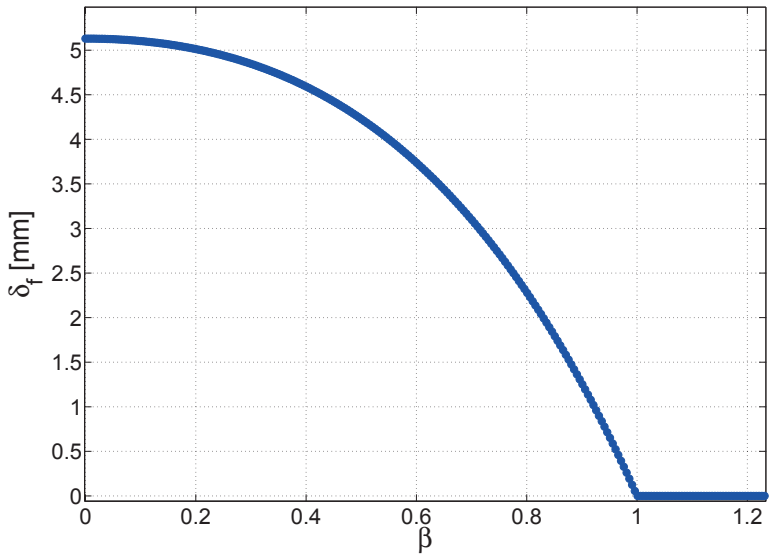

Figure 5.15: Evolution of $\delta_f(\beta)$ as a function of β by equation 5.41

of δ_m and β. The curve for $\beta = 0$ corresponds to the cohesive law in pure Mode I, where the relevant amount of bridging generates a long tail for high opening values δ_m. As β grows, the contribution of bridging decreases until the tail disappears. The remaining curves represent the linear decay of the stress without any toughening process. In the next sections, the optimization process and the choice of the bridging functions, to define the corresponding parameters, are discussed.

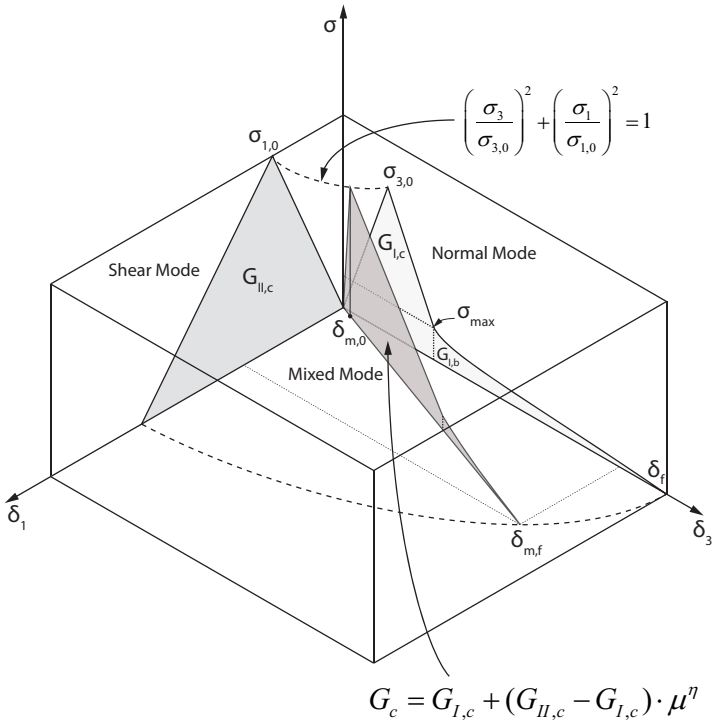

Figure 5.16: 3D cohesive law as a function of β

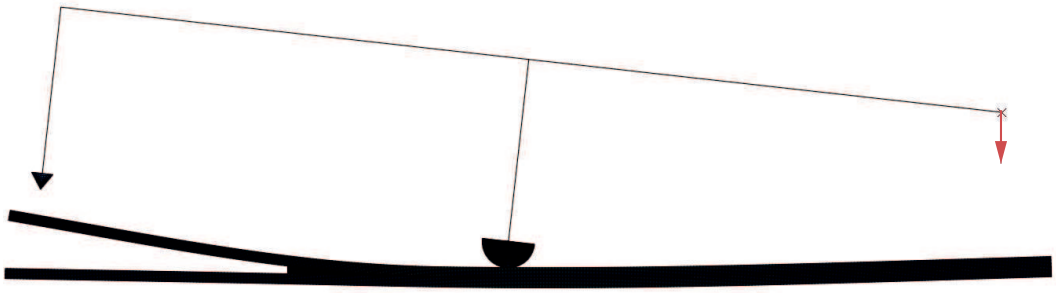

Figure 5.17: FE Model for Mixed Mode delamination

5.3.3 FE Model for Mixed Mode delamination

Figure 5.17 shows the FE Model designed for simulating the Mixed Mode delamination process. The specimen and the MMB jig are meshed with quadratic elements CPE8R with an average size of $0.2mm$. Cohesive elements are placed on the delamination plane and the nodes are collapsed in order to obtain a zero-thickness layer. In order to improve the convergence, the cohesive elements mesh size is set to $0.04mm$, which implies having five cohesive elements for each element belonging to the specimen. A surface-to-surface contact simulates the interaction between the central pin and the specimen, without any friction contribution.

Since a static time integration step showed convergence issues during crack propagation, a implicit dynamic analysis is used. This allows to overcome small instabilities which may occur during the damaging of the cohesive elements. In order to avoid any influence due to the mass of the system, the density is set 100 times lower than the real one. If the mass is kept low, no differences are present between using the *Transient Fidelity*, *Moderate Dissipation* or *Quasi-Static* time integration method.

The displacement, highlighted by the arrow, is applied at the end of the upper bar.

Abaqus® allows to use a mode dependent approach by using an internal cohesive model formulation or providing a tabular form to describe the mixed mode damage evolution $D(\delta_m, \beta)$. In the following subsections 5.3.3.1 and 5.3.3.2 both approaches are explained and discussed.

5.3.3.1 Abaqus® internal model based on B-K relationship

The internal cohesive model formulation is based on the B-K relationship for mode mixity combined with a bilinear traction separation model, which implies the fracture behavior only depends on the critical energies $G_c(\beta)$ without any bridging contribution. The computed cohesive law is defined by:

- the initial elastic stiffness E_0 of the element

- the ultimate stress $\sigma_{3,0}$ and $\sigma_{1,0}$ for pure Mode I, II
- the critical energies $G_{I,c}$ and $G_{II,c}$
- the exponent η of the B-K formula which fits the critical energies over different mode mixities.

By filling these values, the solver automatically computes the local mode mixity for each cohesive element based on β. However, by using this internal formulation, any bridging effects are not taken into account.

5.3.3.2 Cohesive law in tabulated form

In order to take into account the bridging effects, a tabulated form of the cohesive law is used and filled in the Abaqus® code. To tabulate the cohesive law in mode dependent, Abaqus® requires the magnitude of the crack opening displacement δ_m, the corresponding damage parameter D and displacement mode mixity computed as $\frac{2}{\pi}\arctan(\beta)$. The cohesive law is linearly discretized by using 300 points along the δ_m axis and 400 points along the β axis over a range of 0 to 20. To calculate the fracture initiation, $\sigma_{3,0}$ and $\sigma_{1,0}$ are also required for the pure Modes I, II.

5.3.4 External and local mode mixity

A preliminary simulation of the 40% Mixed Mode delamination with a MMB setting is performed by a tabulated form of the mode-dependent cohesive law with bridging tractions. The corresponding bridging parameters are chosen as an initial guess. This allows to better understand how the mode mixity β is related to the external mode mixity μ, applied by imposing the C-arm length as discussed in section 3.1.2, for a MMB setting.

Figure 5.18 shows the evolution of β for the first six cohesive elements and the damage parameter D correspondent to the element 1, as a function of the COD $\delta_m = \sqrt{\delta_3^2 + \delta_1^2}$. The β value continuously varies as the damage parameter increases, meaning that the local mode mixity in the damaged region is not constant. As the cohesive element is damaged, the local mode mixity changes and, therefore, also the corresponding cohesive law.

It is very important to note that the local mode mixity β of all elements converge to a common asymptotic value ~ 0.4 which is significantly different from the value of $\beta = 0.8$ expected from the $\mu(\beta) = \frac{\beta^2}{1+\beta^2}$ relationship (see Figure 5.8). Indeed, if this relationship was true, $\beta = 0.4$ would correspond to a much lower mode mixity of $\mu(0.4) \backsimeq 14\%$.

The fact that at damage initiation the β value is very close to the one supposed by the relationship $\mu(\beta)$ has no actually meaning. A mode mixity represents the ratio between released energies, thus it is meaningful in the damaged region when the crack propagates or at $\delta = \delta_f$.

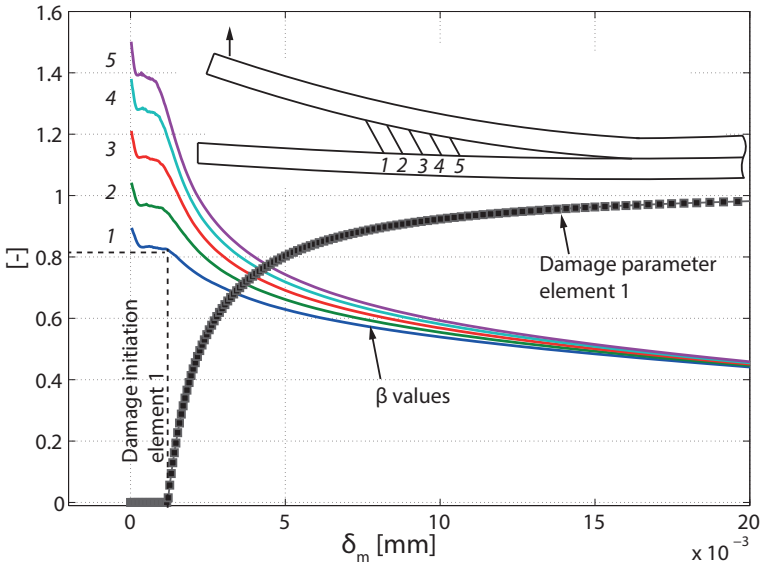

Figure 5.18: β curves associated to the first six cohesive elements as a function of the COD $\delta_m = \sqrt{\delta_3^2 + \delta_1^2}$ for a 40% Mixed Mode FE Model

The relationship $\mu(\beta) = \frac{\beta^2}{1+\beta^2}$ by Camanho was derived by assuming a constant β during the damage evolution and thus is clearly inapplicable to the present case. Indeed, due to the non uniform distribution of β in the process zone, each element follows a different damage evolution path. Thus the energy dissipated in the process zone in normal and shear directions become complex integral of space and time varying terms.

The same evolution of β in the process zone is also found by using a mode-dependent cohesive law based on the B-K relationship without any bridging tractions. This proves that the non-constant β value is caused by the kinematic of the MMB setting and is not due to the presence of bridging tractions which may affect the local stresses in the damage region.

Figure 5.19 shows the evolution of β and D for the first cohesive element with respect to the applied displacement, in order to correlate the damage initiation to the applied displacement. According to the experimental load-displacement and crack length-displacement curves shown in Chapter 4, Figures 4.27 and 4.28, the crack propagation starts at an applied displacement of $\backsimeq 7.5mm$ while the first cohesive element has a damage initiation at $\backsim 1.5mm$. This better explains why the β value at damage initiation cannot be taken as reference for a global mode mixity.

Based on these results, the numerical model cohesive formulation used in Abaqus® and described in sections 5.3.1 and 5.3.1.1, which correlates the local mode mixity in terms of $\beta = \frac{\delta_1}{\delta_3}$

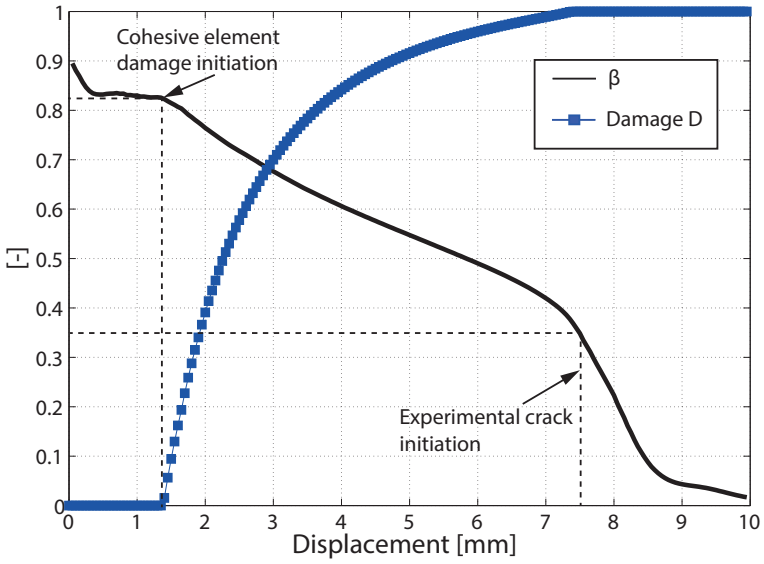

Figure 5.19: β curve associated to the first cohesive element as a function of the applied displacement for a 40% Mixed Mode FE Model

to the one calculated in terms of energies $\mu(\beta) = \frac{G_{II}}{G_{tot}} = \frac{\beta^2}{1+\beta^2}$, is not valid to simulate a MMB test both with and without bridging tractions. The correlation $\mu(\beta)$ is actually verified only if β is kept constant during the delamination process. If β varies in the damaged part, the model is not able to properly represent the external mode mixity μ with the local one.

5.3.5 Bridging modeling

Looking at the Figure 5.20, at damage initiation the β value is relatively high (0.8) and thus the cohesive traction will develop according to a mixed mode cohesive law corresponding to $\mu = 40\%$. In the matrix cracking process zone, the local mode mixity β decreases up to ~ 0.4 (that would correspond to $\mu(0.4) \backsimeq 14\%$) at the end of the matrix cracking process zone when the damage parameter D is ~ 0.99. This will then trigger the development of significant bridging tractions as the local mode mixity becomes lower than the mode mixity threshold for bridging development. In the fiber bridging zone, the local mode mixity decreases even further, which leads towards an even more intense fiber bridging development similar to Mode I. This process goes clearly against the experimental observations in which tests at $\mu = 40\%$ did not show significant bridging fibers in the wake of the crack as well as a very small R-curve effect. This evolution is thus clearly an artifact of the cohesive modeling. Physically, the observed behavior in the model would correspond to the generation of new bridging fibers far from the crack tip,

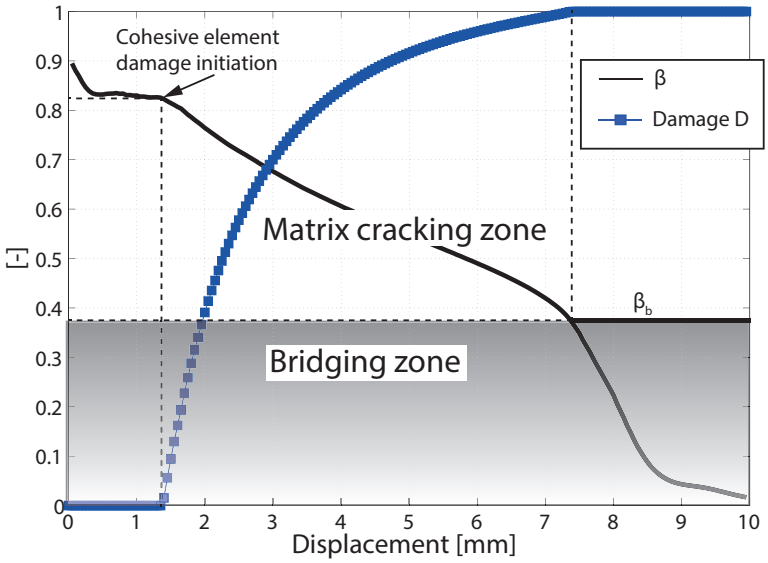

Figure 5.20: β curve associated to the first cohesive element as a function of the applied displacement for a 40% Mixed Mode FE Model

which appears as very unrealistic based on the observation.

To summarize, two main issues have been found when implementing bridging tractions with a direct dependence on the local mode mixity β:

1. the β value in the matrix cracking process zone evolves towards lower values, which invalidates the use of the relationship linking the global energy mode mixity μ to the local displacement mode mixity measure β. The experiments are always performed with a controlled μ, but unfortunately, when looking at the local damage evolution problem, this single energy mode mixity will not correspond to a single value of β, but to a range of values. This means that we cannot directly translate identified bridging tractions at a given mode mixity μ to a given cohesive law for a corresponding β. Instead, a full mixed mode cohesive model is necessary to simulate a test, even when the mode mixity μ remains constant.

2. the local mode mixity β drops significantly in the matrix cracking process zone and decreases even faster in the fiber bridging region, leading to an artificial increase of bridging tractions far from the crack tip.

Phenomenologically, it is observed that the bridging fibers are mostly generated in the matrix cracking process zone and then will evolve independently of the crack tip fracture mechanisms

afterwards. The initial bridging fiber density which controls the intensity of the fiber bridging tractions is thus expected to depend mostly on the mode mixity in the matrix cracking process zone and not so much by the mode mixity evolution in the fiber bridging zone. According to this reasoning, the initial fiber density, and thus bridging traction intensity, would be controlled by the local mode mixity $\beta = \beta_b$ reached at the end of the matrix cracking process zone. The mode mixity at fiber bridging initiation β_b thus indirectly represents the initial bridging fiber density and can be used as a constant state variable controlling the evolution of bridging tractions in the bridging zone instead of the local mode mixity measure β.

This approach can be implemented by using a custom mode mixity measure β^* to implement our cohesive laws. The value of β^* is set equal to the local displacement mode mixity β in the matrix cracking region, leading to a similar behavior to classical linear B-K cohesive models. Though, at the critical damage corresponding to fiber bridging initiation, the value of β^* is then frozen to its current value as $\beta_b = \beta^*$and will remain constant in the bridging zone. As a matter of fact, the bridging tractions will then further develop according to a single "mode mixity" β_b thus avoiding the artifact observed previously.

In order to overcome this numerical artifact, an external Fortran® USDFLD sub-routine is coded to implement the proposed alternative method for the evolution of the local mode mixity indicator β^* in the process zone. This routine, schematically shown in Figure 5.22, is called at the beginning of each step for each integration point in the cohesive zone and it computes the following variables:

- local mode mixity $\beta = {}^{\delta_1}/_{\delta_3}$
- current damage $D = 1 - {}^{E}/_{E_0}$
- critical damage D corresponding to the beginning of fiber bridging $D_{tab}(\beta) = D(\delta_b, \beta)$
- mode mixity indicator β^*: if $D \leqslant D_{tab}(\beta)$: $\beta^* = \beta$ else β^* is kept constant to its previous value

As damage D can only increase, this ensures that β^* is constant in the bridging zone and can be called β_b. The function $D_{tab}(\beta)$ combines the $D_{\sigma_{max,b}}$ values, which corresponds to the damage at bridging initiation as a function of β, as shown in Figure 5.21.

Similarly to the tabular mixed-mode cohesive model $D = D(\delta_m, \beta)$ presented previously, a tabular cohesive model $D(\beta) = D(\delta_b, \beta^*)$ is implemented in Abaqus® which uses the mode mixity indicator β^* instead of the local mode mixity β calculated internally.

Figure 5.23 shows the evolution of β^* versus the applied displacement by using the external routine for the 40% Mixed Mode model. After the condition $D(\beta^*) > D_{tab}(\beta^*)$ is verified,

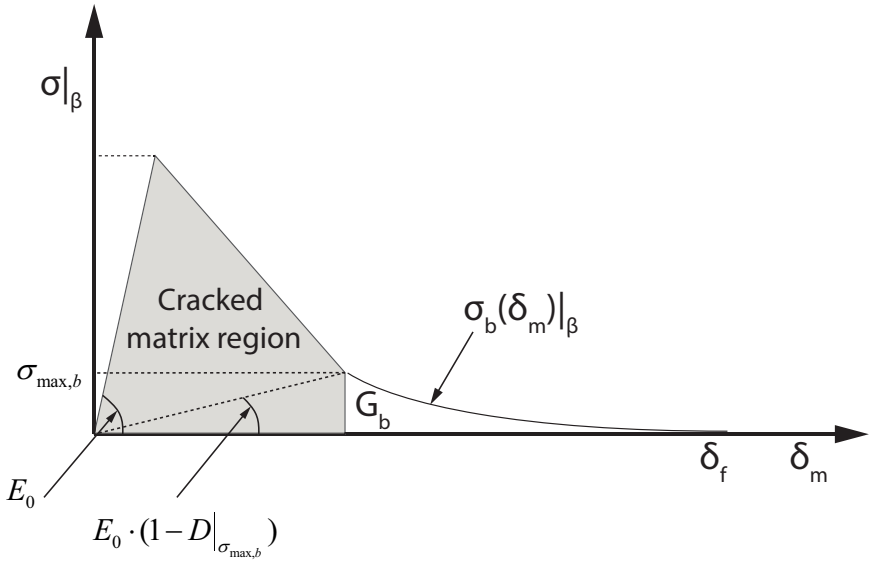

Figure 5.21: Definition of $D\,|_{\sigma_{max,b}}$ at a constant β

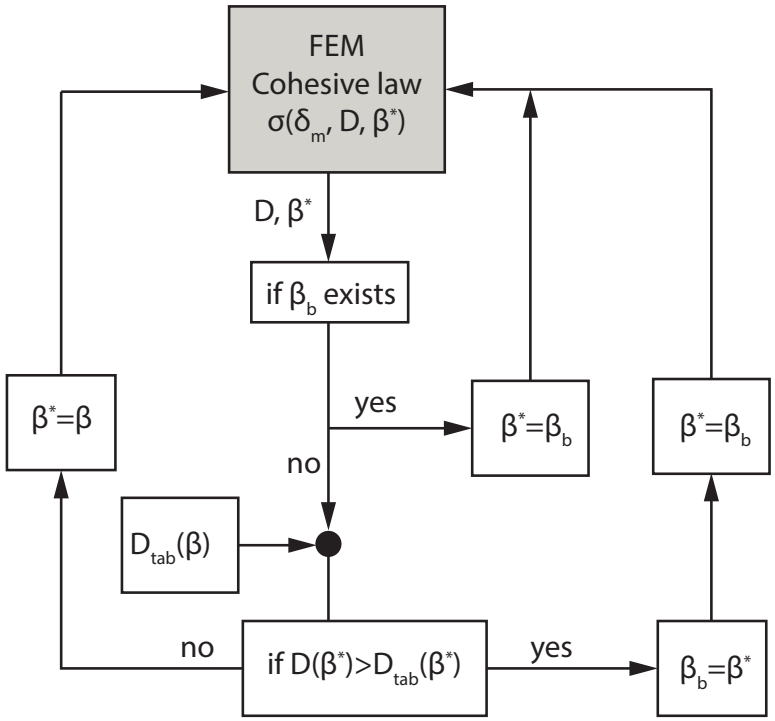

Figure 5.22: Fortran® sub-routine called by Abaqus® to control the evolution of β^*

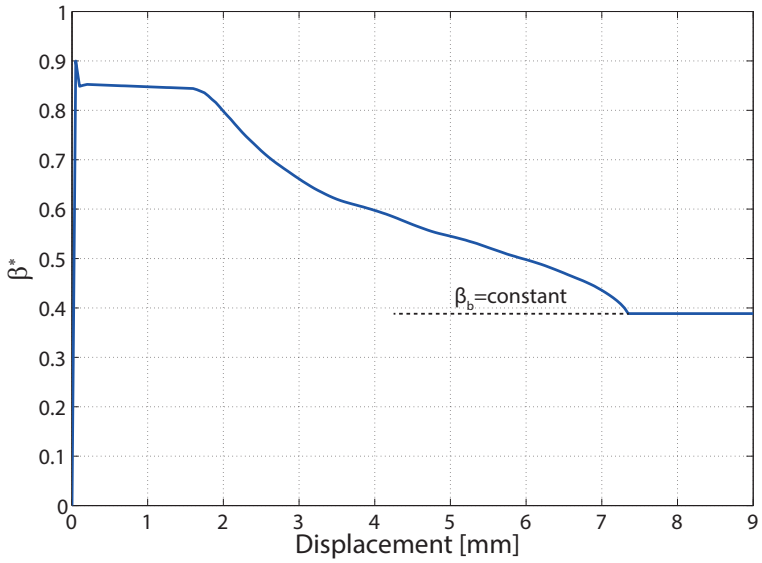

Figure 5.23: Evolution of β^* versus applied displacement by using the external routine for a 40% Mixed Mode model

μ [%]	20	30	40	60
β_b	0.25	0.33	0.38	0.6

Table 5.2: β_b values obtained by the FE Model

β^* is kept constant and called β_b. This algorithm is based on the assumption that bridging characteristics depend on the stress field in the cracked matrix region (see Figure 5.21), which corresponds to the first part of the cohesive law. By running several simulations for the 20%, 30%, 40% and 60% Mode Mixity is found out that β_b only depends on the mode mixity applied by the MMB setting and is weakly influenced by the bridging parameters ξ_{G_b},$\xi_{\sigma_{max}}$ and ξ_{δ_f}.

The β_b values are computed for all the cohesive elements involved in the delamination process. It is found out that they all approximately converge to the same β_b, which means that the bridging contribution associated to each element is the same, as shown in Figure 5.24 for $\mu = 40\%$ .The table 5.2 resumes the β_b values obtained by the numerical simulations for different applied mode mixities.

5.3.6 Optimization process for bridging parameters

The bridging parameters to be optimized, defined in section 5.3.2, are $\xi_i = \left[\xi_{G_b}, \xi_{\sigma_{max}}, \xi_{\delta_f}\right]$ plus $\beta_{b,30}$ and $\beta_{b,end}$.

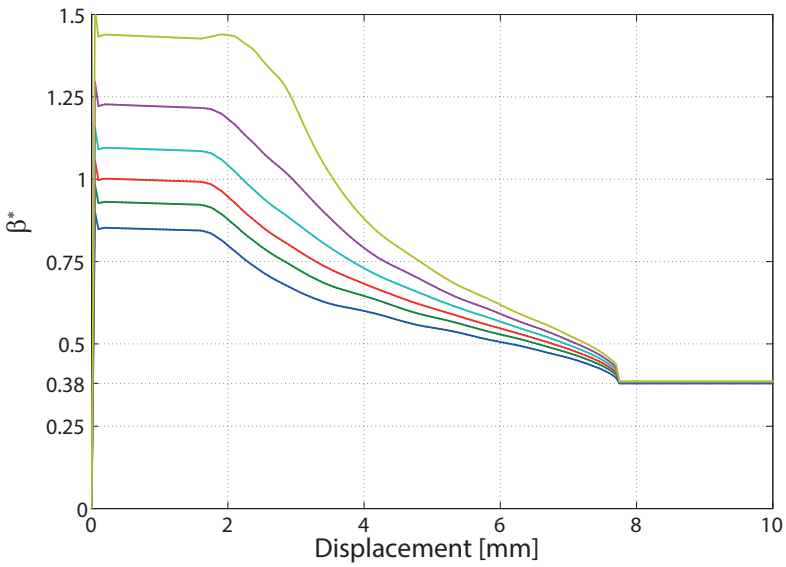

Figure 5.24: Evolution of β for six different cohesive elements versus applied displacement by using the external routine for a 40% Mixed Mode model

The 30% Mixed Mode delamination test represents the threshold between the large scale bridging, which occurs in Mode I and 20% Mixed Mode, and the second part in which a lower bridging contribution is found. For this reason, the first parameter to set is the mode mixity threshold $\beta_{b,30}$, which comes from the constant β^* value, associated to the 30% Mixed Mode FE model. The low contribution of bridging for $\mu = 30\%$ makes the $\beta_{b,30}$ value almost independent of the ξ_i parameters. For this reason, $\beta_{b,30}$ can be easily obtained by running a simulation with a preliminary ξ_i set of bridging parameters. The simulation result provides $\beta_{b,30} = 0.33$ (see table 5.2).

The mode mixity $\mu = 60\%$, according to the experimental results, shows that the amount of bridging is very low. This fact makes the influence of $\beta_{b,end}$ quite low and it can be estimated by the value defined in Table 5.2. Since a small amount of bridging is still present, $\beta_{b,end} = 0.7$ is initially supposed.

The next step consists in the definition of the optimization algorithm to obtain the bridging parameters $\xi_i = \left[\xi_{G_b}, \xi_{\sigma_{max}}, \xi_{\delta_f}\right]$. The mode mixity which is most affected by bridging is $\mu = 20\%$. For this reason the optimization process is run by using a 20% Mixed Mode FE Model which allows a better accuracy for the bridging parameters definition. If the optimization process was run for $\mu = 60\%$, the negligible amount of bridging would make the final results unreliable since the FBG strains would be weakly affected by any ξ_i variation.

The experimental strains evolution $\varepsilon_i(t)$ $i = 1 : 10$ obtained by the ten FBG sensors embedded are used as objective data for optimization. Since for $\mu = 20\%$ a clear steady state is not reached during the experiment, a self-similar crack propagation cannot be assumed and the approach used for the Mode I optimization is not allowed. The optimization process is performed by fitting the *strain* curves, one for each FBG sensor, all along the applied displacement (shown in Chapter 4, Figure 4.16), which allows to detect the evolution of bridging over the whole delamination test. The objective function used for the identification in Mixed Mode is obtained from the general one defined in Equation 5.1 is thus defined as:

$$F(t) = \frac{1}{2} \cdot \sum_{i=1}^{10} \| \frac{\varepsilon_{i,FEM}(t) - \varepsilon_{i,FBGs}(t)}{\varepsilon_{i,FBGs}(t)} \|^2 \tag{5.42}$$

where t indicates the time.

Figure 5.25 shows the optimization scheme used to define the bridging parameters $\xi_i = \left[\xi_{G_b}, \xi_{\sigma_{max}}, \xi_{\delta_f}\right]$. Note that the FE model used in the present identification simulates the whole crack propagation using cohesive elements and thus takes significantly more time to solve than the quasi-static model used for Mode I identification.

The evolution of the bridging parameters ξ_i during the optimization process is shown in Figure 5.26. Before starting the optimization, a set of parameters close to the optimum solution is chosen. After a first part in which mainly ξ_{G_b} and $\xi_{\sigma_{max}}$ vary, the optimization scheme is able to reduce the difference with the objective function and to reach the minimum of the function $F(\overline{x})$. Table 5.3 shows the final optimized bridging parameters $\xi_i = \left[\xi_{G_b}, \xi_{\sigma_{max}}, \xi_{\delta_f}\right]$.

Optimized bridging parameters	ξ_{δ_f}	$\xi_{\sigma_{max}}$	ξ_{G_b}
[-]	1.23	-4.36	3.95

Table 5.3: Bridging parameters $\xi_i = \left[\xi_{G_b}, \xi_{\sigma_{max}}, \xi_{\delta_f}\right]$ obtained from the optimization process

Figure 5.27(a) shows the comparison between the strains measured by the ten FBGs, which represent the objective function, and the ones calculated by the FE Model by using the global cohesive law with mode dependent approach. The fitting of the objective function is very accurate for both the steep region, which indicates the crack tip, and the one affected by the bridging tractions. Figure 5.27(b) shows the same results but only for 3 FBG sensors in order to make them more understandable.

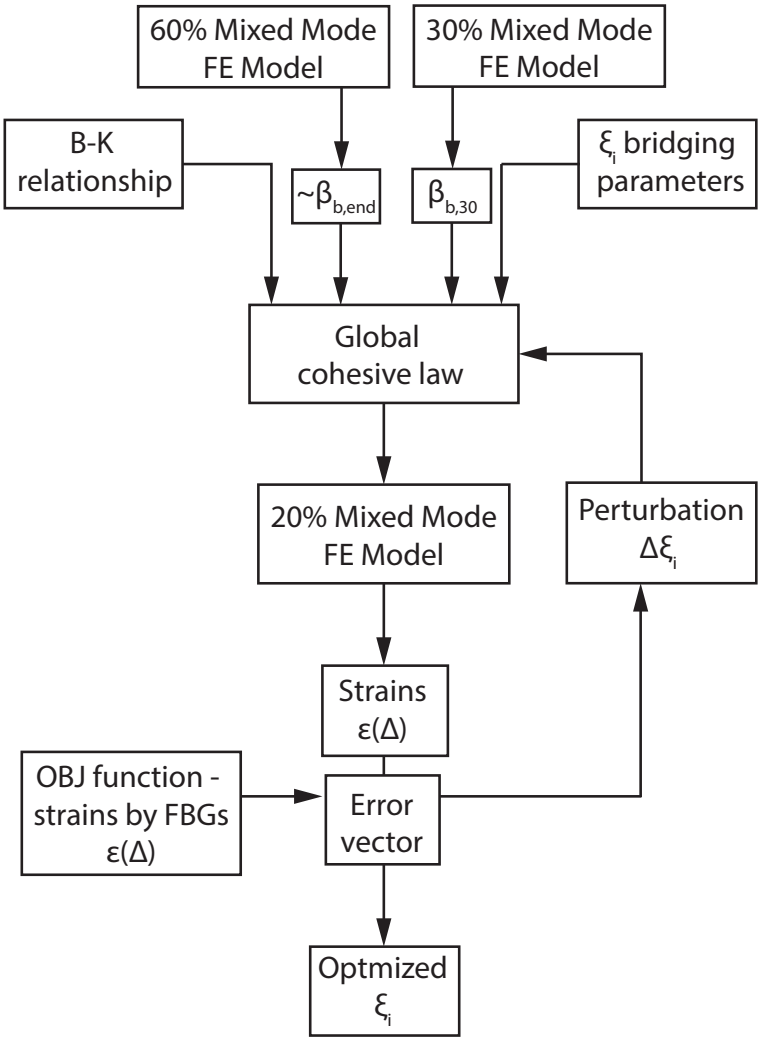

Figure 5.25: Mixed Mode optimization scheme

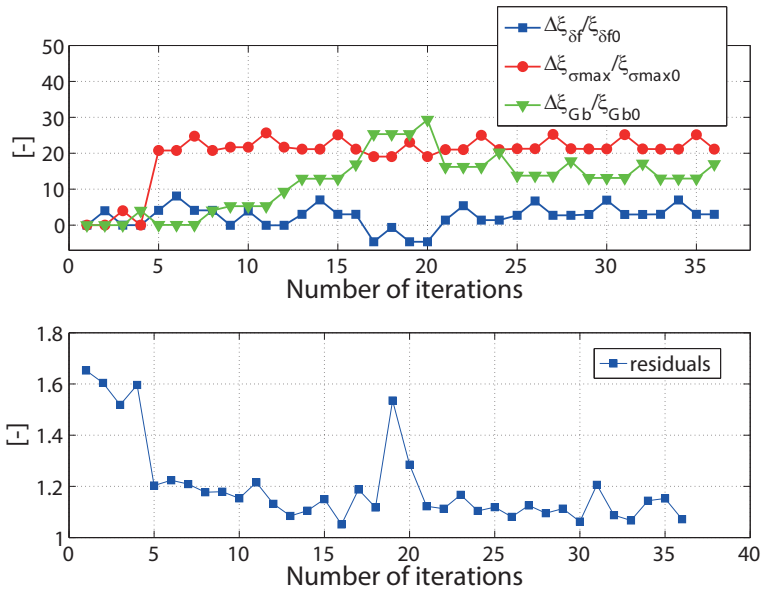

Figure 5.26: Evolution of the Mixed Mode bridging parameters along the optimization process

5.3.7 Variation of the B-K relationship

According to Section 5.3.5, the local displacement mode mixity β is able to properly represent the energy mode mixity μ only if β is constant in the process zone. Since for a MMB setting the local mode mixity keeps varying, the formula proposed by Camanho cannot properly simulate the process, both for crack initiation and propagation. For this reason, the B-K exponent $\eta = 1.61$, obtained by fitting the experimental ERR curves G_c at initiation as discussed in Section 5.3.2, is not able to simulate the correct crack onset and, therefore, the ERR at initiation. Since β approaches to lower values as soon as the cohesive element is damaged (as already discussed and shown in Figure 5.19), the energy at crack initiation is underestimated and the load-displacement curve is shifted to lower values with respect to the experimental ones, as shown in Figure 5.28 for a 40% mode mixity. The same underestimation is common to all the tested mode mixity.

Based on these reasons, the energies G_c at initiation, which define the first triangle of the cohesive law, cannot be tabulated versus $\mu = \frac{\beta^2}{1+\beta^2}$ since β does not represent the energy mode mixity imposed by the MMB setting. Therefore, the exponent η is defined by running a manual optimization process which aims to obtain the correct crack onset. The exponent η is thus changed and imposed equal to 1.3, which is found to be an optimal value to properly fit the crack initiation for all the Mixed Mode tests, as shown in Chapter 6.

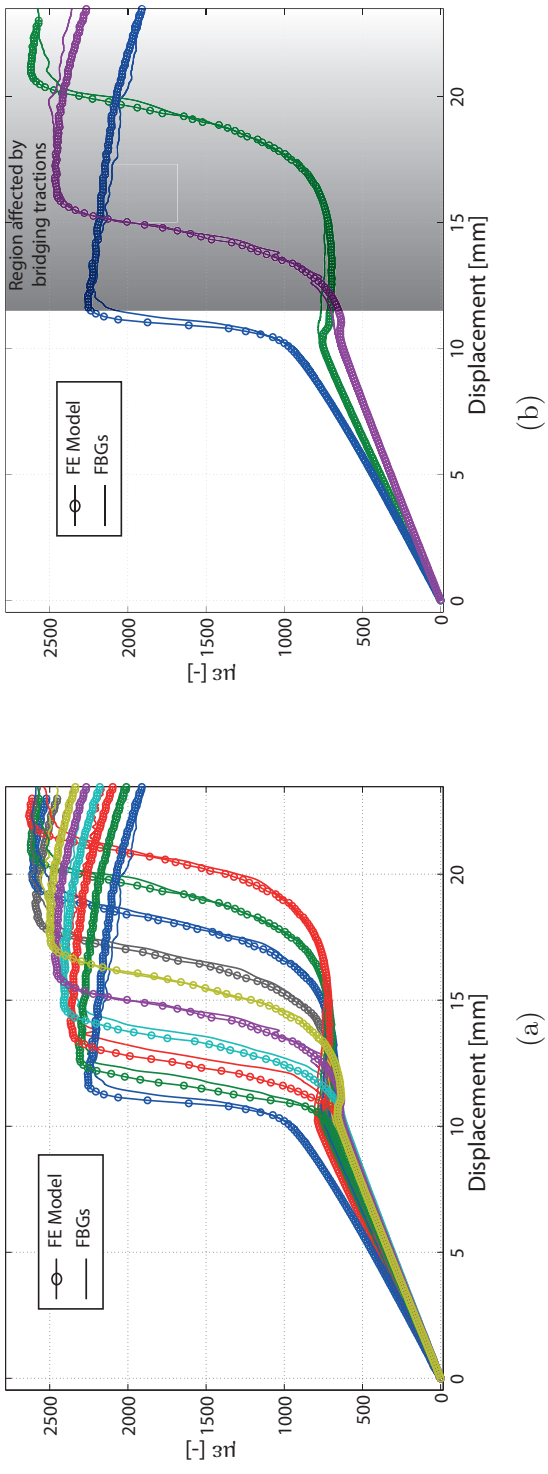

Figure 5.27: Comparison between the strains measured by the ten FBGs and the ones obtained by the FE Model for $\mu = 20\%$ after the optimization process: (a) all the FBG sensors (b) three FBG sensors

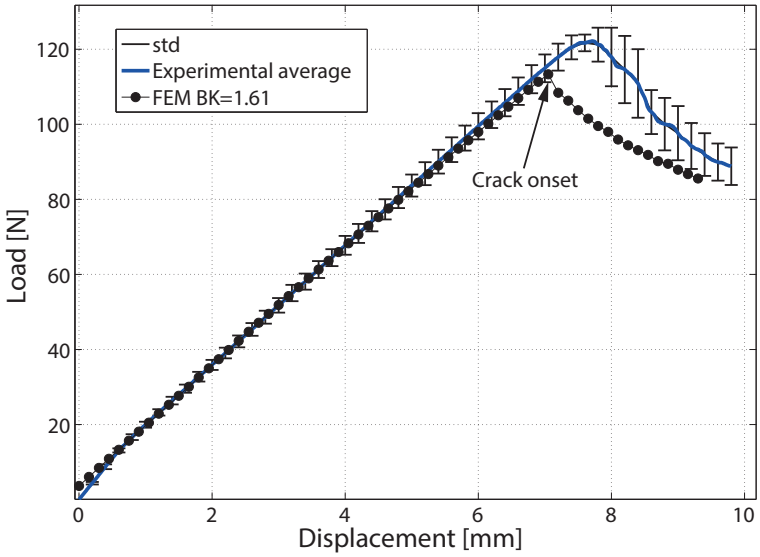

Figure 5.28: Load-displacement curve for Mixed Mode 40%, mismatch of the maximum load at crack initiation of the numerical model based on a B-K relationship with $\eta = 1.61$

Chapter 6

Comparison between experimental and numerical results

This chapter combines the experimental results shown in Chapter 4 with the numerical results obtained by the FE Models based on different numerical approaches. In order to simplify the presentation, we can refer to them depending on the cohesive law formulation adopted as:

- *FEM 1* - mode dependent Abaqus® internal tool, based only on the B-K relationship $G_c(\beta)$ (no bridging tractions)
- *FEM* 2 - mode dependent tabulated cohesive law with appended bridging tractions which are directly defined by the displacement mode mixity β
- *FEM* 3 - mode dependent tabulated cohesive law with appended bridging tractions and external routine to control the evolution of the displacement mode mixity β.

The second as well as the third approach implies the use of the global mode-dependent cohesive law shown in Figure 5.16, defined by the B-K relationship $G_c(\beta)$ and the bridging coefficients $\xi_i = \left[\xi_{G_b}, \xi_{\sigma_{max}}, \xi_{\delta_f}\right]$. The comparison between the experimental results and the different FE Models will better point out the limitations of the numerical approaches known so far and the prediction obtained by our implementation.

6.1 Mode I

The numerical results, obtained by the FE Models based on the cohesive formulations *FEM 1,2,3,* are discussed in terms of load, crack propagation, ERR and FBGs strains evolution.

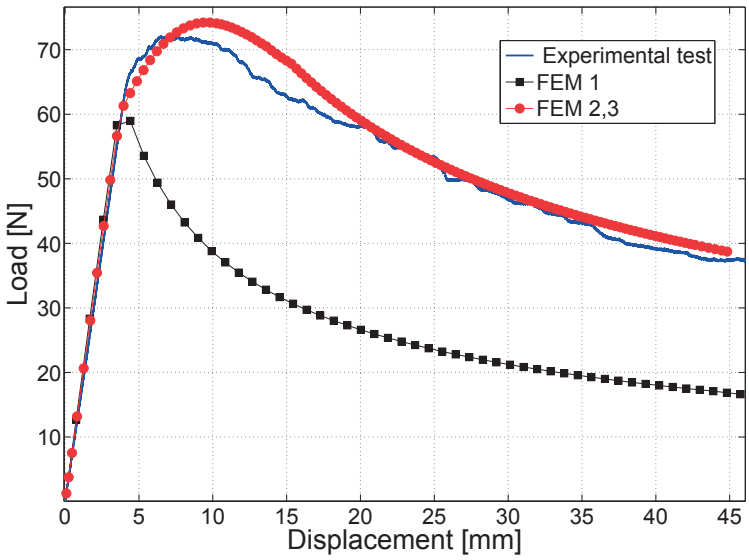

Figure 6.1: Mode I, comparison between experimental and numerical load-displacement curves

Figure 6.1 shows the comparison between the load-displacement curve obtained by the experiment and the numerical models *FEM 1*,2,3. The *FEM 1* approach is not able to properly fit the experimental curve due to the lack of bridging contribution, which actually largely affects the Mode I delamination process. The damage initiation is almost reached but the bridging development is not taken into account, which does not allow to fit the experimental load when the crack propagates. The large difference between the two curves points out the major role of bridging tractions in Mode I delamination. The numerical results based on *FEM* 2-3, characterized by the presence of bridging tractions, offer an optimal fitting for both damage initiation and crack propagation. In this case, due to the symmetry of the DCB setting, the cohesive elements are kept vertical all along the crack propagation, which corresponds to a constant $\beta = 0$. For this reason, there are no differences between the numerical model *FEM 2* and *3*, since $\beta_b = \beta = 0$. The fact that β does not change during the simulation, makes a mode-independent approach also suitable to represent the delamination process.

Figure 6.2 shows the evolution of the crack length versus the applied displacement. The *FEM 2,3* well capture the experimental results while *FEM 1* overestimates the crack length due to the lack of any toughening process. Without bridging tractions and the corresponding energy contribution, the crack would propagate faster since the fracture toughness does not increase as the crack tip advances.

The ERR curve as a function of the crack increment is shown in Figure 6.3. The energy

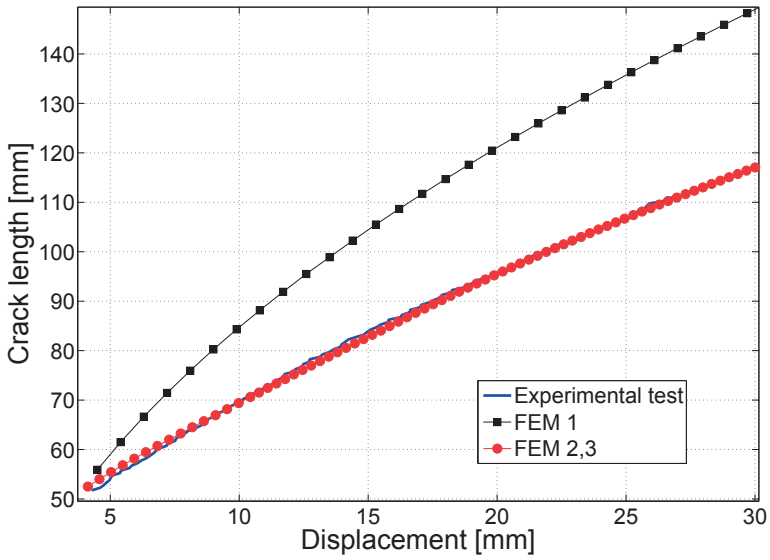

Figure 6.2: Mode I, comparison between experimental and numerical crack length-displacement curves

G_c at initiation is perfectly matched by all the FE Models since it is a constant input value for each cohesive law. The ERR obtained by the cohesive formulation based on *FEM* 2-3 and calculated by using the compliance method, well predicts the experimental trend, meaning that the bridging energy contribution, defined by the parameters $\sigma_{max}, \delta_{fmax}$ and γ (see Table 5.1), is correct. The small mismatch in the rising part is due to the fact that the cohesive law is assumed to be representative of a steady state, causing a slight different transient region as already mentioned in [99]. The ERR computed by *FEM 1* does not show any increase since no bridging effects are taken into account.

For Mode I delamination test, the optimization process and the implementation of the global mode-dependent cohesive law properly represent the delamination process and the bridging development. The evolution of the load, crack length and ERR are very well predicted by using the numerical approaches *FEM 2,3* while, if the proper bridging contribution is not added as in *FEM 1* case, the FE Model is able to catch only the damage initiation but cannot simulate the crack propagation.

The strain curves are already shown in Figure 5.5. Note that the experimental FBG data are involved in the objective function, used to perform the optimization process.

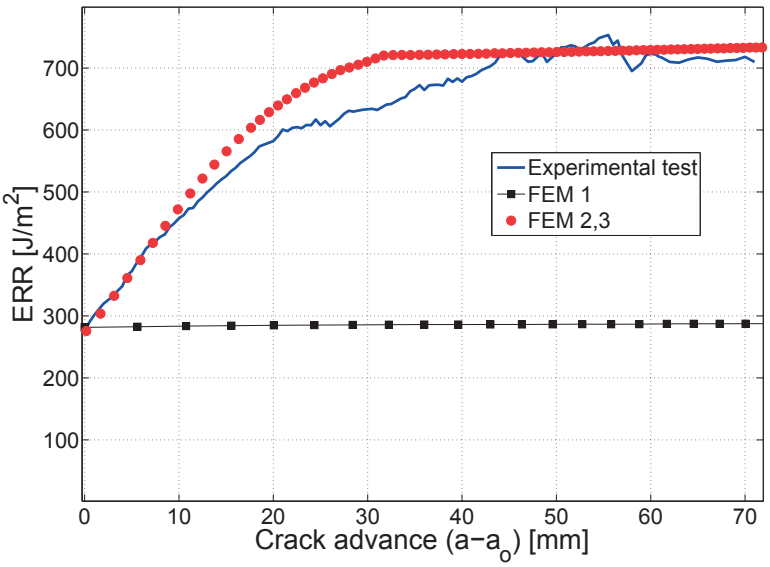

Figure 6.3: Mode I, comparison between experimental and numerical ERR curves

6.2 Mixed Mode

In this section, the Mixed Mode results obtained by the three different numerical approaches *FEM 1,2,3* are shown and discussed. The importance to add the proper bridging contribution and to control the evolution of the β parameter is pointed out by showing the differences in terms of load-displacement, crack propagation, total energy and strains evolution. The numerical results for Mixed Mode delamination and their differences, finally demonstrate the fact that the standard numerical models known so far are not able to accurately predict the delamination process when large scale bridging occurs.

6.2.1 20% Mixed Mode

The Mixed Mode delamination test performed at $\mu = 20\%$, according to the experimental results discussed in Chapter 4, shows that large scale bridging affects the delamination behavior. The curves obtained by the average of the experiments and the ones computed by the FE Models based on the numerical approaches *FEM 1,2,3* are shown in terms of load-displacement in Figure 6.4, crack-length-displacement in Figure 6.5 and ERR in Figure 6.6.

- *FEM 1* - The numerical approach *FEM 1,* based on the B-K relationship without any bridging contribution, shows important differences with respect to the experimental result. The lack of bridging tractions causes an important underestimation and a different

shape of the load-displacement curve. The crack evolution is also affected since the model overestimates the value obtained during the experiment. This means that the bridging energy contribution involved in the experiments allows the crack to slow down and, therefore, to increase the fracture toughness. Note that the ERR for the *FEM 1* approach is perfectly flat since no toughening processes are involved, which does not well represent the rising energy experimentally obtained. The strains evolution, corresponding to the FBG sensors, is shown in Figure 6.7(a), which points out the large mismatch between the numerical and the experimental results. Figure 6.7(b) omits some FBGs curves for a better viewing. Based on these considerations, it is possible to assert that the Abaqus® internal cohesive formulation for Mixed Mode delamination is not appropriate to describe a delamination process when large scale bridging occurs.

- *FEM 2* - The numerical approach *FEM 2* adds the bridging tractions to the mode-dependent cohesive law by using the optimized bridging parameter set $\xi_i = \left[\xi_{G_b}, \xi_{\sigma_{max}}, \xi_{\delta_f}\right]$, described in Table 5.3. In this case, bridging contribution only depends on the displacement mode mixity β all along the delamination process, which involves the issues discussed in Section 5.3.5. As expected, the load is overestimated with an evident rising trend due to the variation of β in the process and bridging zone, which approaches to lower values, involving extra bridging tractions as the delamination process goes on. This numerical artifact is thus well pointed out by the corresponding rising load-displacement curve. This effect also influences the crack propagation, by underestimating the experimental values. The excess of bridging contribution increases the fracture toughness which slows down the crack propagation. The ERR is, therefore, higher than the experimental one and shows a continuous increasing trend. The strains evolution, corresponding to the FBG sensors, is displayed in Figure 6.8, which shows an important overestimation of the numerical model due to an excess of bridging tractions. Based on these considerations, the *FEM 2* numerical approach cannot be used to simulate a delamination process under Mixed Mode conditions and large scale bridging, due to the uncontrolled evolution of β.

- *FEM 3* - The numerical approach *FEM 3* combines the proper bridging contribution with the Fortran® external routine to control the evolution of β^*. The bridging parameters $\xi_i = \left[\xi_{G_b}, \xi_{\sigma_{max}}, \xi_{\delta_f}\right]$, obtained by fitting the strain curves along the FBGs path, are found to be appropriate to properly represent the experimental load-displacement curve, showing a negligible difference within the standard deviation limits. The crack evolution is also perfectly simulated both in terms of actual values and trend. The ERR matches with the experimental one, showing that the proper bridging energy contribution is added and that no steady state is reached. The strains, already shown in Figure 5.27, are adopted

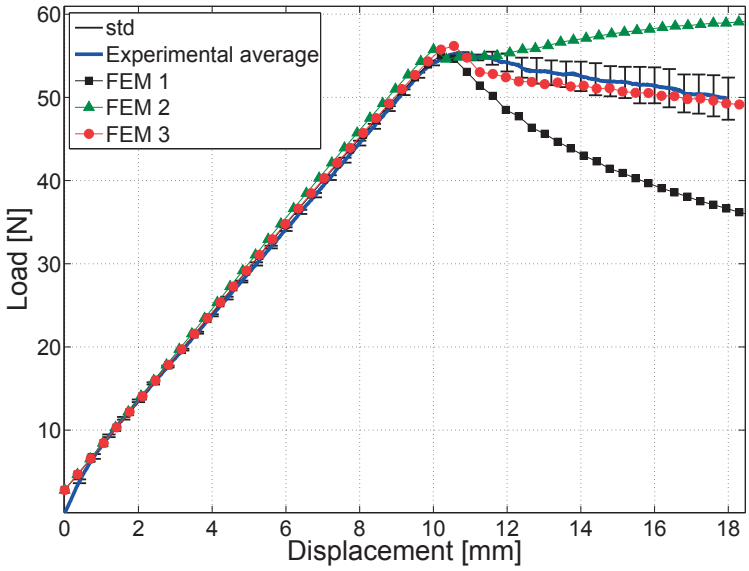

Figure 6.4: Mixed Mode 20%, comparison between experimental and numerical load-displacement curves

as objective data to define the correct bridging parameters. Therefore, the assumption made in Section 5.3.5, which implies the bridging contribution depending on the β^* value at the end of the process zone without any extra evolution, allows to accurately describe the Mixed Mode delamination process when large scale bridging is involved.

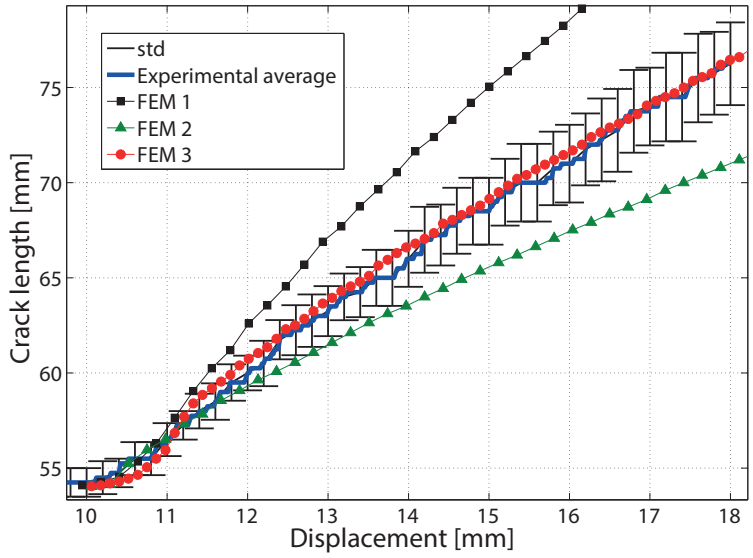

Figure 6.5: Mixed Mode 20%, comparison between experimental and numerical crack length-displacement curves

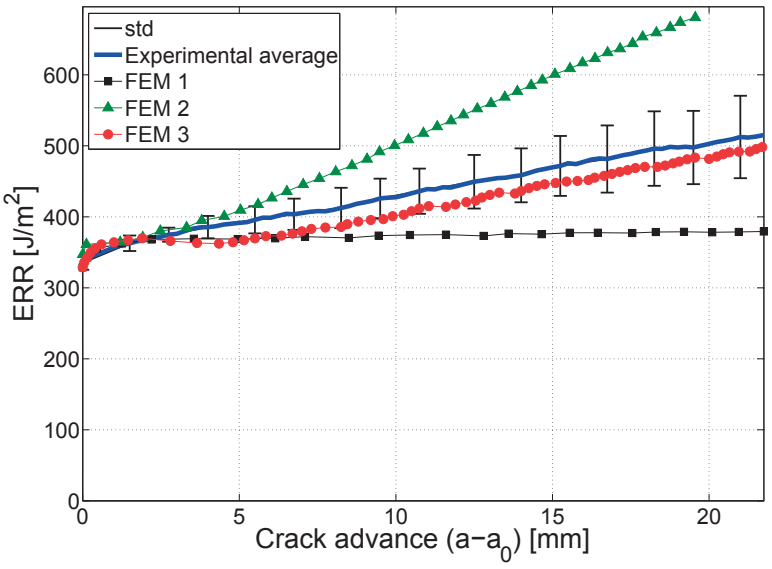

Figure 6.6: Mixed Mode 20%, comparison between experimental and numerical ERR curves

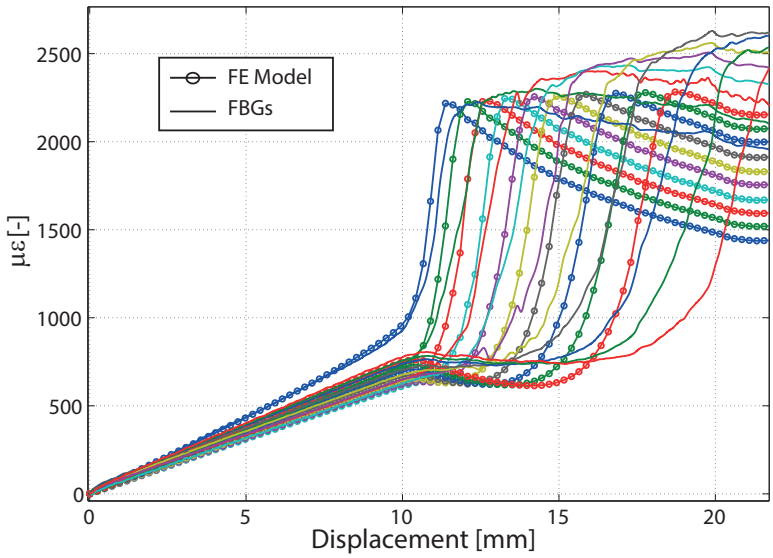

(a)

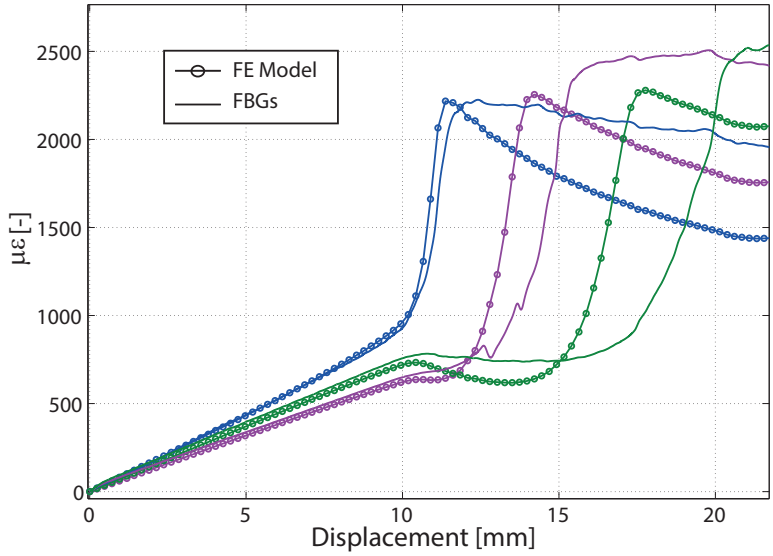

(b)

Figure 6.7: Mixed Mode 20%, comparison between the experimental FBGs and the corresponding *FEM 1* numerical strain curves, (a) all the FBG sensors (b) three FBG sensors

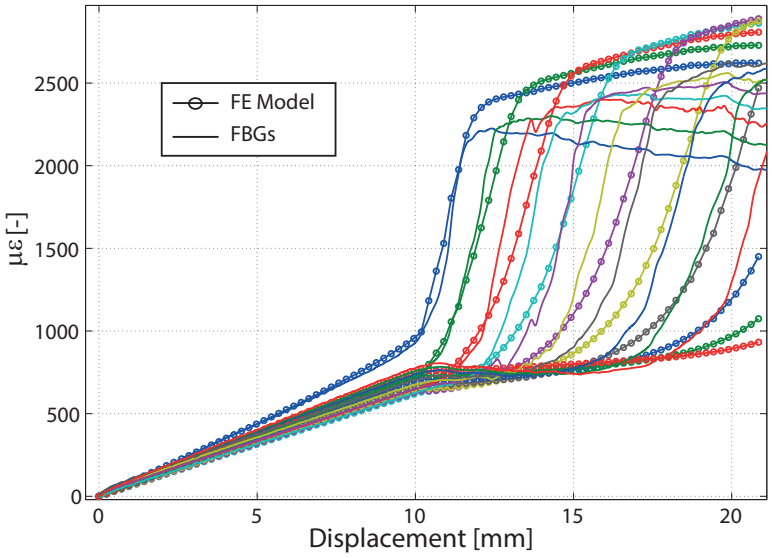

(a)

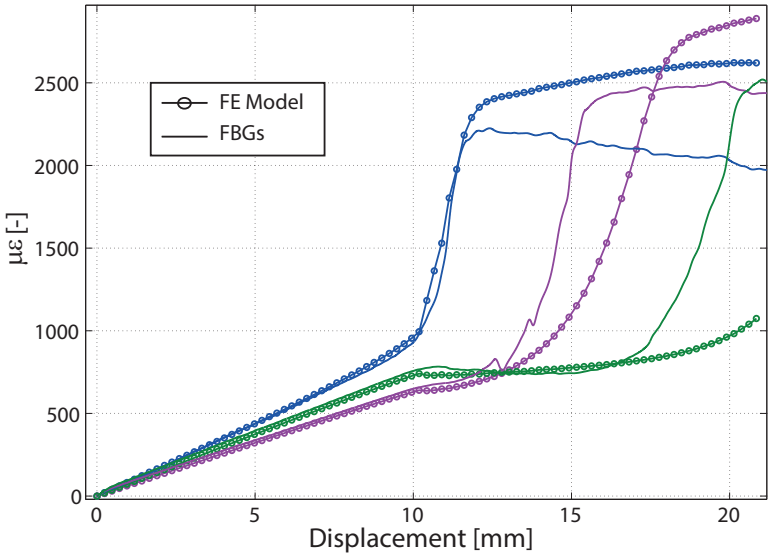

(b)

Figure 6.8: Mixed Mode 20%, comparison between the experimental FBGs and the corresponding *FEM 2* numerical strain curves, (a) all the FBG sensors (b) three FBG sensors

6.2.2 30% Mixed Mode

The Mixed Mode delamination test performed at $\mu = 30\%$ represents, as discussed in Section 5.3.2 and shown in Figure 5.13, a threshold between the large scale bridging which occurs between $\mu = 0\%$ and 20% and the small scale bridging in $\mu = 40\%$ and 60%. Although the bridging energy contribution for $\mu = 30\%$ is lower than the one obtained for $\mu = 20\%$, the load-displacement in Figure 6.9, the crack length-displacement in Figure 6.10 and the ERR curves in Figure 6.11 still show the importance to add the correct bridging tractions to properly predict the delamination behavior.

- *FEM 1* - The numerical approach *FEM 1* underestimates the load in the crack propagation region due to the lack of bridging tractions. Therefore, the crack propagates faster overestimating the experimental one. Consistently, the ERR is flat, lower than the experimental one, without showing any rising part while the strains, corresponding to the FBGs position, are shown in Figure 6.12. The difference between the strains computed by using the *FEM 1* approach and the ones measured by the FBGs, is almost negligible at the end of the rising part, which represents the crack tip position, while it increases as the crack propagates and bridging develops. However, the fact that the bridging contribution in 30% mode mixity is low makes the difference between the experimental results and the *FEM 1* numerical simulations smaller with respect to the 20% Mixed Mode case.

- *FEM 2* - The numerical approach *FEM 2* provides the contribution of bridging tractions to the mode-dependent cohesive law. As already discussed, the continuous variation of β in the process and bridging zones causes an overestimation of tractions which implies a higher load-displacement curve and a slower crack propagation. Therefore, the ERR shows an important increase due to the fact that, as β varies and approaches to low values, extra tractions arise providing additional energy. The strains are plotted in Figure 6.13, which points out how much they are affected by an excess of bridging tractions. The strains keep rising since the crack does not properly propagate.

- *FEM 3* - The numerical approach *FEM 3* provides optimum results also for the 30% mode mixity. The evolution of load, crack length and ERR are perfectly predicted. This result is very important since the bridging coefficients $\xi_i = \left[\xi_{G_b}, \xi_{\sigma_{max}}, \xi_{\delta_f}\right]$ are obtained by an optimization process performed with a 20% Mixed Mode Model. The numerical results at $\mu = 30\%$ acts, therefore, as a check of the assumptions made in Chapter 5. The strains are also well predicted both for the steep and crack propagation zone, as shown in Figure 6.14.

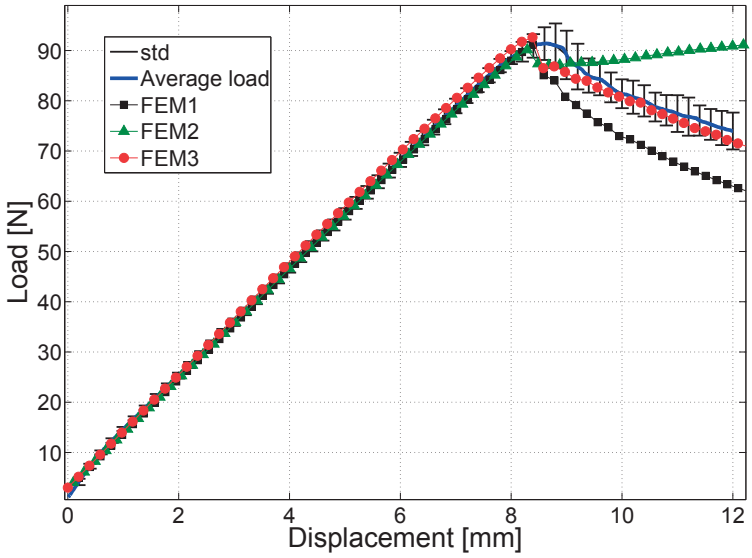

Figure 6.9: Mixed Mode 30%, comparison between experimental and numerical load-displacement curves

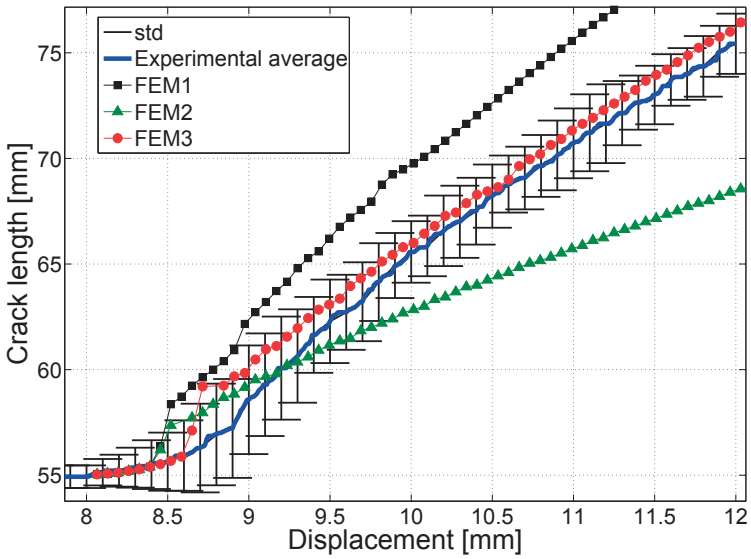

Figure 6.10: Mixed Mode 30%, comparison between experimental and numerical crack length-displacement curves

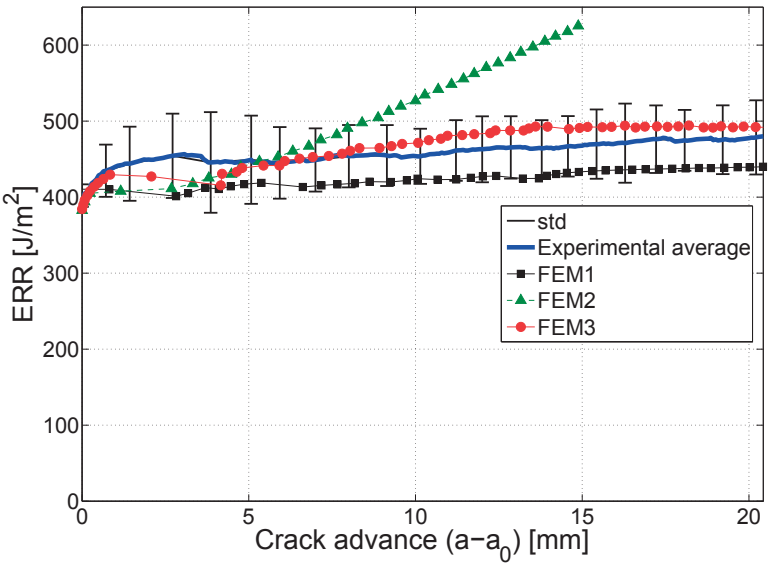

Figure 6.11: Mixed Mode 30%, comparison between experimental and numerical ERR curves

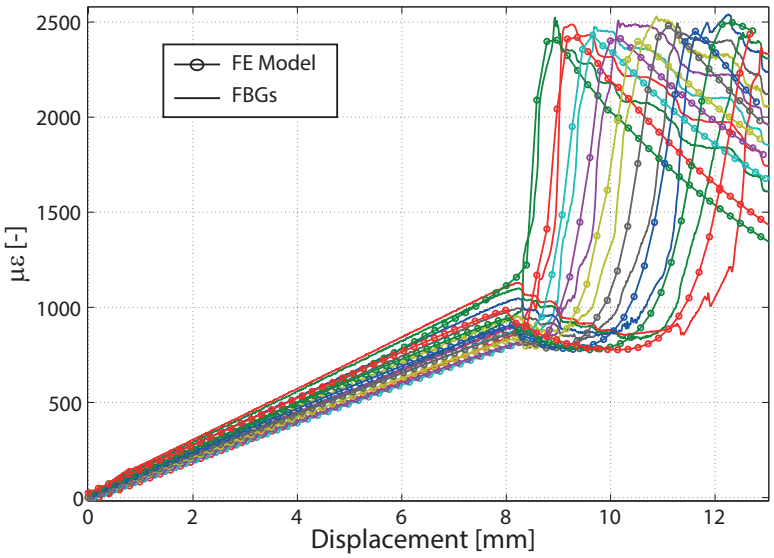

(a)

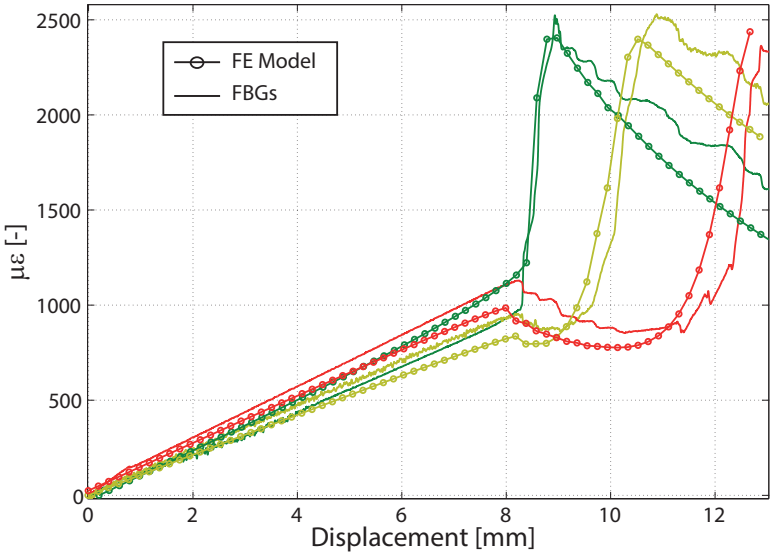

(b)

Figure 6.12: Mixed Mode 30%, comparison between the experimental FBGs and the corresponding *FEM 1* numerical strain curves, (a) all the FBG sensors (b) three FBG sensors

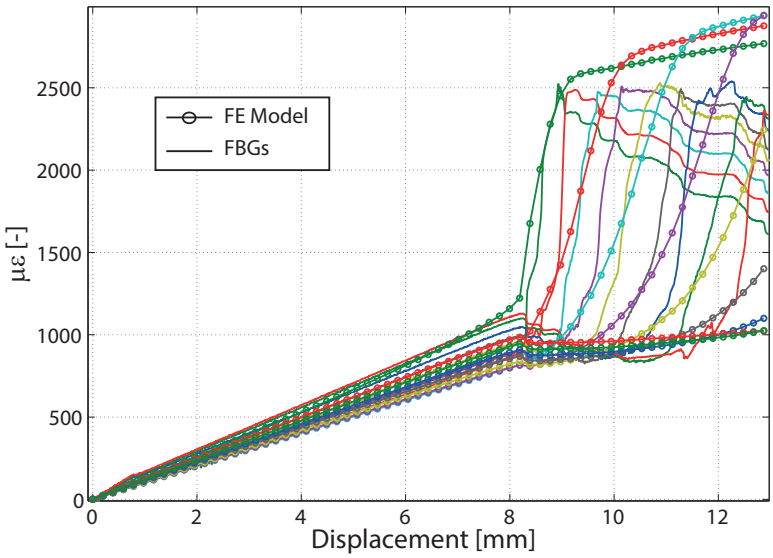

(a)

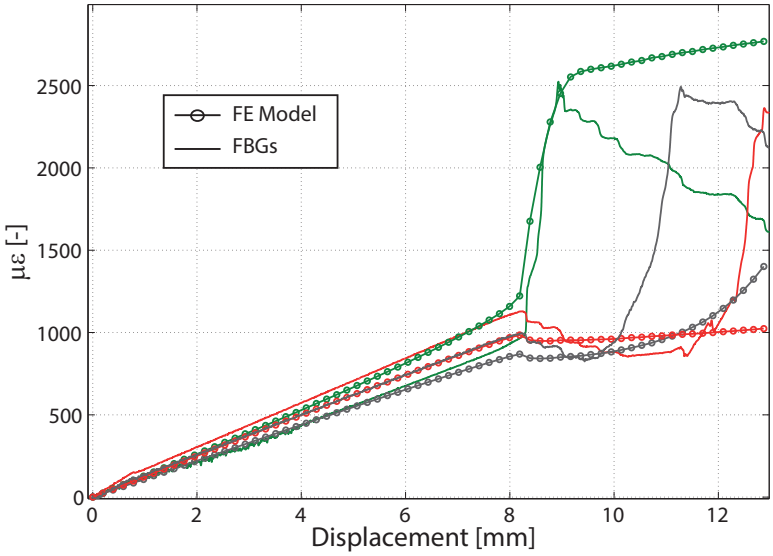

(b)

Figure 6.13: Mixed Mode 30%, comparison between the experimental FBGs and the corresponding *FEM 2* numerical strain curves, (a) all the FBG sensors (b) three FBG sensors

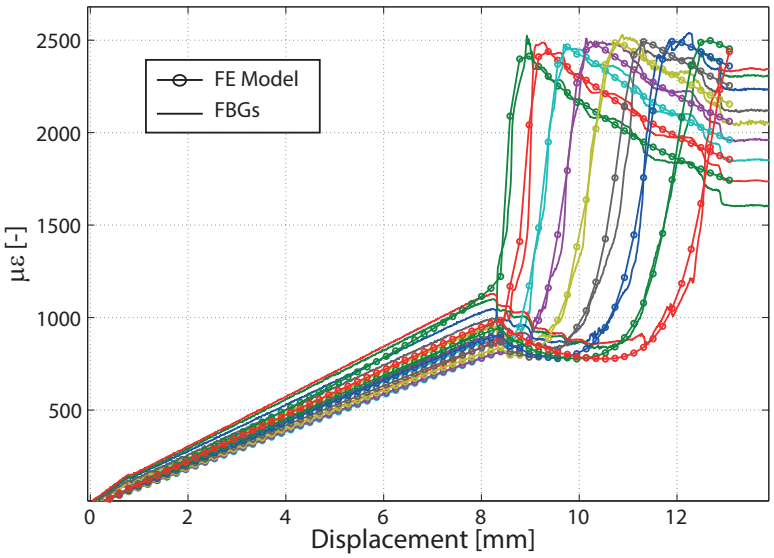

(a)

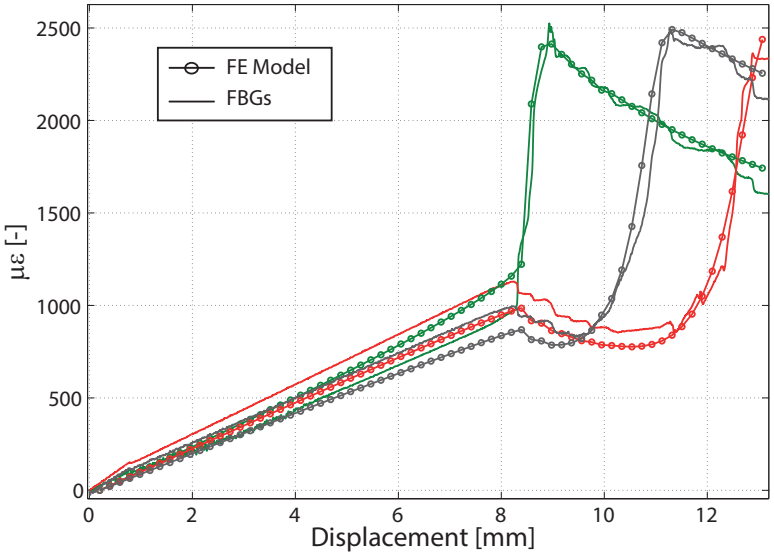

(b)

Figure 6.14: Mixed Mode 30%, comparison between the experimental FBGs and the corresponding *FEM 3* numerical strain curves, (a) all the FBG sensors (b) three FBG sensors

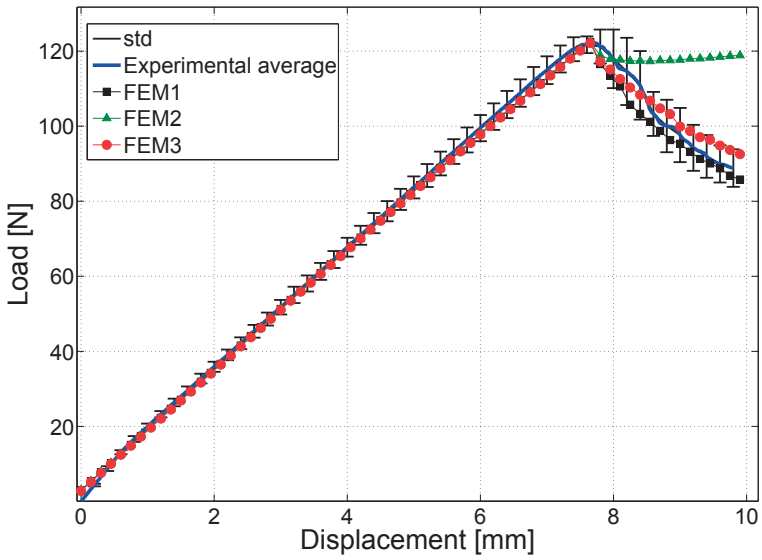

Figure 6.15: Mixed Mode 40%, comparison between experimental and numerical load-displacement curves

6.2.3 40% Mixed Mode

The 40% mode mixity, according to the experimental results shown in Chapter 4, shows a small and almost negligible amount of bridging. Looking at the load-displacement curve in Figure 6.15, crack length-displacement curve in Figure 6.16 and the ERR curve in Figure 6.17, the difference between the numerical results obtained by using the cohesive formulation based on the *FEM 1* and *FEM 3* approach is very small. This means that the experimental bridging contribution is low enough to allow using a cohesive formulation only based on the B-K relationship, without any bridging contribution.

The *FEM 2*, instead, provides results very far from the experimental ones. The not-controlled evolution of β in the bridging zone keeps generating new bridging tractions even if the two crack faces are already separated, which implies a higher load and energy evolution. The strains values are not plotted since, due to the higher scatter over the experimental results, the FBGs strains obtained by the single specimen with the embedded optical fiber do not well represent the average.

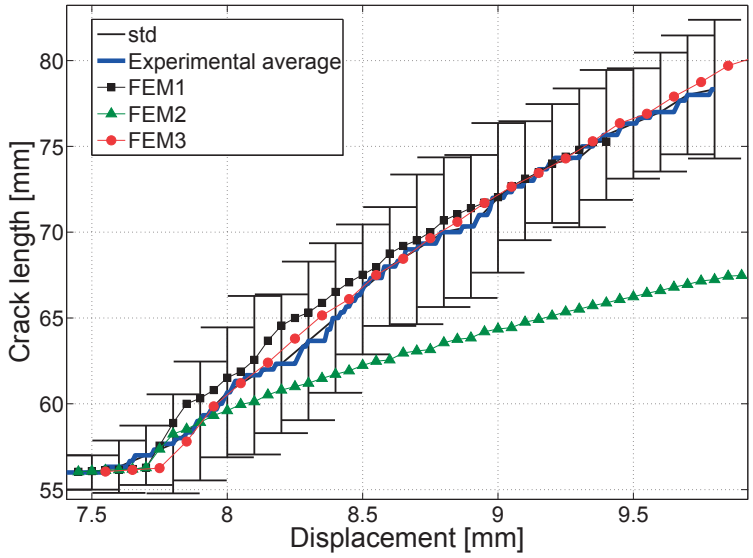

Figure 6.16: Mixed Mode 40%, comparison between experimental and numerical crack length-displacement curves

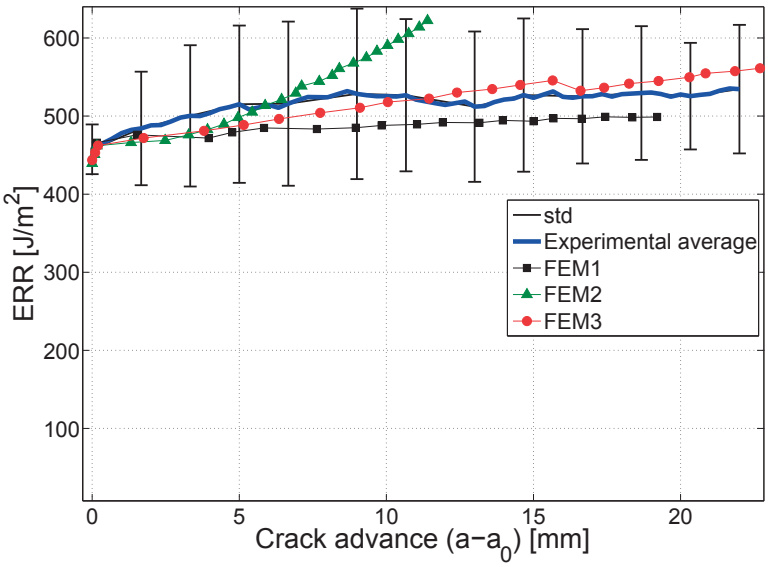

Figure 6.17: Mixed Mode 40%, comparison between experimental and numerical ERR curves

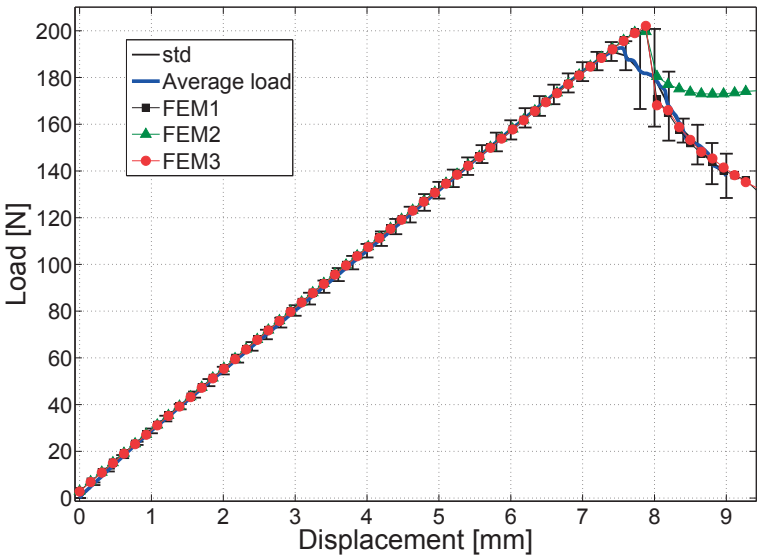

Figure 6.18: Mixed Mode 60%, comparison between experimental and numerical load-displacement curves

6.2.4 60% Mixed Mode

According to the experimental results, the delamination process performed at $\mu = 60\%$ shows a negligible bridging contribution. Consequentially, the numerical results, obtained by the FE Models based on the *FEM 1* and *FEM 3* cohesive formulations, are superimposed. The load-displacement curves in Figure 6.18, the crack length-displacement curves in Figure 6.19 and the ERR curves in Figure 6.20 follow the same path. Accordingly to these results, it is possible to assert that both *FEM 1* and *FEM 3* cohesive formulation approach are perfectly able to predict the 60% Mixed Mode delamination, since the experimental bridging contribution is negligible.

As expected, also in this case the *FEM 2* approach overestimates the bridging tractions, providing wrong results over all the objective curves.

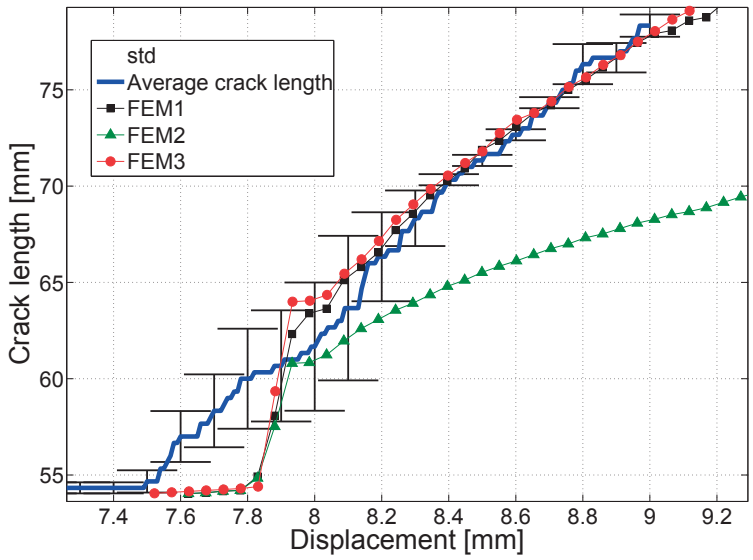

Figure 6.19: Mixed Mode 60%, comparison between experimental and numerical crack length-displacement curves

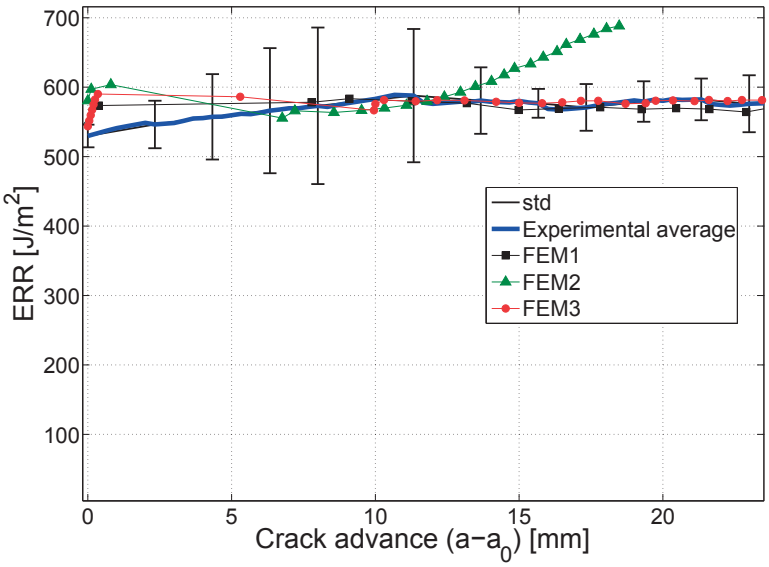

Figure 6.20: Mixed Mode 60%, comparison between experimental and numerical ERR curves

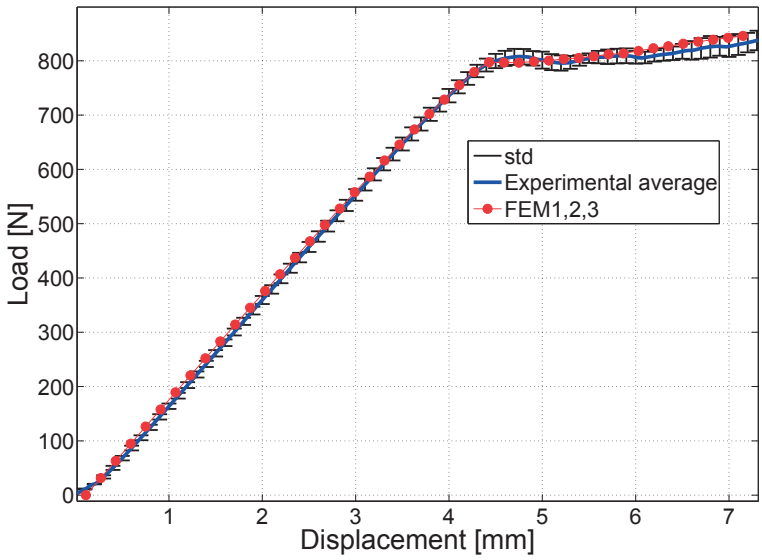

Figure 6.21: Mode II, comparison between experimental and numerical load-displacement curves

6.3 Mode II

The Mode II delamination test is performed by using a 4-ENF setting. The delamination occurs due to pure shear, without any bridging toughening process, as discussed in Chapter 4. Since only shear is present without any opening, the displacement mode mixity is constant and tends to infinity $\beta = \frac{\delta_1}{\delta_3} \to \infty$ which corresponds to pure Mode II $\mu = 1$ (see Equation 5.38).

In this particular case, where bridging is not involved and β is constant, the three numerical approaches *FEM 1,2,3* coincide as expected. The prediction for the load-displacement, crack length-displacement and ERR is very accurate as shown respectively in Figures 6.21, 6.22, 6.23. The FE Models provide an optimal prediction also for the strain curves corresponding to the FBGs position, as shown in Figure 6.24. The slight mismatch over the last FBG sensor is consistent with the small overestimation of the crack length curve at the end of the delamination process: this may be due to the friction effects that are not taken into account in the numerical simulation.

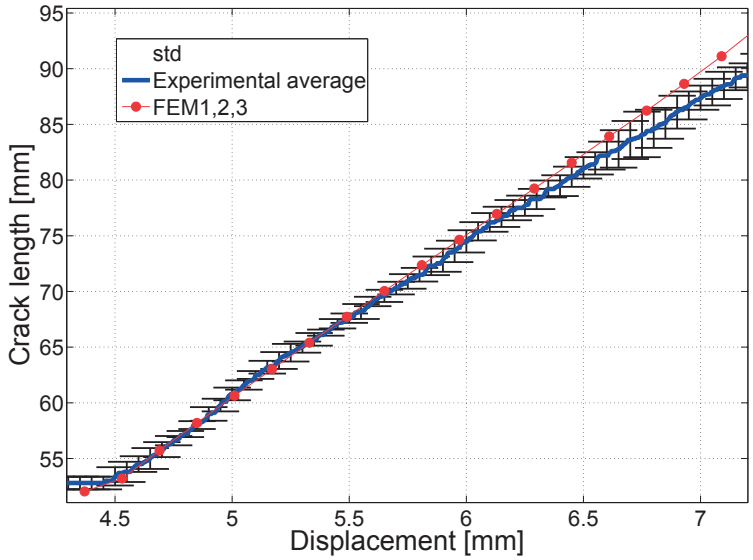

Figure 6.22: Mode II, comparison between experimental and numerical crack length-displacement curves

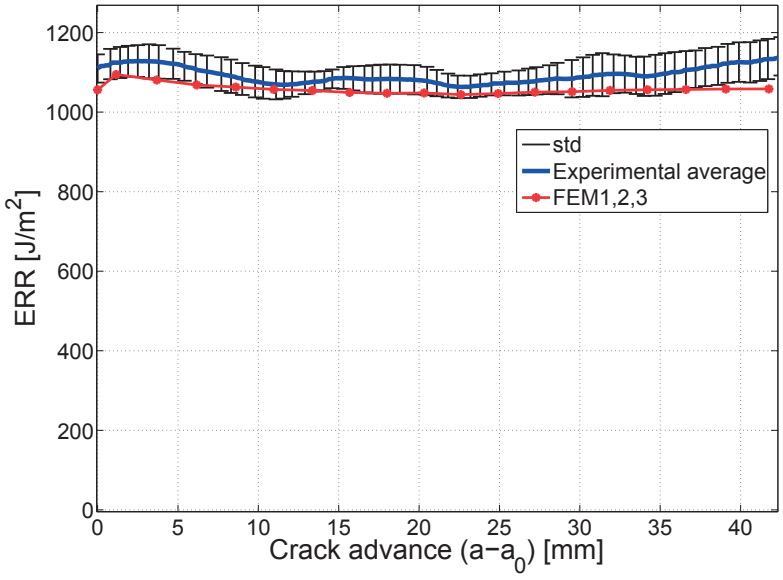

Figure 6.23: Mode II, comparison between experimental and numerical ERR curves

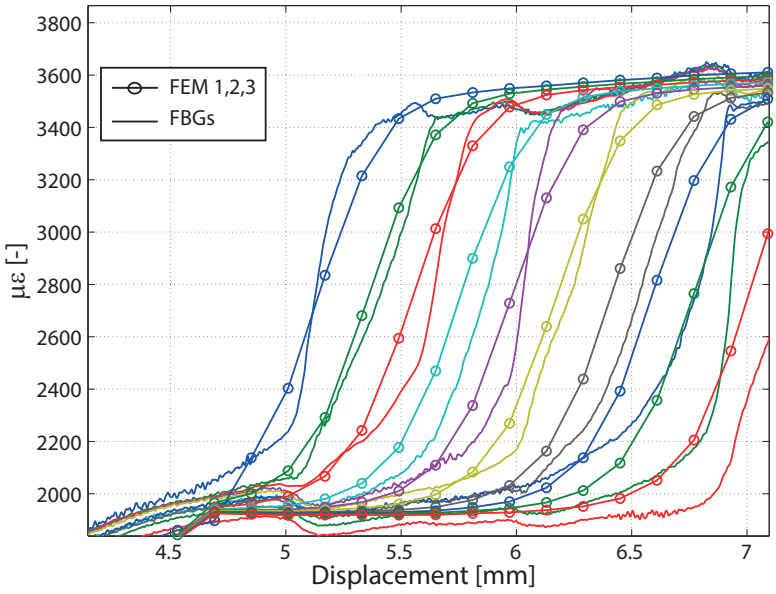

(a)

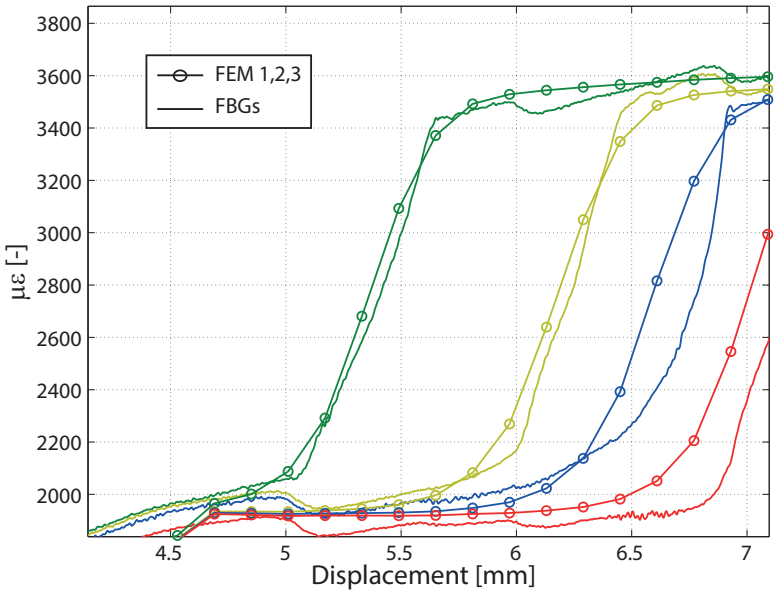

(b)

Figure 6.24: Mode II, comparison between the experimental FBGs and the corresponding numerical *FEM 1,2,3* strain curves, (a) all the FBG sensors (b) four FBG sensors

6.4 Summary

This chapter outlines the comparison between the experimental results and three different numerical approaches for a mode-dependent cohesive law formulation, characterized by the B-K relationship without any bridging traction (*FEM 1*), by the bridging contribution only dependent on β (*FEM* 2) and by the combination of bridging and the external routine to control the displacement mode-mixity evolution β^*(*FEM* 3). The parameters $\xi_i = \left[\xi_{G_b}, \xi_{\sigma_{max}}, \xi_{\delta_f}\right]$ (Table 5.3), which defines the bridging tractions as a function of β, are obtained by the optimization process discussed in Chapter 5.

The numerical results show that the cohesive law formulation *FEM* 3 is able to predict the delamination behavior over a wide range of mode mixities, from pure Mode I which is largely affected by bridging, up to pure Mode II, going through the 20%,30%,40% and 60% Mixed Mode delamination. By using a unique mode-dependent cohesive law, based on the displacement mode-mixity β^* computed by the external routine, and blocking its evolution at the end of the process zone, the customized FE Model is able to describe properly the bridging contribution over multiple mode mixities, thus predicting the load, crack and ERR evolution.

These results gain more importance if compared with the ones obtained by using the conventional Abaqus® internal cohesive formulation (*FEM 1*) which is found to be inappropriate for the simulation of the MMB delamination test. The fact that β varies in the process zone makes this approach not valid as proved by the fact that the B-K exponent η cannot be derived by the experimental results but it must be obtained by performing FE simulations to catch the correct crack initiation, as previously discussed in Section 5.3.7. In addition, the conventional approach does not take into account the bridging effects and therefore it is not able to predict the experimental delamination process when an important bridging contribution is present.

Also the cohesive formulation *FEM* 2, which makes the bridging contribution only dependent on the displacement mode mixity β, is not suitable to properly represent the delamination process since it causes a numerical artifact in which new bridging tractions may appear when the two crack faces are already separated. This particular behavior is due to the not-controlled evolution of β.

Chapter 7

Conclusions

This work provided the possibility to study in detail the behavior of delamination for unidirectional CFRP materials subjected to different mix mode ratios, both by running experiments and numerical simulations. In particular, the effects of mode mixity on the fracture toughness at damage initiation and the corresponding bridging contribution are analyzed. Experiments are performed at pure Mode I, Mixed Mode at 20%, 30%, 40%, 60% and pure Mode II, monitoring the applied load, crack evolution and internal strains by using embedded optical fibers with Bragg gratings. The obtained results allow to shed light on the influence of bridging tractions for different mode mixities and the stability of the crack propagation. The main experimental results can be summarized as follows:

- the critical ERR G_c at crack initiation increases with the applied mode mixity
- the bridging contribution depends on the applied mode mixity
- large scale bridging occurs in pure Mode I and in Mixed Mode up to $\mu = 30\%$
- negligible bridging contribution is found in Mixed Mode delamination performed at $\mu = 40\%$ and 60%
- no bridging contribution in pure Mode II delamination.

The innovative customized Mixed Mode FE numerical model based on cohesive elements, which aims to properly predict the delamination behavior over a wide range of different mode mixities, represents the core of the this work since the standard cohesive law formulations implemented in commercial software are not able to accurately describe the experimental results. This study allowed for better understanding the main limitations and issues associated with this approach. In particular it should be noted that:

- the formulation implemented in Abaqus® and proposed by Camanho [98], which correlates the global mode mixity in terms of energy $\mu = \frac{G_{II}}{G_{tot}}$ to the local mode mixity $\beta = \frac{\delta_{shear}}{\delta_{normal}}$ according to the formula $\mu = \frac{\beta^2}{1+\beta^2}$, is valid only if β is constant over the whole damage process zone. Since it is found that the local displacements mode mixity β varies in the process zone for a Mixed Mode test based on the MMB setting, the correlation between the local and global mode mixity is not valid anymore, as discussed in Section 5.3.4

- the bridging tractions and the corresponding energy contribution cannot be directly related to the local mode mixity β since, as previously mentioned, it keeps changing both in the process and bridging zone, thus it cannot be related to the global mode mixity μ applied by the MMB setting. This problem is discussed in detail in Section 5.3.5

- the β evolution corresponding to different cohesive elements is different even if the theoretical global mode mixity μ, applied by the MMB setting, is constant

- the β value changes in the bridging zone and approaches to lower values which are characterized by the presence of bridging tractions. This causes a numerical artifact consisting of extra tractions arising far from the crack tip, exceeding the experimental bridging contribution.

The aforementioned issues, which affect the standard Mixed Mode models, are now solved. The innovative customized Abaqus® model is based on the displacement ratio β^*, computed by an external Fortran® routine (see Section 5.3.5), which is used as a mode mixity indicator but not correlated to the global mode mixity μ. The main characteristics of this Abaqus® model are:

- in the process zone, β^* corresponds to the local displacement mode mixity β

- the B-K relationship $G_c = G_{Ic} + (G_{IIc} - G_{Ic})\mu^\eta$, which correlates the critical energy at damage initiation G_c to the applied mode mixity μ, by imposing an exponent η to fit the experimental critical energies, does not necessarily reflect correctly the energy when cohesive elements are involved, since μ and β cannot be related. Therefore, the exponent η is changed and defined by performing numerical simulations for different Mixed Mode models until the right crack initiation is obtained (see Section 5.3.7)

- at the critical damage corresponding to bridging initiation, β^* is kept constant as $\beta_b = \beta^*$. This algorithm is based on the assumption that the bridging characteristics depend on the stress field in the cracked matrix region, without any further evolution

- three different functions are defined, as a function of β^*, to describe the evolution of the bridging energy contribution G_b, the maximum stress σ_{max} provided by the bridging

tractions and the maximum COD at failure δ_f. The shape of these functions can be changed by varying the corresponding bridging parameters $\xi_i = \left[\xi_{G_b}, \xi_{\sigma_{max}}, \xi_{\delta_f}\right]$

- the optimized set of bridging coefficients ξ_i is defined by performing an optimization process for a 20% Mixed Mode model, where the objective data are represented by the strains measured by ten FBG sensors located over the crack plane

This work provides a detailed analysis of the main characteristics for the experiments and numerical approaches related to Mixed Mode delamination, when large scale bridging occurs. The limitations associated with the standard Mixed Mode models are pointed out, analyzed and finally a new cohesive approach is established, providing a numerical tool able to predict the correct delamination behavior over a wide range of different mode mixities, from pure Mode I up to pure Mode II, by using a unique mode-dependent cohesive law which allows to evaluate the proper bridging contribution.

7.1 Future work

The Mixed Mode experiments performed up to now provide a complete set of data to describe the delamination process in unidirectional CFRP. Therefore, an interesting evolution of this work consists on performing additional Mode I, Mode II and Mixed Mode experiments by changing both the geometry of the specimen, such as the thickness, and the fibers orientation. Even if the bridging contributions will be different with respect to the ones here obtained, it would be very interesting to check the evolution of the bridging coefficients $\xi_i = \left[\xi_{G_b}, \xi_{\sigma_{max}}, \xi_{\delta_f}\right]$, which represent the variation rate of G_b, σ_{max} and δ_f with respect to β^*. Experimentally, the Digital Image Correlation (DIC) method can serve well to measure local crack opening displacements to validate and extend the macro and micro mechanical models.

The numerical model can be also improved, in particular the way to insert the global cohesive law in Abaqus®. Up to now, if the cohesive law has to be customized in order to add bridging tractions, the tabulation form is the only option currently available. This requires the evolution of the damage parameter D with respect to the magnitude of the crack opening displacement δ_m and the displacement mode mixity β. If the cohesive law is discretized by using 300 points along the δ_m axis and 400 points along the β axis, it means tabulating 120.000 values. The Abaqus® solver, therefore, has to interpolate these curves at each time step for each cohesive element, which clearly slows down the simulation. Since the mesh size chosen for the cohesive layer is very fine, in order to improve the accuracy of the solution, the amount of cohesive elements is high: therefore, the tabulated form does not represent the optimal solution for computational efficiency. For this reason, it would be very useful to describe the evolution of the

damage parameter D by defining an analytical function in two variables so that $D = D(\delta_m, \beta)$. This approach would strongly reduce the computational time needed to complete the numerical simulation and it would provide a better accuracy.

A micro-mechanical approach for a crack subjected to mixed mode conditions with bridging will be of importance to validate and support the macro-mechanical model developed in this work.

Bibliography

[1] P Robinson and J M Hodgkinson. 9 - Interlaminar fracture toughness. In J M Hodgkinson, editor, *Mechanical Testing of Advanced Fibre Composites*, Woodhead Publishing Series in Composites Science and Engineering, pages 170–210. Woodhead Publishing, 2000.

[2] Z.H. Jin C. T. Sun. *Fracture mechanics*. Waltham, 2012.

[3] S Stutz, J Cugnoni, and J Botsis. Studies of mode I delamination in monotonic and fatigue loading using {FBG} wavelength multiplexing and numerical analysis. *Composites Science and Technology*, 71(4):443–449, 2011.

[4] Te Tay. Characterization and analysis of delamination fracture in composites: An overview of developments from 1990 to 2001. *Applied Mechanics Reviews*, 56(1):1–32, 2003.

[5] P Davies, Brk Blackman, and Aj Brunner. Standard test methods for delamination resistance of composite materials: current status. *Applied Composite Materials*, 5(Iso 4585):345–364, 1998.

[6] S Sridharan. *Delamination behaviour of composites*. Cambridge, 2008.

[7] T. L. Anderson. *Fracture Mechanics*. CRC Press, Boca Raton, FL, 2005.

[8] J Paulo Davim, J Campos Rubio, and A M Abrao. A novel approach based on digital image analysis to evaluate the delamination factor after drilling composite laminates. *Composites Science and Technology*, 67(9):1939–1945, 2007.

[9] Jang-Kyo Kim and Man-Lung Sham. Impact and delamination failure of woven-fabric composites. *Composites Science and Technology*, 60(5):745–761, 2000.

[10] Shuchang Long, Xiaohu Yao, and Xiaoqing Zhang. Delamination prediction in composite laminates under low-velocity impact. *Composite Structures*, 132:290–298, 2015.

[11] Michael May. Numerical evaluation of cohesive zone models for modeling impact induced delamination in composite materials. *Composite Structures*, 133:16–21, 2015.

[12] V V Bolotin. Mechanics of delaminations in laminate composite structures, 2001.

[13] S. S. Wang. Fracture Mechanics for Delamination Problems in Composite Materials. *Journal of composite materials*, vol. 17(3):210–223, 1983.

[14] B. Pradhan D. Chakraborty. Effect of Ply Thickness and Fibre Orientation on Delamination Initiation in Broken Ply Composite Laminates. *Journal of Reinforced Plastics and Composites*, 18(8):735–758, 1999.

[15] B. Bigourdan N. Baral, P. Davies,C. Baley. Delamination behaviour of very high modulus carbon/epoxy marine composites. *Compsosites Science and Technology*, 68(3-4):995–1007, 2008.

[16] M. Kenane. Delamination Growth In Unidirectional Glass/Epoxy Composite Under Static And Fatigue Loads. *Physics Procedia*, 2(3):1195–1203, 2009.

[17] Joakim Schön. A model of fatigue delamination in composites. *Composites Science and Technology*, 60(4):553–558, 2000.

[18] J Botsis and D Zhao. Fatigue fracture process in a model composite. *Composites Part A: Applied Science and Manufacturing*, 28(7):657–666, 1997.

[19] AJ Russell and KN Street. Moisture and Temperature Effects on the Mixed-Mode Delamination Fracture of Unidirectional Graphite/Epoxy. *Delamination and Debonding of Materials, ASTM STP 876*, pages 349–370, 1985.

[20] René de Borst and Joris J C Remmers. Computational modelling of delamination. *Composites Science and Technology*, 66(6):713–722, 2006.

[21] R. Krueger. Virtual crack closure technique: History, approach, and applications. *Applied Mechanics Reviews*, 57(2):109–143, 2004.

[22] C T Sun and Z.-H. Jin. Modeling of composite fracture using cohesive zone and bridging models. *Composites Science and Technology*, 66(10):1297–1302, 2006.

[23] B. Cox Q. Yang. Cohesive models for damage evolution in laminated composites. *International Journal of Fracture*, 133(2):107–137, 2005.

[24] I. Scheider and W. Brocks. The Effect of the Traction Separation Law on the Results of Cohesive Zone Crack Propagation Analyses. *Key Engineering Materials*, 251-252:313–318, 2003.

[25] Giulio Alfano. On the influence of the shape of the interface law on the application of cohesive-zone models. *Composites Science and Technology*, 66(6):723–730, 2006.

[26] P. Camanho A. Turon and J. Costa. *Delamination in composites*. Saarbrücken, 2008.

[27] A Turon, J Costa, P P Camanho, and C G Dávila. Simulation of delamination in composites under high-cycle fatigue. *Composites Part A: Applied Science and Manufacturing*, 38(11):2270–2282, 2007.

[28] P. Davies A. Brunner, B. Blackman. A status report on delamination resistance testing of polymer-matrix composites. *Engineering Fracture Mechanics*, 75(9):2779–2794, 2008.

[29] ASTM D5528. Standard Test Method for Mode I Interlaminar Fracture Toughness of Unidirectional Fiber-Reinforced Polymer Matrix Composites. 2001.

[30] ASTM D6115 - 97. Standard Test Method for Mode I Fatigue Delamination Growth Onset of Unidirectional Fiber-Reinforced Polymer Matrix Composites. 2011.

[31] P P Camanho and G Catalanotti. On the relation between the mode I fracture toughness of a composite laminate and that of a 0Â° ply: Analytical model and experimental validation. *Engineering Fracture Mechanics*, 78(13):2535–2546, 2011.

[32] V. T. Buchwald R. M. L. Foote. An exact solution for the stress intensity factor for a double cantilever beam. *International Journal of Fracture*, 29(3):125–134, 1985.

[33] J. G. WILLIAMS S. HASHEMI, A. J. KINLOCH. Corrections needed in double-cantilever beam tests for assessing the interlaminar failure of fibre-composites. *Journal of Materials Science Letters*, 8:125–129, 1989.

[34] B R K Blackman, A J Brunner, and J G Williams. Mode {II} fracture testing of composites: a new look at an old problem. *Engineering Fracture Mechanics*, 73(16):2443–2455, 2006.

[35] J.D. Barrett and R.O. Foschi. Mode II stress-intensity factors for cracked wood beams. *Engineering Fracture Mechanics*, 9(2):371–378, 1977.

[36] R.B. Pipes L.A. Carlsson, J.W. Gillespie JR. On the Analysis and Design of the End Notched Flexure (ENF) Specimen for Mode II Testing. *Journal of Composite Materials*, 20(6):594–604, 1986.

[37] K Kageyama, Kikuchi, M, and N Yanagisawa. Stabilized End Notched Flexure Test: Characterization of Mode II Interlaminar Crack Growth. *ASTM STP1110-EB*, 3:210–225, 1991.

[38] H. Wang and T. Vu-Khanh. Use of end-loaded-split (ELS) test to study stable fracture behaviour of composites under mode II loading. *Composite Structures*, 36(1-2):71–79, 1996.

[39] Clara Schuecker and Barry D. Davidson. Evaluation of the accuracy of the four-point bend end-notched flexure test for mode II delamination toughness determination. *Composites Science and Technology*, 60(11):2137–2146, 2000.

[40] X. Sun and B. D. Davidson. A Direct Energy Balance Approach for Determining Energy Release Rates in Three and Four Point Bend End Notched Flexure Tests. *International Journal of Fracture*, 135(1):51–72, 2005.

[41] C Schuecker and BD Davidson. Effect of Friction on the Perceived Mode II Delamination Toughness from Three- and Four-Point Bend End-Notched Flexure Tests. *ASTM STP 1383*, pages 334–344, 2001.

[42] B. D. Davidson. Influences of Friction, Geometric Nonlinearities, and Fixture Compliance on Experimentally Observed Toughnesses from Three and Four-point Bend End-notched Flexure Tests. *Journal of composite materials*, 41(10):1177–1196, 2007.

[43] ASTM D6671. Standard Test Method for Mixed Mode I-Mode II Interlaminar Fracture Toughness of Unidirectional Fiber Reinforced Polymer Matrix Composites. 2006.

[44] Yeh-Hung Lai, M. Dwayne Rakestraw, and David A. Dillard. The cracked lap shear specimen revisited: a closed form solution. *International Journal of Solids and Structures*, 33(12):1725–1743, 1996.

[45] Liyong Tong and Quantian Luo. Analysis of cracked lap shear (CLS) joints. *Modeling of Adhesively Bonded Joints*, (1), 2008.

[46] TK O'Brien. Mixed-Mode Strain-Energy-Release Rate Effects on Edge Delamination of Composites. *ASTM STP 836*, pages 125–142, 1984.

[47] J.M. Greer, S.E. Galyon Dorman, and M.J. Hammond. Some comments on the Arcan mixed-mode (I/II) test specimen. *Engineering Fracture Mechanics*, 78(9):2088–2094, 2011.

[48] WL Bradley and RN Cohen. Matrix Deformation and Fracture in Graphite-Reinforced Epoxies. *ASTM STP 876*, pages 389–410, 1985.

[49] S Hashemi, AJ Kinloch, and G Williams. Mixed-Mode Fracture in Fiber-Polymer Composite Laminates. *Composite Materials: Fatigue and Fracture*, 3 ASTMSTP:143–168, 1991.

[50] J. R. Reeder and J. R. Crews Jr. Mixed-Mode Bending Method for Delamination Testing. *AIAA Journal*, 28(7):1270–1276, 1990.

[51] RH Martin and PL Hansen. Experimental Compliance Calibration for the Mixed-Mode Bending (MMB) Specimen. *Composite Materials: Fatigue and Fracture ASTM STP 1285*, 6:305–323, 1997.

[52] HT Hahn. A Mixed-Mode Fracture Criterion for Composite Materials. *Composite Technology Review*, 5(1):26–29, 1983.

[53] Johannesson T and Blikstad M. Fractography and Fracture Criteria of the Delamination Process. *ASTM STP876*, pages 411–423, 1985.

[54] M L Benzeggagh and M Kenane. Measurement of mixed-mode delamination fracture toughness of unidirectional glass/epoxy composites with mixed-mode bending apparatus. *Composites Science and Technology*, 56(4):439–449, 1996.

[55] W.S. Johnson and P.D Mangalgiri. Investigation of fiber bridging in double cantilever beam specimens. *Journal of composites technology and research*, 9(1):10–13, 1987.

[56] G. Bao Suo and Z. Remarks on Crack-Bridging Concepts. *Applied Mechanics Reviews*, 45(8):355–366, 1992.

[57] Bent F. Sørensen, E. Kristofer Gamstedt, Rasmus C. Østergaard, and Stergios Goutianos. Micromechanical model of cross-over fibre bridging - Prediction of mixed mode bridging laws. *Mechanics of Materials*, 40(4-5):220–234, 2008.

[58] Victor C. Li, Youjiang Wang, and Stanley Backer. A micromechanical model of tension-softening and bridging toughening of short random fiber reinforced brittle matrix composites. *Journal of the Mechanics and Physics of Solids*, 39(5):607–625, 1991.

[59] Mototsugu Sakai Tatsuya Miyajima. Fiber bridging of a carbon fiber-reinforced carbon matrix lamina composite. *Journal of Materials Research*, 6(3):539 – 547, 1991.

[60] S.M. Spearing and A.G. Evans. The role of fiber bridging in the delamination resistance of fiber-reinforced composites. *Acta Metallurgica et Materialia*, 40(9):2191–2199, 1992.

[61] Michel Studer, Kara Peters, and John Botsis. Method for determination of crack bridging parameters using long optical fiber Bragg grating sensors. *Composites Part B: Engineering*, 34(4):347–359, 2003.

[62] L Sorensen, J Botsis, Th. Gmür, and L Humbert. Bridging tractions in mode I delamination: Measurements and simulations. *Composites Science and Technology*, 68(12):2350–2358, 2008.

[63] S P Fernberg and L A Berglund. Bridging law and toughness characterisation of {CSM} and {SMC} composites. *Composites Science and Technology*, 61(16):2445–2454, 2001.

[64] Frederic Lachaud, Christine Espinosa, Laurent Michel, Pierre Rahme, and Robert Piquet. Modelling Strategies for Simulating Delamination and Matrix Cracking in Composite Laminates. *Applied Composite Materials*, pages 377–403, 2014.

[65] F. Bianchi and X. Zhang. A cohesive zone model for predicting delamination suppression in z-pinned laminates. *Composites Science and Technology*, 71(16):1898–1907, 2011.

[66] Denis D R Cartié, Manos Troulis, and Ivana K Partridge. Delamination of Z-pinned carbon fibre reinforced laminates. *Composites Science and Technology*, 66(6):855–861, 2006.

[67] Francesco Bianchi and Xiang Zhang. Predicting mode II delamination suppression in z-pinned laminates. *Composites Science and Technology*, 72(8):924–932, 2012.

[68] Hakan Kilic Venkata Dantuluri, Spandan Maiti, Philippe H. Geubelle, Rakesh Patel. Cohesive modeling of delamination in Z-pin reinforced composite laminates. *Composites Science and Technology*, 2006.

[69] Hao Cui, Yulong Li, Sotiris Koussios, and Adriaan Beukers. Mixed mode cohesive law for Z-pinned composite analyses. *Computational Materials Science*, 75:60–68, 2013.

[70] K O Hill, Y Fujii, D C Johnson, and B S Kawasaki. Photosensitivity in optical fiber waveguides: Application to reflection filter fabrication. *Applied Physics Letters*, 32(10), 1978.

[71] G Meltz, W W Morey, and W H Glenn. Formation of Bragg gratings in optical fibers by a transverse holographic method. *Opt. Lett.*, 14(15):823–825, 1989.

[72] V Antonucci, M Giordano, A Cusano, J Nasser, and L Nicolais. Real time monitoring of cure and gelification of a thermoset matrix. *Composites Science and Technology*, 66(16):3273–3280, 2006.

[73] Marco Lai. *Hygrothermal Ageing and Damage Characterization in Epoxies and in Epoxy-Glass Interfaces*. PhD thesis, EPFL, 2011.

[74] D Coric Marco Lai, J Botsis, Joel Cugnoni. An experimental-numerical study of moisture absorption in an epoxy. *Composites Part A: Applied Science and Manufacturing*, 43(7):1053–1060, 2012.

[75] Jeannot Frieden, Joël Cugnoni, John Botsis, Thomas Gmür, and Dragan Ćorić. High-speed internal strain measurements in composite structures under dynamic load using embedded {FBG} sensors. *Composite Structures*, 92(8):1905–1912, 2010.

[76] Shizeng Lu, Mingshun Jiang, Qingmei Sui, Yaozhang Sai, and Lei Jia. Damage identification system of CFRP using fiber Bragg grating sensors. *Composite Structures*, 125:400–406, 2015.

[77] R. Di Sante and L. Donati. Strain monitoring with embedded Fiber Bragg Gratings in advanced composite structures for nautical applications. *Measurement*, 46(7):2118–2126, 2013.

[78] Mingjun Xia, Mingshun Jiang, Qingmei Sui, and Lei Jia. Theoretical and experimental analysis of interaction from acoustic emission on fiber Bragg grating. *Optik - International Journal for Light and Electron Optics*, 126(11-12):1150–1155, 2015.

[79] Jose Manuel Menendez Martin and Alfredo Guemes Gordo. SHM Using Fiber Sensors in Aerospace Applications. In *Optical Fiber Sensors*, page MF1. Optical Society of America, 2006.

[80] A. Panopoulou, T. Loutas, D. Roulias, S. Fransen, and V. Kostopoulos. Dynamic fiber Bragg gratings based health monitoring system of composite aerospace structures. *Acta Astronautica*, 69(7-8):445–457, 2011.

[81] I Mckenzie and N Karafolas. Fiber optic sensing in space structures: the experience of the European Space Agency. In M Voet, R Willsch, W Ecke, J Jones, and B Culshaw, editors, *17th International Conference on Optical Fibre Sensors*, volume 5855 of *Society of Photo-Optical Instrumentation Engineers (SPIE) Conference Series*, pages 262–269, 2005.

[82] John Botsis. Fiber Bragg Grating Applied to In Situ Characterization of Composites. pages 1–15, 2012.

[83] K. P. Koo A. D. Kersey, M. A. Davis, H. J. Patrick, M. LeBlanc, M. A. Putnam C. G. Askins, and E. Joseph Friebele. Fiber Grating Sensors. *Journal of lightwave technology*, 15(8):1442–1463, 1997.

[84] K. S. C Kuang and W. J. Cantwell. Use of conventional optical fibers and fiber Bragg gratings for damage detection in advanced composite structures: A review. *Applied Mechanics Reviews*, 56(5):493–513, 2003.

[85] H. Wang, S.L. Ogin, A.M. Thorne, and G.T. Reed. Interaction between optical fibre sensors and matrix cracks in cross-ply GFRP laminates. Part 2: Crack detection. *Composites Science and Technology*, 66(13):2367–2378, 2006.

[86] E.N Barton, S.L Ogin, A.M Thorne, G.T Reed, and B.H Le Page. Interaction between optical fibre sensors and matrix cracks in cross-ply GRP laminates-part 1: passive optical fibres. *Composites Science and Technology*, 61(13):1863–1869, 2001.

[87] José M A Silva, Tessaleno C Devezas, AbíLio P Silva, and José A M Ferreira. Mechanical Characterization of Composites with Embedded Optical Fibers. *Journal of Composite Materials*, 39(14):1261–1281, 2005.

[88] S. Stutz, J. Cugnoni, and J. Botsis. Crack - fiber sensor interaction and characterization of the bridging tractions in mode I delamination. *Engineering Fracture Mechanics*, 78(6):890–900, 2011.

[89] R. M. Measures. *Structural Monitoring With Fiber Optic Technology*. 1999.

[90] G. Meltz W. Morey, J. R. Dunphy. Multiplexing fiber Bragg grating sensors. *Fiber and Integrated Optics*, 10(4):351–360, 1991.

[91] A. A. Griffith. The phenomena of rupture and flow in solids. *Philosophical Transactions*, 221:163–198, 1920.

[92] G. R. Irwin. A critical energy rate analysis of fracture strength. *Welding Journal*, 33:193, 1954.

[93] R. Bertholds, A. Dandliker. Determination of the individual strain-optic coefficients in single-mode optical fibres. *Journal of Lightwave Technology*, 6(1):17–20, 1988.

[94] N. Shibata, S. Shibata, and T. Edahiro. Refractive index dispersion of lightguide glasses at high temperature. *Electronics Letters*, 17(8):310–311, 1981.

[95] Hans G Limberger Philippe Giaccari, Gabriel R Dunkel, Laurent Humbert, John Botsis and René P Salathé. On a direct determination of non-uniform internal strain fields using fibre Bragg gratings. *Smart Materials and Structures*, 14(1):127–136, 2004.

[96] P. Giaccari. *Fiber bragg grating characterization by optical low coherence reflectometry and sensing applications*. Phd thesis, EPFL, 2003.

[97] D7905/D7905M-14. Standard Test Method for Determination of the Mode II Interlaminar Fracture Toughness of Unidirectional Fiber-Reinforced Polymer Matrix Composites. 2014.

[98] Carlos G. Davila Camanho P. Mixed-Mode Decohesion Finite Elements for the Simulation of Delamination in Composite Materials. *NASA/TM-2002-211737*, 2002.

[99] G. Pappas and J. Botsis. Intralaminar fracture of unidirectional carbon/epoxy composite: experimental results and numerical analysis. *International Journal of Solids and Structures*, 85:114–124, 2016.

Curriculum Vitæ

Marco Borotto

Date of birth: 15 January 1984
Place of birth: Milan, Italy
e-mail: marcoborotto@hotmail.com

Education

01/2012 – 05/2016 ***PhD student, Solid Mechanics***
École Polytechnique Fédérale de Lausanne (EPFL), Switzerland VD
Phd Thesis: "Bridging effects on Mixed Mode delamination: experiments and numerical simulation**"**

2011 ***Qualifying examination to engineers register in Italy***

2007 – 2010 ***Master's degree in Mechanical Engineering***
Vehicle design - Politecnico of Milan, Italy
MSc Thesis: "Design and construction of a dynamometer structure made of composite material based on fiber optic sensors"

2003 - 2007 ***Bachelor's Degree in Mechanical Engineering***
Vehicle design - Politecnico of Milan

2003 ***High School Diploma***
Salesiani S. Ambrogio, Milan

Teaching Experiences

01/2012 – 2015 Assistant for the course "Mechanics of Structures"
Prof. J. Botsis, LMAF, EPFL

01/2013 – 2015 Assistant for the course "Continuum Mechanics"
Prof. J. Botsis, LMAF, EPFL

01/2013 – 2015 Assistant for the course "Fracture Mechanics"
Prof. J. Botsis, LMAF, EPFL

Working Experiences

01/2011 – 01/2012 *Research fellowship at Politecnico of Milan, Italy*
Research on Smart Structures, Energy Harvesting and measurement systems based on embedded optical fibers in composite materials

2007 *JAS, HONDA Motorsport*
Research and development of several mechanical components for racing vehicles. Vehicle dynamic and structural optimization of several components

Presentations

25th – 27th September 2013	M.Borotto, J.Botsis Bridging effects on carbon/epoxy composite materials *IV ECCOMAS Thematic Conference on the Mechanical Response of Composites* S. Miguel, Azores
7th – 11th July 2014	M.Borotto, J.Botsis The effects of bridging on Mixed-Mode delamination in carbon/epoxy composite *16th International Conference on Experimental Mechanics* Cambridge, UK

Publications

2016	M.Borotto, J. Botsis, J. Cugnoni *The effects of bridging on Mixed-mode delamination of unidirectional carbon epoxy: Part II Numerical Modelling* In preparation
2016	M.Borotto, J. Botsis, J. Cugnoni *The effects of bridging on Mixed-mode delamination of unidirectional carbon epoxy: Part I Experiments* In preparation
2012	M.Borotto, E.de Cais, M.Belloli, A.Bernasconi, S.Manzoni *Metrological performances of fiber Bragg grating sensors and comparison with electrical strain gauges* Key Engineering Materials, Vol. 495, pp. 53-57, 2012
2012	E. de Cais, M.Borotto, M.Belloli, A.Bernasconi, S.Manzoni *Metrological performances of smart structures based on Bragg grating sensors* Key Engineering Materials, Vol. 495, pp. 41-44, 2012

Competences

Software	Matlab, Catia V5, Abaqus, Solid Works, Adams, MS Office

Patents and start up

2013	*Management, Business and Marketing Course* *Venture Lab*, École Polytechnique Fédérale de Lausanne (EPFL), CH
2016	Worldwide patent: *Capacitive sensor array for dental occlusion monitoring* WO2015181693